FOURIER-BASED DESIGN OF ACOUSTIC TRANSDUCERS

A Thesis
Presented to
The Academic Faculty

by

Matteo Carrara

In Partial Fulfillment
of the Requirements for the Degree
Doctor of Philosophy in the
School of Aerospace Engineering

Georgia Institute of Technology
Spring 2016

FOURIER-BASED DESIGN OF ACOUSTIC TRANSDUCERS

Approved by:

Dr. Massimo Ruzzene, Advisor
School of Aerospace Engineering
Georgia Institute of Technology

Dr. Julian J. Rimoli
School of Aerospace Engineering
Georgia Institute of Technology

Dr. Alper Erturk
School of Mechanical Engineering
Georgia Institute of Technology

Dr. Karim Sabra
School of Mechanical Engineering
Georgia Institute of Technology

Dr. Min-Feng Yu
School of Aerospace Engineering
Georgia Institute of Technology

Date Approved: December 11, 2015

To my beautiful wife Francesca, and my daughter Sofia.

You are the stars of my life.

ACKNOWLEDGEMENTS

I would like to express my sincere appreciation to my advisor Dr. Massimo Ruzzene, you have been a tremendous mentor for me during this years. I want to thank you for encouraging my research and for allowing me to grow both on personal and professional levels. Your advices on research, career, and life have been priceless.

I would also like to thank Dr. Julian Rimoli, Dr. Min-Feng Yu, Dr. Alper Erturk, and Dr. Karim Sabra, for serving as my committee members. Thank you for all your brilliant comments, useful insights, and, more importantly, for the research ideas you inspired in me and helped me pursue.

A special thanks goes to my labmates and friends during my first period at Georgia Tech: Filippo, Maria, Matteo, Emanuele, and Paolo. I do not know what I would have done without your professional and personal help that eased my transition to the United States and, in particular, to Atlanta.

I would like to thank my fellow labmates and all the friends I have made during this years for the stimulating discussions, the work we did together, the encouragement and support, the lunches and coffee breaks, the allupos, the passeggiatine, the Xbox nights (and days), the dinners at El Potro, the wings and the tacos, the biking to Alabama, the tennis and ping-pong matches, the brown bags, and, in general, for all the fun we had in the last four years. It was an amazing ride and I am glad that you were part of it. You all have showed me immense affection that I will bring with me forever.

A special thanks goes to my family. Words cannot express how grateful I am to my beloved wife Francesca, for all the sacrifices that you have made on my behalf. Four years ago we blindly decided together to undertake this journey so far from our homes, and I cannot be more happy that we did. It has been tough at times, but the joy that baby Sofia brought to our lives easily outshines all the down periods that inevitably mark the path towards a doctorate. You are my everything.

Last, but light years away from least, I want to express my gratitude to my whole extended family. This entire experience would not have been possible without the unconditional support of my parents Doriana and Maurizio, my sister Cristina, my grandma Angela (and grandpa Attilio, even if you are not with us anymore I think of you every single day), and my parents-in-law Lucia and Aurelio. Thanks for understanding that the path that Francesca and I decided to pursue, even if thousands of miles away from home, was the right one for us. I love you with all my heart.

TABLE OF CONTENTS

LIST OF TABLES

LIST OF FIGURES

SUMMARY

The work presented in this thesis investigates novel transducer implementations that take advantage of directional sensing and generation of acoustic waves. These transducers are conceived by exploiting a Fourier-based design methodology. The proposed devices find application in the broad field of Structural Health Monitoring (SHM), which is a very active research area devoted to the assessment of the structural integrity of critical components in aerospace, civil and mechanical systems. Among SHM schemes, Guided Waves (GWs) testing has emerged as a prominent option for inspection of plate-like structures using permanently attached piezoelectric transducers.

GWs-based methods rely on the generation and sensing of elastic waves to evaluate structural integrity. They offer an effective method to estimate location, severity and type of damage. It is widely acknowledged among the GWs-SHM community that effective monitoring of structural health is facilitated by sensors and actuators designed with ad hoc engineered capabilities. The objective of this research is to design innovative piezoelectric transducers by specifying their electrode patterns in the Fourier domain. Taking advantage of the Fourier framework, transducer design procedures are outlined and tailored to relevant SHM applications, such as (i) directional actuation and sensing of GWs, (ii) simultaneous sensing of multiple strain components with a single device, and (iii) estimation of the location of impact sites on structural components. The proposed devices enable significant reductions in cost, hardware, and power requirements for advanced SHM schemes when compared to current technologies.

This work specifically contributes to the formulation of Frequency Steered Acoustic Transducers (FSATs), a class of devices characterized by a spatial arrangement of active material which produces directional transduction characteristics that are frequency dependent. Based on prior preliminary theoretical formulations for the FSAT, this thesis advances

the state of the art by (i) prototyping the transducer to operate in actuation mode for monolithic piezoelectric wafers for applications on both isotropic and anisotropic plates, and (ii) adapting the design to employ piezo-fibrous active layers that are able to conform to non-flat surfaces. These milestones are achieved by exploring and implementing fabrication techniques for rapid and cost-effective patterning of geometrically complex electrodes onto both (i) monolithic piezoelectric wafers, and (ii) piezo-fibrous active layers. The latter also requires theoretical procedures for anisotropy compensation to guarantee consistent actuation authority throughout the device bandwidth. Finite elements simulations as well as experimental validations are presented to demonstrate the capabilities of such devices.

The Fourier-based design procedure is then extended and applied to two different applications relevant to SHM, namely strain and impact directionality sensing. For strain sensing purposes, the Acoustic Wave Rosette (AWR) concept is presented. This device is characterized by a pattern whose bi-dimensional Fourier representation features maxima at specific directions. The resulting sensor leads to a multi-band spatial filter suitable for strain sensing applications by monitoring peaks shift in the wavenumber domain triggered by the deformation state in the underlying structure. The AWR is a one-of-a-kind device able to gather information on multiple strain components. Finally, for impact localization purposes, the Impact Directionality Revealer (IDR) is presented. In this concept, patterning of the electrode along with wave amplitude data are exploited to retrieve informations regarding the location of impact events. The theoretical framework along with numerical/analytical demonstrations for the two concepts are unique contributions of this thesis.

CHAPTER I

INTRODUCTION

1.1 Overview

The work presented in this thesis investigates novel acoustic transducer concepts that take advantage of electrode patterning designed in the Fourier domain. The proposed devices find application in the broad area of Structural Health Monitoring (SHM). This chapter provides a brief background on SHM, with particular emphasis on (i) Guided Waves (GWs) SHM, and (ii) on the employment of piezoelectric transducers, highlighting existing techniques and practices for GWs inspections. Successively, motivations for the present work are detailed along with research objectives and contributions to the state of the art on acoustic transducers. Finally, the chapter concludes with the organization of the dissertation.

1.2 Background

In recent years, there has been an increasing awareness of the importance of damage prognosis systems in civil, mechanical and aerospace structures. It is foreseen that, in a not-so-distant future, such systems will have the potential to inform the user about the structure's state of health, potentially providing warnings about damage initiation, along with an estimate of the remaining useful life of the structural component. Potential benefits of such a technology are enormous. By taking advantage of these systems, maintenance procedures for structures could change from being schedule-driven to condition-based. This would allow to reduce off-line periods, thereby guaranteeing cost savings and labor reduction requirements for structural inspections. Most significantly, confidence levels in operating structures would increase dramatically as a result of the new safeguards against unpredictable structural degradation mechanisms, particularly for aging structures. In addition, the safety of the end-users, which is of paramount importance in any engineering field, and particularly for the aerospace industry, would be better ensured.

1.2.1 Structural Health Monitoring

SHM is a key component of damage prognosis systems. In a broader sense, SHM refers to the process of implementing a damage detection and characterization strategy for engineering structures. More practically, SHM is the component that examines the structure for deterioration and provides information about any potential damage that is detected. SHM is thus used for rapid condition screening and aims to provide reliable information regarding the integrity of a structure.

SHM strategies can be broadly classified as active or passive, depending on whether they involve the use of actuators. Examples of passive schemes are acoustic emission and strain/loads monitoring [73, 53, 76, 46, 65, 13, 34, 23]. Typically, these implementations require high sensor densities on the structure, which is particularly critical for aerospace components. Conversely, in active schemes, the structure is excited in a repeatable manner using actuators so that it can be examined for damage in real-time, where and when required. In the past two decades, GWs testing has emerged as a very prominent option among active schemes. It can offer an effective method to estimate location, severity and type of damage, and it is an established practice in the Non-Destructive Evaluation and Testing (NDE/NDT) industry. More recently, GWs have also demonstrated suitability for SHM applications having an on-board, preferably built-in, sensor and actuator network to assess the state of a structure during operation. The main asset to GWs SHM schemes is that the actuator-sensor pair has a large coverage area, thus resulting in fewer units distributed over the structure.

1.2.2 Guided Waves

GWs are stress waves forced to follow a path defined by structural boundaries. For example, when a beam is excited at high frequency, stress waves travel along the beam axis away from the excitation source, i.e. the beam guides the waves along its axis, thus the name: guided waves. Similarly, in two dimensions, the free surfaces of a plate guide waves within its confines as sketched in Figure 1, where the case of a flexural GW mode propagating in an aluminum plate is represented. There are several application areas for guided elastic waves

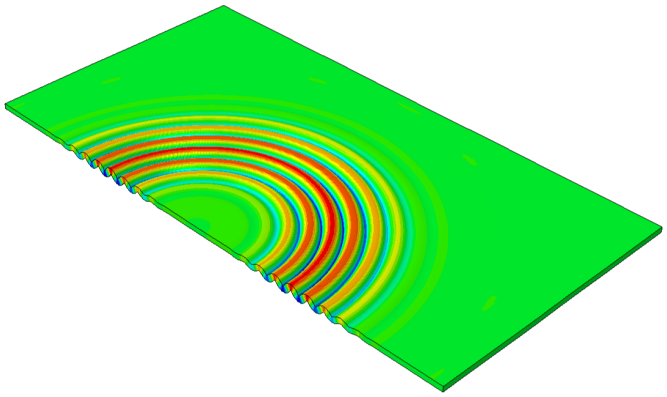

Figure 1: Example of a guided wave traveling in an aluminum plate-like structure.

in solids, such as seismology, inspection, material characterization, delay lines, etc.[1, 3, 30]. Lamb waves are a very important class among GWs [26, 29, 64]. Their propagation domain is that of solid plates (or shells) with free surfaces. Due to the abundance of plate- and shell-like structural configurations they have been the subject of much scrutiny. Lamb waves are dispersive, which means that the propagation velocities are dependent on frequency, and propagate according to several modes which are either symmetric or anti-symmetric with respect to the plate mid thickness, Figure 2. The potential damage types that a Lamb wave-based inspection system can provide are well summarized in [67], for example. A comprehensive review of GWs SHM approaches is also presented in [64].

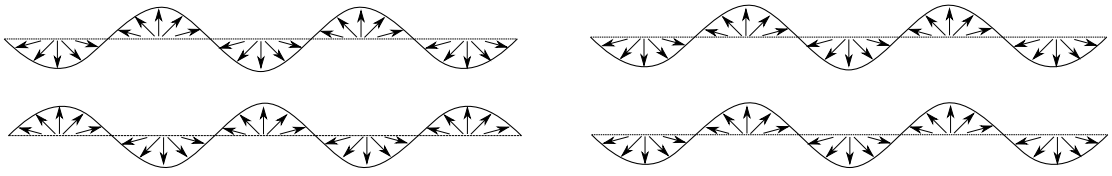

(a) S_0 Lamb mode (b) A_0 Lamb mode

Figure 2: Qualitative schematic of displacement fields associated to the first symmetric (S_0) and first antisymmetric (A_0) Lamb wave modes.

Other classes of GWs have also been examined in the literature. Among them, an important category is that of Rayleigh waves, also known as Surface Acoustic Waves (SAWs), which propagate close to the free surface of elastic solids. These waves represent elastic

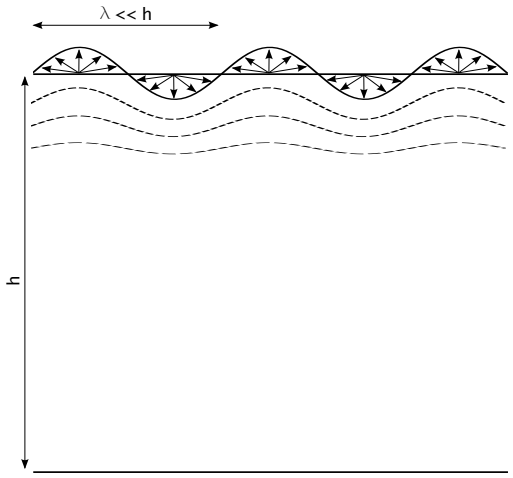

Figure 3: Qualitative schematic of displacement field associated to Rayleigh waves.

perturbations propagating near the free boundary of a solid and rapidly decaying with depth, Figure 3. SAW-based devices have been in commercial use for over 60 years, and have proven to be the most sensitive sensors among acoustic devices, as a result of their concentration of energy density on the surface [21]. In addition, due to their sensitivity to perturbations to many different physical parameters, they have been used for a wide variety of purposes over the years. As an example, changing the state of stress of the hosting medium, SAW devices have been used as temperature, pressure, torque, shock, and force transducers [87, 15, 61, 52].

Given their intrinsic low-power requirements, and potentially wireless operations [79], SAW technology is beginning to attract serious interest for a broad range of other sensors, especially in aerospace and SHM applications [9, 97]. In these areas, many applications have very challenging requirements: (i) maintenance-free, no-battery operations, (ii) no power deriving from scavenging or external power source, (iii) reliable life-cycle that guarantee years in a wing structure or hours in an engine exhaust, and (iv) miniaturization, just to cite a few. For SAW operations, potential SHM applications are presented by Wilson in [98].

Details on the fundamentals of GWs propagation can be found in texts such as Auld [3], Graff [30], and Achenbach [1].

1.2.3 Transducers for GWs SHM

Critical elements of GWs SHM are the transducers, their network arrangement, and the overall SHM architecture. For the case of Non-Destructive Evaluation (NDE), the most common transducers are angled piezoelectric wedges [103, 91], comb transducers [59] and electromagnetic acoustic transducers (EMATs) [2]. Other, more recent, options are Hertzian contact transducers [17] and lasers [60]. While these types of devices are suited for maintenance checks when the structure is off-line, they are not compact enough to be permanently attached to the structure during its operation. This is particularly true for the case of the aerospace industry, where mass and space penalties associated with additional transducers should be maintained to a minimum.

The most commonly used transducers in GWs SHM are embedded or surface-bonded piezoelectric wafers (hereafter referred to as piezos). These devices are inexpensive and available in very fine thicknesses, ranging from $100\,\mu$m for ceramics, down to $9\,\mu$m for polymer films, making them suitable for permanent integration into structural components. Piezos exploit the direct and inverse piezoelectric effect that couples the electrical and mechanical behavior of the material. An electric charge is collected on the surface of the piezoelectric material when it is strained. Conversely, mechanical strain is generated in response to an applied electric field. Hence, they can be consistently used both as actuators and sensors [27]. The most commonly available piezoelectric materials are (i) lead zirconium titanate ceramic, commonly referred to as PZT, [20, 42], and (ii) polyvinylidene fluoride (PVDF), which is a polymer film. Both of these materials usually feature a through-the-thickness polarization, which is also the direction in which the voltage is either applied or sensed. When used in actuation-mode, the voltage signal applied to the electrodes causes waves to be excited in the structure. Conversely, when used in sensing-mode, the strain over the sensor area causes a voltage signal to be generated across the piezo. PZTs are quite brittle and need to be handled with care, while polymer films are very flexible and easy to handle, and can conform easily. However, because of their weaker inverse piezoelectric properties and high compliance, polymer-based transducers (e.g. PVDF) feature poorer performance both as actuators and sensors, if compared to PZTs. In addition, PVDF films

cannot be embedded into composite structures because of the loss of piezoelectric properties under typical curing conditions. For these reasons, PZTs are the most popular choice for the transducer material in most GWs SHM research groups [41, 40, 58].

1.2.4 Transducers Directionality and Electrode Patterning

It is widely acknowledged that GWs SHM approaches potentially benefit from the use of transducers with controllable directional characteristics, so that selective scanning of a surface can be performed to locate damage, impacts or cracks.

Wave steering through phased arrays [85, 51, 44] is a well-established technique, widely used in radar, sonar, seismology, oceanology, and medical imaging such as echocardiography and ultrasonography [88]. A phased array consists of a group of sensors located at distinct spatial locations. The relative phase of each transducer is varied in a way that the effective propagation pattern of the resulting signal is directed in a desired direction and inhibited in undesired ones. This principle has made possible the development of radar and sonar systems that allow to scan the horizon in an electronic way, without relying on any mechanical movement. Phased array concepts are also extensively adopted in ultrasonic imaging for NDE applications [8, 56] because of their intrinsic advantages such as (i) high inspection speed, (ii) flexible data processing capabilities, (iii) high resolution, and (iv) scanning capability without requiring mechanical movement. Rose [68] describes a high-frequency GW phased array focusing method for performing nondestructive pipe inspection with conventional phased-array transducers. Froome [24] designed and built a permanently attached GW array prototype to be used in long term monitoring of structural integrity. Major limitations in the path of transitioning Lamb-wave based NDE into SHM methodologies are represented by size, cost, and power requirements of conventional NDE phased arrays, which are rather bulky, expensive, and require a lot of power to operate given their intrinsic multi-channel nature.

Patterning of the sensing material (or electrode) layout yields significant opportunities to provide transducers with useful functionalities, such as inherent frequency and directional

sensitivity. This basic idea has been widely exploited for the design of interdigitated transducers (IDTs) used as part of SAW devices [36]. Linear IDT configurations are commonly employed for selective generation and detection of SAWs, Figure 4.

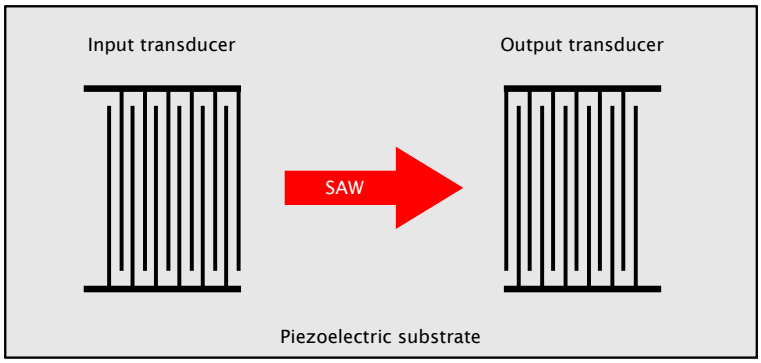

Figure 4: Qualitative schematic of an IDT device.

Other alternative configurations, such as the slanted IDT described in [101], and the annular IDTs illustrated in [50], have been proposed to achieve novel functionalities such as wide-band operations and acoustic wave focusing. As an example, an ultrasonic radiator with frequency beam steering capabilities is presented in [48]. The radiator consists of a cantilever plate placed in water, on which a pair of piezoelectric ceramics are mounted. Direction of propagation of ultrasound in water is solely steered by frequency of the applied signal. In another study a Meander antenna, whose main lobe is steerable by variation of the feed frequency, is studied [14, 77] for radar applications.

1.3 Motivations and Objectives

GW-based SHM techniques using structurally integrated transducers are still in their formative years. All the promising results mentioned previously not only demonstrate the potential benefits of such systems, but also underline some important drawbacks. On one hand, limitations are present in the array basic principle of operation, which requires wiring and multiplexing of individual array elements. The corresponding hardware complexity makes their implementation as embedded devices problematic [56, 102]. On the other hand, SAW devices, although mature from a commercial standpoint, are limited to perform

sensing of scalar fields. Multiple devices are to be employed, and carefully arranged, to perform sensing of inherently vectorial or tensorial fields, such as strain.

The present work stems from, and expands on, the work done by Senesi and Baravelli in [74, 75, 4] towards the framework formulation and design of a wavenumber spiral Frequency Steerable Acoustic Transducer (spiral FSAT). The spiral FSAT is a device that can direct energy associated with a specific Lamb wave mode in specified directions without the need for individual element control. It is characterized by a spatial arrangement of the piezoelectric material which leads to frequency-dependent directionality without relying on phasing and control of a large number of channels. This reduces the hardware requirements to a minimum. The spiral FSAT transducer prototype was previously manufactured on a PVDF substrate and applied on an aluminum plate hosting structure. Very good directional sensing capabilities were demonstrated with limited actuation capabilities due to low actuation authority of PVDF. In addition, although the device was originally presented as an effective resource for impact damage localization, its applicability is limited by the frequency content of actual impact events, which are usually not as high as the frequency typically considered for the spiral FSAT prototype [66].

The motivations of this research reside in expanding the spiral FSAT device application field to enable GW actuation and damage detection operations on aluminum and composite hosting media, and extending the directionality design framework to exploit transducer patterning for multi-component strain sensing and impact directionality detection.

Given the motivations above, the objectives of the thesis are:

- To formulate strategies for the design of novel classes of sensors and actuators that can be of practical use in SHM applications, with an extended application field that would include composite materials;

- To implement FSAT concepts in actuation mode featuring different active layers, namely (i) monolithic piezoelectric wafers, and (ii) piezo-fibrous composite layers;

- The implement working imaging techniques to enrich damage-detection capabilities of the spiral FSAT concepts on both aluminum and composite hosting media;

- To investigate a novel transducer concept, termed as Acoustic Wave Rosette (AWR), for multi-component strain sensing;
- To study a novel transducer concept, named Impact Directionality Revealer (IDR), for real-time impact detection and localization.

To accomplish the above-mentioned objectives, the work employs numerical as well as experimental methods to confirm the effort spent towards the theoretical development of FSATs, AWRs, and IDRs devices.

1.4 Contributions

Achievement of the objectives outlined in Section 1.3 would lead to the following contributions:

- The expansion of the spiral FSAT concept as a minimal complexity, reliable, and directional wave generation device;
- The experimental validation of new spiral FSAT concepts to enable actuation mode on both aluminum and composite hosting media;
- The implementation of working imaging techniques to enrich damage-detection capabilities of the spiral FSAT concepts on both aluminum and composite hosting media;
- The formulation and demonstration of the Acoustic Wave Rosette (AWR) concept, which extends the FSAT design framework to enable multi-component strain sensing by monitoring the transducer patterning deformation;
- The formulation of the Impact Directionality Revealer (IDR) concept, which extends the FSAT design framework to enable impact directionality detection for "low-frequency" scenarios.

1.5 Organization of the Thesis

The thesis is organized in seven chapters including this introduction. Chapter 2 presents the theoretical developments in support of the wavenumber design procedures of arbitrarily

shaped piezoelectric transducers. Chapter 3 presents the details of FSAT design patterns, focusing on the study of actuation capabilities of the device in presence of (i) monolithic piezo wafer substrates on isotropic and anisotropic plates, and (ii) a piezo-fibrous substrate to confer flexibility to the device. Analytical/numerical investigations are employed along with experimental testing to validate and assess the actuation performance of such devices. Chapter 4 illustrates damage detection capabilities for the monolithic devices presented in the previous chapter. To this aim, ad hoc imagining techniques that rely on signals collected by the devices through pulse-echo operations are discussed and implemented. Chapter 5 is devoted to the development of the AWR for strain sensing purposes. Analytical/numerical analyses of the device are presented, along with an experimental validation of the filtering properties associated with its electrode's patterning. Chapter 6 presents the theoretical development of the IDR. Numerical and experimental validations are presented to illustrate the IDR capabilities in terms of impact directionality estimation. Finally, Chapter 7 outlines conclusions drawn from the work and provides recommendations for future investigations.

CHAPTER II

WAVENUMBER DESIGN OF DIRECTIONAL TRANSDUCERS

2.1 Overview

This chapter presents the equations governing transducer directionality related to (i) the geometrical configuration of its electrodes, and (ii) the material that constitutes its transduction, or active, layer. The case of a piezoelectric patch of arbitrary shape is considered as a general framework to illustrate the principles of directional sensing through proper electrode shaping. The geometry-related directivities of (i) a circular patch, and (ii) a rectangular patch are then illustrated as two examples demonstrating the basic principles of the design procedure. For the latter, experimental evidence of directionality is also presented.

2.2 Sensing Principles for an Arbitrarily Shaped Piezoelectric Patch

This section presents the equations that govern sensing of Lamb waves through piezoelectric-based surface mounted devices. Starting from the constitutive relations associated to piezo materials, a general expression for the voltage sensed by an arbitrarily shaped patch when in presence of a propagating plane wave is derived.

2.2.1 Piezoelectric Constitutive Relations

The system under investigation features two domains: a thin plate-like structural component (denoted as Ω), and an arbitrarily shaped piezoelectric patch (denoted as Ω_P) of thickness t_P bonded on its top surface, as depicted in Figure 5. The piezoelectric constitutive relations expressed in the classical stress-charge form are the following [99]

$$\begin{aligned} \boldsymbol{\sigma} &= \boldsymbol{C}^E \boldsymbol{\varepsilon} - \boldsymbol{e}^T \boldsymbol{E} \\ \boldsymbol{D} &= \boldsymbol{e}\boldsymbol{\varepsilon} + \boldsymbol{\epsilon}^{\varepsilon} \boldsymbol{E} \end{aligned} \tag{1}$$

where $\boldsymbol{\sigma}$ and $\boldsymbol{\varepsilon}$ are the mechanical stress and strain vectors, $\boldsymbol{D}$ is the electric charge vector, and $\boldsymbol{E}$ the electric field vector. Also, $\boldsymbol{C}^E$ is the material stiffness matrix at constant electric

field, $\boldsymbol{e}$ is the piezoelectric coupling matrix at constant stress, and $\boldsymbol{\epsilon}^{\varepsilon}$ denotes the permittivity matrix at constant strain.

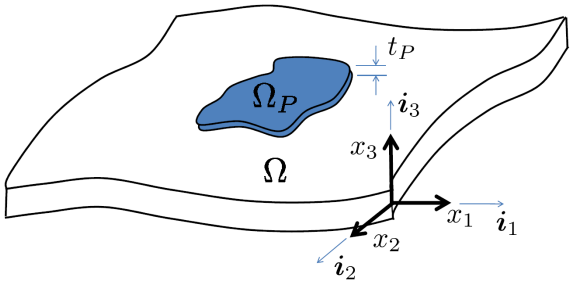

Figure 5: Plate slice with arbitrarily shaped piezoelectric patch bonded on its top surface.

It is assumed that the piezoelectric patch does not interfere with the dynamics of the plate, which means that the wavefield to be measured is not significantly altered by the presence of the transducer.

The validity of the piezoelectric constitutive relations of Equation (1) can be extended from the piezoelectric domain Ω_P to the entire domain Ω introducing the functional $\phi(\boldsymbol{x})$

$$\phi(\boldsymbol{x}) = \begin{cases} 1, & \boldsymbol{x} \in \Omega_P \\ 0, & \boldsymbol{x} \in \Omega - \Omega_P \end{cases} \tag{2}$$

which describes the shape of the electrodes of the patch, with $\boldsymbol{x} = x_1\boldsymbol{i_1} + x_2\boldsymbol{i_2}$ denoting a position vector on the plane of the structure.

A second functional $\psi(\boldsymbol{x})$ is introduced to allow for different polarizations within the piezoelectric domain. Without loss of generality, this second functional is assumed to be $\psi(\boldsymbol{x}) = \pm 1,\ \boldsymbol{x} \in \Omega_P$. In light of these considerations, Equation (1) can be rewritten as follows

$$\begin{Bmatrix} \boldsymbol{\sigma} \\ \boldsymbol{D} \end{Bmatrix} = \phi(\boldsymbol{x}) \begin{bmatrix} \boldsymbol{C}^E & -\psi(\boldsymbol{x})\boldsymbol{e}^T \\ \psi(\boldsymbol{x})\boldsymbol{e} & \boldsymbol{\epsilon}^{\varepsilon} \end{bmatrix} \begin{Bmatrix} \boldsymbol{\varepsilon} \\ \boldsymbol{E} \end{Bmatrix}, \quad \boldsymbol{x} \in \Omega. \tag{3}$$

For sensing purposes, the second row of Equation (3) is considered because it relates the electric charge developed by the patch to the strain to which it is exposed and the electric field resulting from its polarization. To further simplify the development of the equations, the following two assumptions are introduced:

- The patch is considered to be polarized across its thickness (i.e. $D_1 = D_2 = 0$);

- The patch undergoes plane stress (i.e. $\sigma_{33} = \sigma_{13} = \sigma_{23} \approx 0$).

Considering the stress-charge form of the piezoelectric constitutive equations outlined above, the second row of Equation (3) reduces to

$$D_3 = \phi(\boldsymbol{x})\boldsymbol{b}^T[\psi(\boldsymbol{x})\boldsymbol{d}^\sigma \boldsymbol{C}^E \boldsymbol{\varepsilon} + (\boldsymbol{\epsilon}^\sigma - \boldsymbol{d}^\sigma \boldsymbol{C}^E \boldsymbol{d}^{\sigma^T})\boldsymbol{E}], \quad \boldsymbol{x} \in \Omega \tag{4}$$

where $\boldsymbol{b} = [0,\ 0,\ 1]^T$, and $\boldsymbol{d}^\sigma$, $\boldsymbol{\epsilon}^\sigma$ denote the matrices of piezoelectric strain and permittivity constants evaluated at constant stress, respectively.

2.2.2 Voltage Generated by the Patch

Considering the electrical boundary conditions of the transducer in sensing mode as an open circuit, the total charge developed over the electrodes area of the piezoelectric patch can be approximatively considered null [54]

$$\int_{\Omega_p} D_3 d\boldsymbol{x} = \int_{\Omega} \phi(\boldsymbol{x}) D_3 d\boldsymbol{x} \approx 0 \tag{5}$$

Given this assumption, integration of Equation (4) yields

$$\boldsymbol{b}^T \boldsymbol{d}^\sigma \boldsymbol{C}^E \int_{\Omega} \epsilon\phi(\boldsymbol{x})\psi(\boldsymbol{x}) d\boldsymbol{x} = \boldsymbol{b}^T(\boldsymbol{d}^\sigma \boldsymbol{C}^E \boldsymbol{d}^{\sigma^T} - \boldsymbol{\varepsilon}^\sigma) \int_{\Omega} \phi(\boldsymbol{x}) \boldsymbol{E} d\boldsymbol{x} \tag{6}$$

where all the properties of the patch are assumed to be constant over Ω_P. As shown in [74], the voltage sensed by the piezoelectric patch can be expressed by integrating Equation (4) and imposing $E_1 = E_2 = 0$, with $E_3 = \frac{V}{t_P}\boldsymbol{b}$, i.e. enforcing a linear variation of the voltage across the thickness of the piezo (t_P). This procedure results in the following expression for the voltage measured across the electrodes

$$V = \frac{t_P}{A_P \left[\boldsymbol{b}^T(\boldsymbol{d}^\sigma \boldsymbol{C}^E \boldsymbol{d}^{\sigma^T} - \boldsymbol{\varepsilon}^\sigma)\boldsymbol{b}\right]} \boldsymbol{b}^T \boldsymbol{d}^\sigma \boldsymbol{C}^E \int_{\Omega} \boldsymbol{\varepsilon} f(\boldsymbol{x}) d\boldsymbol{x} \tag{7}$$

where $A_P = \int_\Omega \phi(\boldsymbol{x}) d\boldsymbol{x}$ is the area of the piezoelectric patch, and $f(\boldsymbol{x}) = \phi(\boldsymbol{x})\psi(\boldsymbol{x})$ is introduced to simplify the notation by lumping the ϕ and ψ functionals together.

2.2.3 Plane Wave Sensing

The sensed voltage of Equation (7) can then be evaluated in presence of a plane harmonic wave propagating field at a frequency ω, Figure 6. Within this scenario, the surface displacement can be generally expressed as

$$\boldsymbol{u}(\boldsymbol{x}, \omega) = \boldsymbol{U}_0(\omega) e^{-j\boldsymbol{k}_0(\omega)\cdot\boldsymbol{x}} \tag{8}$$

where $\boldsymbol{U}_0$ defines amplitude and polarization of the wave at the considered frequency, and $\boldsymbol{k}_0(\omega) = k_0 \boldsymbol{i}_1^{'}$ is the wave vector defining plane wave propagation at an angle ϑ. Assuming that $\boldsymbol{u} \cdot \boldsymbol{i}_2^{'} = 0$, as it can be intuitively seen from Figure 6, the only strain component relevant to the surface-mounted sensor is

$$\varepsilon_{1'1'} = \frac{\partial u_1'}{\partial x_1'} = jU_{1_0'}(\omega) k_0(\omega) e^{-jk_0(\omega)x_1^{'}} \tag{9}$$

while $\varepsilon_{2'2'} = \gamma_{1'2'} = 0$ as discussed in [54]. The strain field can then be written as

$$\boldsymbol{\varepsilon} = \varepsilon_{1'1'} \boldsymbol{r}(\vartheta) \tag{10}$$

where $\boldsymbol{r}(\vartheta) = [\cos^2 \vartheta, \sin^2 \vartheta, 0]^T$.

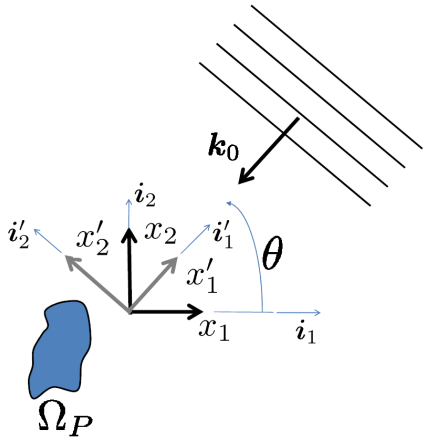

Figure 6: Schematic of plane wave propagating at an angle ϑ.

Finally, substituting Equation (10) into Equation (7) yields

$$V(\omega) = jU_{1_0'}(\omega) k_0(\omega) \mathcal{H}(\vartheta) \mathcal{D}(\boldsymbol{k}(\omega), \vartheta) \tag{11}$$

where

$$\mathcal{H}(\vartheta) = \frac{t_P}{A_P} \frac{\boldsymbol{b}^T \boldsymbol{d}^{\sigma} \boldsymbol{C}^E \boldsymbol{r}(\vartheta)}{\left[\boldsymbol{b}^T (\boldsymbol{d}^{\sigma} \boldsymbol{C}^E \boldsymbol{d}^{\sigma^T} - \boldsymbol{\varepsilon}^{\sigma}) \boldsymbol{b}\right]} \tag{12}$$

contains the electromechanical properties and thickness of the sensor patch [54, 44]. To better understand the role played by this term, consider as an example a patch featuring strongly anisotropic material properties, where the 0° direction is much stiffer than the 90°

one. In this scenario the role of $\mathcal{H}(\vartheta)$ is such that the voltage sensed by the device would be much higher for the sensing of a traveling wave coming from a 0° direction rather than 90° one. Generalizing this idea, $\mathcal{H}(\vartheta)$ can be effectively considered as a material-related term that acts upon the voltage reading on the piezoelectric patch, i.e. a material-related directionality.

Also in Equation (11)

$$\mathcal{D}(\boldsymbol{k}(\omega),\, \vartheta) = \int_{\Omega} e^{jk_0(\omega)(x_1 \cos\vartheta + x_2 \sin\vartheta)} f(\boldsymbol{x}) d\boldsymbol{x} \tag{13}$$

describes the effect of the electrode distribution as defined by $f(\boldsymbol{x})$. The term $\mathcal{D}(\boldsymbol{k}(\omega),\, \vartheta)$ can be regarded as a geometry-related term that acts upon the voltage reading on the piezoelectric patch, i.e. a shape-related directionality.

It is worth noting that Equation (13) can be rewritten as

$$\mathcal{D}(\omega,\, \vartheta) = \int_{-\infty}^{+\infty} e^{j\boldsymbol{k}_0(\omega)\cdot\boldsymbol{x}} f(\boldsymbol{x}) d\boldsymbol{x} \tag{14}$$

where the limited spatial support of $f(\boldsymbol{x})$ is exploited to extend the integration limits to infinity. Its frequency dependence is based on the dispersion relation $\boldsymbol{k}_0 = \boldsymbol{k}_0(\omega)$.

Equation (14) can be easily recognized as the spatial Fourier Transform (FT) of $f(\boldsymbol{x})$. Patch directional sensing can thus be associated with electrode shaping and internal polarization through the estimation of the FT pair

$$\mathcal{D}(\boldsymbol{k}_0(\omega),\, \vartheta) = \mathcal{F}[f(\boldsymbol{x})] \tag{15}$$

where $\mathcal{F}[\,\cdot\,]$ denotes the FT.

A closer look at Equation (15) suggests the possibility to evaluate sensor directivity through FFT algorithms. More in detail, given a desired directivity function in the wavenumber domain, it is possible to obtain the corresponding sensor geometrical, or spatial, shape by means of the Inverse Fourier Transformation (IFT)

$$f(\boldsymbol{x}) = \mathcal{F}^{-1}[\mathcal{D}(\boldsymbol{k}_0(\omega),\, \vartheta)] \tag{16}$$

where $\mathcal{F}^{-1}[\,\cdot\,]$ denotes the IFT.

2.3 Actuation Mode for an Arbitrarily Shaped Piezoelectric Patch

With the sensing framework in place, a general approach to obtain the directivity associated with an arbitrary shaped patch in actuation mode is now presented. The system under consideration is the same as the one described in Section 2.2.1. In here the piezoelectric patch is assumed to provide external inputs to the elastic medium without interfering with its dynamic behavior [63].

The elastic medium under consideration is assumed to be (i) homogeneous, (ii) isotropic, and (iii) able to sustain the propagation of a wave of phase velocity $c(\omega)$, the dependence of c on ω being directly related to the dispersive properties of the medium.

In this context, each infinitesimal actuation element $d\Omega = dx_1 dx_2$ of Ω_P is considered as a point source capable to generate a harmonic signal in the time domain, $g(t) = g_0(\omega)e^{-j\omega t}$, where g_0 is directly related to the voltage applied to the piezo patch. The analysis considers far field radiation, so that each piezoelectric infinitesimal element generates a wave which can be considered as plane at the point of interest, as represented in Figure 7.

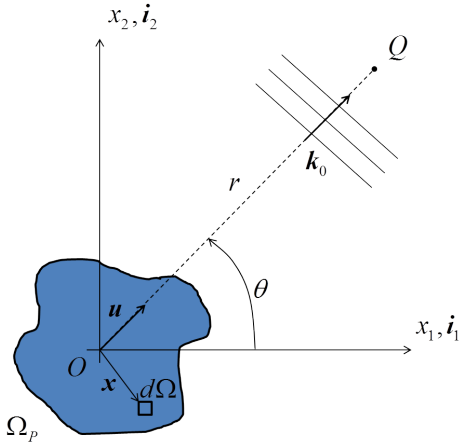

Figure 7: Plate with arbitrarily shaped piezoelectric actuator bonded on the top surface.

The infinitesimal response at a generic point Q, whose position vector is $\boldsymbol{r} = r\boldsymbol{u}$, due to a harmonic excitation of an element $d\Omega$ placed in the origin O, with position vector $\boldsymbol{x}_O$, can be expressed, dropping the harmonic term, as

$$dw(\boldsymbol{r}, \boldsymbol{x}_O, \omega) = g_0(\omega)\mathcal{G}(\boldsymbol{r}, \boldsymbol{x}_O, \omega)d\Omega \tag{17}$$

where $\mathcal{G}(\boldsymbol{r}, \boldsymbol{x}_O, \omega)$ is an appropriate Green's function [30]. For simplicity $\mathcal{G}(\boldsymbol{r}, \boldsymbol{x}_O, \omega)$ it can be expressed by the definition of a geometric loss factor combined with a phase shift due to the wave traveled distance

$$\mathcal{G}(\boldsymbol{r}, \boldsymbol{x}_O, \omega) = \frac{1}{\sqrt{|\boldsymbol{r} - \boldsymbol{x}_O|}} e^{j\omega\tau_O} \tag{18}$$

with τ_O denoting the propagation time from the source O to Q. Under the single mode propagation assumption, the propagation time can be expressed as

$$\tau_O = \frac{r}{c(\omega)}. \tag{19}$$

The infinitesimal response at Q due to a source $d\Omega$ placed at a generic $\boldsymbol{x}$ can be written as

$$dw(\boldsymbol{r}, \boldsymbol{x}, \omega) = g_0(\omega) f(\boldsymbol{x}) \mathcal{G}(\boldsymbol{r}, \boldsymbol{x}, \omega) d\Omega \tag{20}$$

where $f(\boldsymbol{x})$ defines the distribution of active material as introduced in Section 2.2.2. Also, similarly as in Equation (18), $\mathcal{G}(\boldsymbol{r}, \boldsymbol{x}, \omega)$ is expressed as

$$\mathcal{G}(\boldsymbol{r}, \boldsymbol{x}, \omega) = \frac{1}{\sqrt{|\boldsymbol{r} - \boldsymbol{x}|}} e^{j\omega\tau_x} \tag{21}$$

where τ_x is the propagation time.

Within the far field assumption, τ_x can be expressed in terms of τ_O through a set of geometrical considerations based on the schematic of Figure 8. In particular, by assuming parallel wave fronts for the waves generated point-wise within the patch, the relation between τ_x and τ_O can be approximated as

$$\tau_x \approx \frac{r - \boldsymbol{u} \cdot \boldsymbol{x}}{c(\omega)} \approx \tau_O - \frac{\boldsymbol{u} \cdot \boldsymbol{x}}{c(\omega)} \tag{22}$$

where $\boldsymbol{u} = \boldsymbol{u}(\vartheta) = [\cos(\vartheta), \quad \sin(\vartheta)]^T$ is the direction cosines of vector $\boldsymbol{r}$, and $\boldsymbol{x}$ is the position of the generic piezoelectric element. In addition to this

$$\frac{1}{\sqrt{|\boldsymbol{r} - \boldsymbol{x}|}} \approx \frac{1}{\sqrt{|\boldsymbol{r} - \boldsymbol{x}_O|}} \tag{23}$$

and, therefore

$$\mathcal{G}(\boldsymbol{r}, \boldsymbol{x}, \omega) \approx \mathcal{G}(\boldsymbol{r}, \boldsymbol{x}_O, \omega) e^{-j\frac{\omega}{c(\omega)}\boldsymbol{u}\cdot\boldsymbol{x}} \tag{24}$$

Given this framework, the response given by the entire piezoelectric patch can be expressed invoking the superposition principle

$$\begin{aligned} w(\boldsymbol{r},\omega) &= \int dw(\boldsymbol{r},\boldsymbol{x},\omega) \\ &= \int_{\Omega_P} g_0(\omega) f(\boldsymbol{x}) \mathcal{G}(\boldsymbol{r},\boldsymbol{x}_O,\omega) e^{-j\frac{\omega}{c(\omega)}\boldsymbol{u}\cdot\boldsymbol{x}} d\Omega \\ &= g_0(\omega)\mathcal{G}(\boldsymbol{r},\boldsymbol{x}_O,\omega)\mathcal{D}(\boldsymbol{k}(\omega),\vartheta) \end{aligned} \tag{25}$$

where

$$\mathcal{D}(\boldsymbol{k}(\omega),\vartheta) = \int_{\Omega_P} f(\boldsymbol{x}) e^{-j\frac{\omega}{c(\omega)}\boldsymbol{u}\cdot\boldsymbol{x}} d\Omega \tag{26}$$

contains the directionality contribution due to the geometrical arrangement of the piezoelectric material. By noting that $\boldsymbol{k}_0(\omega) = \frac{\omega}{c(\omega)}\boldsymbol{u}$ by the definition of the dispersion relation, and by exploiting the limited support of $f(\boldsymbol{x})$, Equation (26) can be rewritten as

$$\mathcal{D}(k(\omega),\vartheta) = \int_{-\infty}^{+\infty} f(\boldsymbol{x}) e^{-j\boldsymbol{k}_0(\omega)\cdot\boldsymbol{x}} d\Omega \tag{27}$$

which can be recognized as the spatial FT of the function $f(\boldsymbol{x})$. The obtained result is thus the same to the one of Equation (14). This shows the duality between sensing and actuation, as expected by acoustic reciprocity principles.

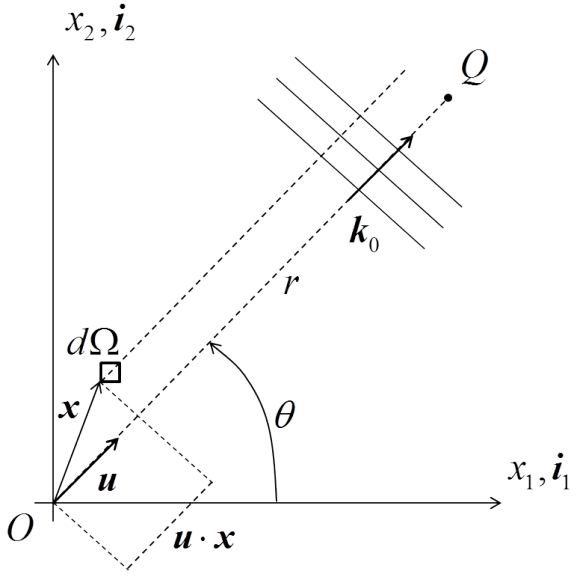

Figure 8: Far field approximation.

2.4 Examples of Directivities for Simple Geometries

In summary, the following statements can be outlined:

- In sensing, directivity maxima provide the dominant frequency component(s) that depend on the the direction of incoming waves;
- In actuation, directivity maxima provide the excitation frequencies suitable to generate waves along specific directions.

The geometry-related directivities of (i) a circular patch, and (ii) a rectangular patch are now illustrated as simple examples of how the electrode shape determines the directivity associated with the transducer.

2.4.1 Circular Patch

The simplest case that one can think of is represented by a circular piezoelectric patch, for which the function $f(\boldsymbol{x})$ assumes the following expression:

$$f(\boldsymbol{x}) = \text{rect}\left(\frac{|\boldsymbol{x}|}{a}\right) \tag{28}$$

where the function $\text{rect}(\cdot)$ is defined as follows:

$$\text{rect}(\xi) = \begin{cases} 1, & |\xi| \leq 1 \\ 0, & |\xi| > 1 \end{cases} \tag{29}$$

and where a represents the radius of the patch. Figure 9(a) shows a configuration with $a = 5$ mm. The corresponding directivity can be computed analytically and it assumes the following expression

$$\mathcal{D}(\boldsymbol{k}(\omega), \vartheta) = 2\pi a^2 \frac{J_1(a|\boldsymbol{k}_0|)}{a|\boldsymbol{k}_0|} \tag{30}$$

where $J_1(x)$ is the first order Bessel function.

The directivity function of Equation (30), which is represented in Figure 9(b), shows that the directionality amplitude follows a radial variation that presents both peaks (represented by white dashed lines) and valleys (represented by the white solid line). These features are linked with the sensing/actuation authority of the patch. In particular, the

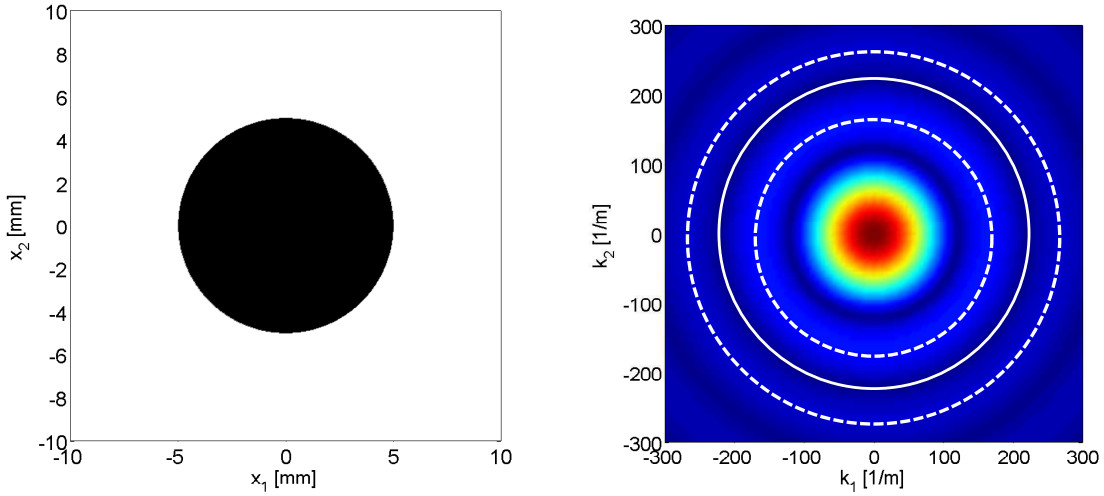

(a) (b)

Figure 9: (a) Circular piezo disc of radius $a = 5$ mm. (b) Wavenumber representation of the directivity function associated to the piezo disk. Dashed white lines: local maxima of the Bessel function.

sensing/actuation authority presents (i) maximum values in correspondence of the peaks, which, in turn, represent the tuning conditions for the patch, and (ii) minimum values in correspondence of the valleys. Moreover, peaks and valleys in the wavenumber domain can be coupled to frequency values for specific wave modes through medium dispersion relations, thus generating a frequency-based directionality. In light of this, it can be stated that the circular patch of Figure 9 shows the absence of any particular directionality and indicates that preferential, although isotropic, tuning occurs for frequencies associated to wave modes that lay on local maxima of the Bessel function.

2.4.2 Rectangular Patch

The analytical framework developed above is now applied to the case of a rectangular patch. In this case, the geometry of the patch can be described by the following function

$$f(\boldsymbol{x}) = \text{rect}\left(\frac{x_1}{a}\right) \text{rect}\left(\frac{x_2}{b}\right) \tag{31}$$

where $2a$ and $2b$ define the dimensions of the patch along the x_1 and x_2 directions, as reported in Figure 10(a). The shape-related transducer directivity can be analytically de-

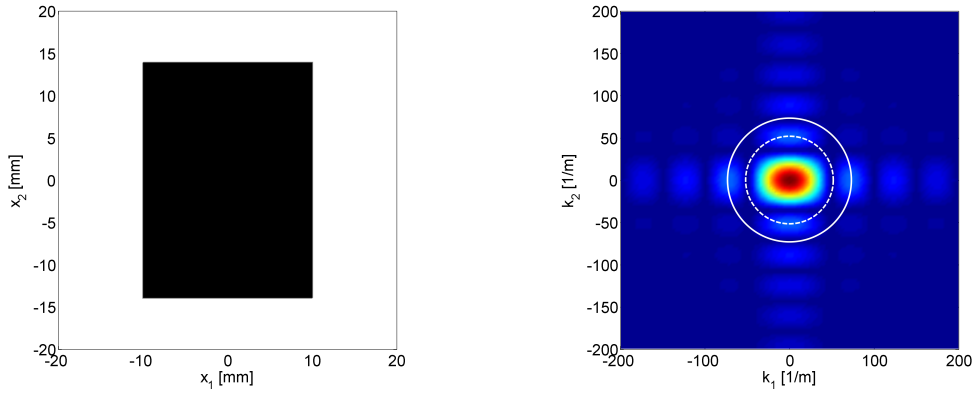

(a) (b)

Figure 10: (a) Spatial representation of a rectangular piezo patch of dimensions $a = 10$ mm, and $b = 14$ mm. (b) Corresponding wavenumber representation. Dashed white line: tuning condition for $k_0^{(1)}$. Solid white line: tuning condition for $k_0^{(2)}$.

termined to be given by

$$\mathcal{D}(\boldsymbol{k}_0(\omega), \vartheta) = a\, b\, \mathrm{sinc}(ak_0 \cos\vartheta)\, \mathrm{sinc}(bk_0 \sin\vartheta) \tag{32}$$

which indicates that preferential directions of sensing/actuation are aligned with the rectangle edges. Tuning occurs for wavenumber values that maximize the $sinc(\cdot)$ functions in Equation (32). Directivity maxima occur for (i) wavenumbers $k_0^{(1)} = (2n-1)\frac{\pi}{2a}$ corresponding to a traveling wave at $\vartheta = 0°$, and (ii) wavenumbers $k_0^{(2)} = (2n-1)\frac{\pi}{2b}$ corresponding to a traveling wave at $\vartheta = 90°$, where n is integer-valued. Tuning conditions for $k_0^{(1)}$ and $k_0^{(2)}$ are represented in Figure 10(b) by dashed and solid white lines, respectively.

Wavenumber information can be directly related to frequency values through the dispersion relations of the underlying medium. For example, in actuation mode, the transducer would be able to generate waves that, based on the frequency value of the applied excitation voltage, will travel in the directions of maximum sensitivity.

2.4.3 Experimental Evaluation of Rectangular Patch Directionality

The performance of the transducer described above and of dimensions depicted in Figure 10(a) is evaluated experimentally. The objective of the tests is to reconstruct the directivity functions associated with the patch when used in actuation mode, and show

that the electrode, rather than the overall piezoelectric material, shape is responsible of defining the directivity associated with the transducer.

The transducer rectangular electrode is manufactured by means of the Toner Transfer Method (TTM), detailed in Section 3.3.3, which is adopted here to manufacture a rectangular electrode out of a circular PZT wafer of 63.5 mm diameter and 0.19 mm thick initially coated with 200 nm thick nickel electrodes (Piezo Systems, Inc.). The resulting transducer is then vacuum bonded with bi-component high strength epoxy (Loctite® Epoxy Adhesive, Hysol E-20HP) to a 0.81 mm thick aluminum plate, as pictured in Figure 11.

(a) (b)

Figure 11: (a) Vacuum bonding technique employed to mechanically bond the transducer to the hosting structure. (b) Transducer attached to the plate with the rectangular electrode clearly visible.

The plate with the transducer bonded at its center is then prepared for testing in actuation mode. The input voltage signal is provided by an amplified signal coming from a function generator (Agilent 33220A) and the wave propagation field is recorded with a Scanning Laser Doppler Vibrometer (SLDV). Reflective tape is applied on the side opposite to the one with the transducer to enhance the quality of the laser measurements.

The analysis considers the successive application of 7 cycles, Hanning-windowed, tone bursts, Figure 12(a), centered at different frequencies, to verify the radiation patterns as predicted by Equation (32). In each case, the perturbations generated by the transducer are recorded at scan points located along a circle with 100 mm radius and centered at the transducer location, Figure 12(b). Radiation patterns are evaluated constructing polar

energy plots of the RMS values of the points time history acquired along the scan path. The frequencies selected for the excitation are the ones associated to wavenumber directivity maxima of Equation 32, and are reported in Table 1 for convenience.

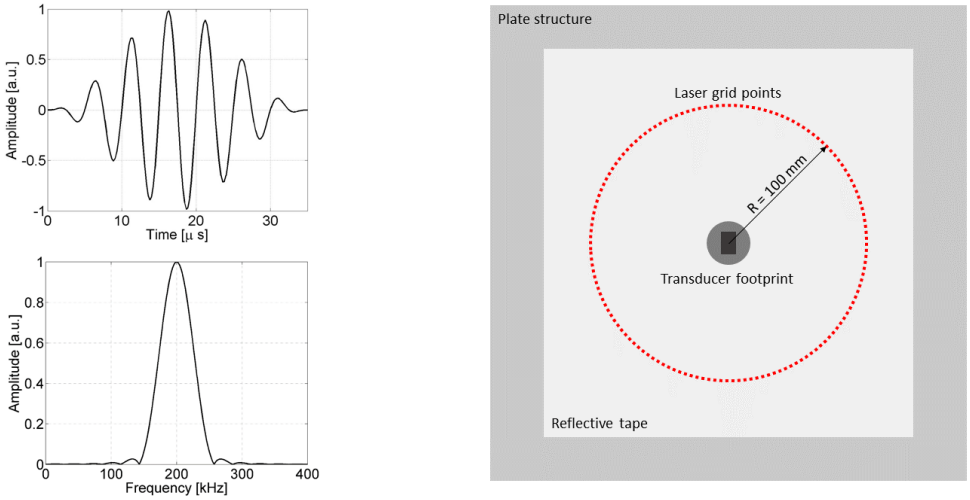

(a) (b)

Figure 12: (a) 200 kHz 7-cycles Hanning-windowed excitation signal fed to the rectangular actuator. Top figure: time domain. Bottom figure: corresponding frequency spectrum. (b) Circular scan mock-up for directionality estimation of radiation from the rectangular patch.

Table 1: First eight values of wavenumber maxima associated with the rectangular patch, and corresponding frequencies. Tests featuring $n = 1$ have not been performed because the associated wavelength with such low frequencies would have been too long.

n	$k_0^{(1)}$ (rad/m)	$f_0^{(1)}$ (kHz)	$k_0^{(2)}$ (rad/m)	$f_0^{(2)}$ (kHz)
1	157.1	4.6	112.2	2.2
2	471.2	42.8	336.6	21.8
3	785.4	115.4	561.0	60.3
4	1099.6	215.1	785.4	115.4

A representative selection of the results collected experimentally is reported in Figure 13 under the form of polar plots. As it can be seen, the matching of the directionality recorded by the experimental energy plots with the theoretical results is excellent for a broad frequency spectrum that goes from 21.8 kHz to 215.1 kHz. In particular, the main directionality lobes get captured consistently throughout the frequency bandwidth under investigation,

while some discrepancies can be observed on the secondary (smaller) lobes. This distortion is believed to be associated (i) with the presence of the epoxy bonding layer, which introduces a shear-lag phenomenon not considered in the analytical developments, and (ii) with the appearance of non-linear piezoelectric effects facilitated by the high-voltages used to drive the device in actuation mode. These results validate the directionality framework from an experimental standpoint, showing that custom electrode layouts can be shaped out of a monolithic piezoelectric wafer without significant loss of directionality associated to the patch geometrical arrangement.

2.5 Conclusions

In this chapter, the equations for sensing of Lamb waves by piezo patches of arbitrary shapes have been provided. Under the assumptions of (i) thin piezo patches, (ii) propagating plane waves, and (iii) through-the-thickness polarization of the piezo material, an expression of the transducers directivity has been formulated based on the spatial distribution of active material, valid for both wave sensing and actuation, in agreement with acoustic reciprocity principles. Directivities for simple transducers configurations such as (i) circular patch, and (ii) rectangular patch have been evaluated as introductory examples that provided the basic tools for further transducer design analysis.

In the next chapter the concept of frequency-based beam steering is introduced through the presentation of the spiral FSAT concept in actuation mode. To this aim, the existing framework is expanded and ported to composite materials, and anisotropic active layers. Numerical and experimental validations of the devices are then presented in support of the efforts performed towards the design of the transducers.

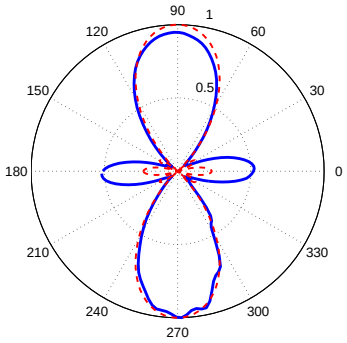

(a) f = 21.8 kHz

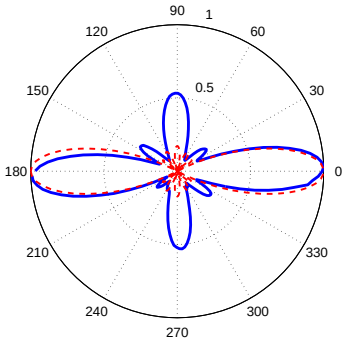

(b) f = 42.8 kHz

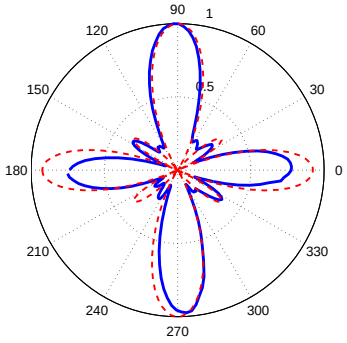

(c) f = 60.3 kHz

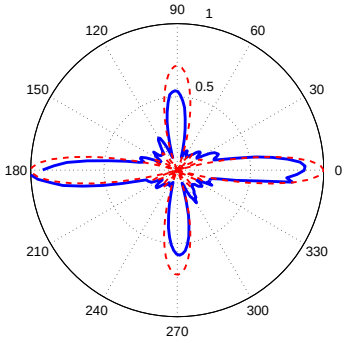

(d) f = 115.4 kHz

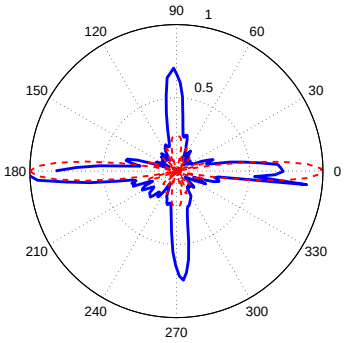

(e) f = 215.1 kHz

Figure 13: Rectangular patch directionality at selected frequencies. Blue solid line: experimental. Red dashed line: analytical.

CHAPTER III

SPIRAL FREQUENCY STEERABLE ACOUSTIC TRANSDUCERS FOR GUIDED WAVE ACTUATION

3.1 Overview

This chapter presents the study of actuation capabilities of spiral Frequency Steerable Acoustic Transducers (FSATs). Firstly, the concept of frequency-based beam steering is introduced by outlining the principles of operation of spiral FSAT devices. Then, the development of monolithic piezo wafer-based FSATs is illustrated for applications to both isotropic, and anisotropic plates, where it is shown how spiral FSATs electrode layouts can be shaped out of a monolithic piezoelectric wafer without significant loss of directionality. Finally, the spiral FSAT design technique is adapted to incorporate piezo-fibrous active layers, which confers conformability properties to the transducer, thus extending its application range. Both numerical/analytical and experimental studies are conducted to validate the actuation performance of the devices, and, in the process, a simple and powerful fabrication technique is outlined for the manufacturing of complex electrode shapes out of monolithic piezoelectric wafers.

3.2 Introduction to FSAT Principles of Operation

The FSAT design idea stems from the frequency-dependent directivity of Equation (15), which suggests the possibility of designing the material distribution to achieve a desired directionality for specific frequencies. This is done by specifying the shape of the transducer in the wavenumber domain, and subsequently exploiting Equation (16) to retrieve the corresponding spatial distribution of active material.

For continuous beam steering between two angles that define an angular sector, the desired directivity traces a spiral in the wavenumber domain. This shape allows for iso-frequency circles representing dispersion relations for isotropic media to intercept a single

directivity maximum for a given wave vector, thus univocally identifying a single direction of sensing/radiation. The schematic represented in Figure 14 shows the intersection of a potential spiraling material distribution (represented by blue circles) that covers an angular sector that goes from ϑ_m to ϑ_M with three iso-frequency circles. This illustrates how increasing wavenumbers, and thus frequencies, correspond to transducer sensitivity at increased angles of directionality.

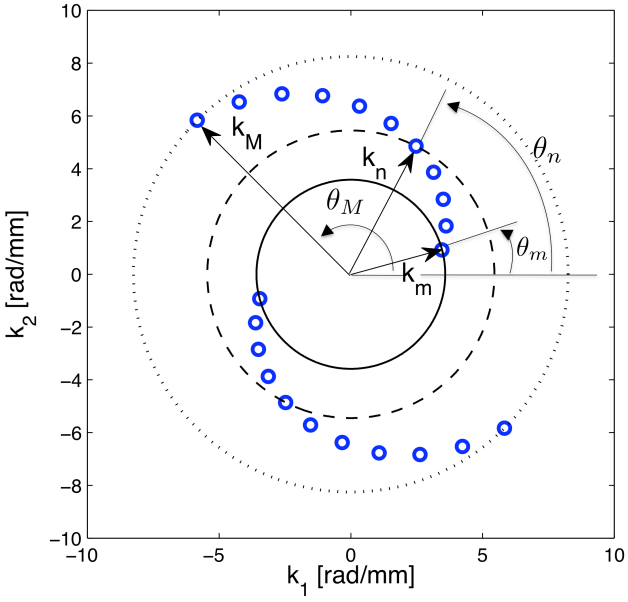

Figure 14: Schematic of spiral directivity in the wavenumber domain for the case of isotropic materials.

The shape-related directivity function in the wavenumber domain is expressed as

$$\mathcal{D}(\boldsymbol{k}_0(\omega),\, \vartheta) = -j\frac{a}{N}\sum_{n=1}^{N}\left[\frac{J_1(a|\boldsymbol{k}_0 - \boldsymbol{k}_n|)}{a|\boldsymbol{k}_0 - \boldsymbol{k}_n|} - \frac{J_1(a|\boldsymbol{k}_0 + \boldsymbol{k}_n|)}{a|\boldsymbol{k}_0 + \boldsymbol{k}_n|}\right] \tag{33}$$

where a represents the patch radius in the spatial domain, $J_1(x)$ is the first order Bessel function, and $\boldsymbol{k}_n$ denotes the wave vector corresponding to the angle ϑ_n, at which the $n-th$ maximum of the transducer is located in the wavenumber domain (blue circles in Figure 14).

Adopting a spiral wavenumber distribution, the location of $\boldsymbol{k}_n = \boldsymbol{k}_n(\vartheta_n)$ is given by

$$\boldsymbol{k}_n(\vartheta_n) = \left[(k_M - k_m)\frac{\vartheta_n - \vartheta_m}{\vartheta_M - \vartheta_m} + k_m\right](\cos\vartheta_n \boldsymbol{i}_1 + \sin\vartheta_n \boldsymbol{i}_2) \tag{34}$$

which is the shape of an Archimedean spiral [86] defined in terms of minimum and maximum values of the wave vector amplitude, respectively k_m and k_M. These values are to be selected

at the design stage and they essentially define the spiral FSAT frequency bandwidth. Such bandwidth is defined by k_m, k_M, and the medium dispersion relations.

The analytical expression for the spatial distribution of the piezoelectric material given by Equation (33) can be obtained analytically through an IFT, Equation (16). This operation results in the following expression

$$f(\boldsymbol{x}) = \frac{1}{N}\text{rect}\left(\frac{|\boldsymbol{x}|}{a}\right)\sum_{n=1}^{N}\sin(\boldsymbol{k}_n \cdot \boldsymbol{x}) \tag{35}$$

where a is the patch radius, and $\boldsymbol{k}_n$ denotes the wave vector corresponding to the angle ϑ_n, at which the $n-th$ maximum of the transducer is located in the wavenumber domain. It is worth noting that the spatial distribution described by Equation (35) is not practical from a manufacturing standpoint, since it features a continuous electrode distribution that would require material and/or polarization grading to manufacture. A simple strategy to overcome this problem is to apply a thresholding procedure to the spatial distribution $f(\boldsymbol{x})$, and transform it into a "quantized" constant-valued function distributed over the transducer domain. A threshold value η is introduced as a percentage of the maximum value assumed by $f(\boldsymbol{x})$. In this way, the final distribution of material in the spatial domain is described as

$$\bar{f}(\boldsymbol{x}) = \begin{cases} 1, & f(\boldsymbol{x}) \geq \eta \\ 0, & f(\boldsymbol{x}) < |\eta| \\ -1, & f(\boldsymbol{x}) \leq -\eta \end{cases} \tag{36}$$

where $\bar{f}(\boldsymbol{x})$ represents the quantized constant valued version of $f(\boldsymbol{x})$, being η the threshold level. This is chosen based on manufacturing consideration and constraints, such as electrode spacing to avoid electric shorting. This thresholding procedure generally affects the transducer directionality function by introducing side lobes that arise on the sides of the spiral material distribution [74]. Despite of this, the directionality associated with the spiral layout of the material is completely preserved. In addition, being the procedure required from a manufacturing standpoint, the thresholding is implied for the remaining of this work when electrodes patterns are to be generated, and $f(\boldsymbol{x})$ is often used in place of $\bar{f}(\boldsymbol{x})$.

3.3 Monolithic Design on Piezo-ceramic Substrate for Isotropic Plates

The spiral directionality can be seen as a way to confer spatial filtering properties to the transducer. These properties can be ultimately converted to frequency information through the dispersion relations of the considered medium. This makes the design flexible and tailorable to specific applications. Dispersion relations of Lamb waves in isotropic plates are considered in the following section due to their extensive use in damage detection.

3.3.1 Design

The spiral FSAT is designed to operate in a frequency range where wave propagation consist in the superposition of the first anti-symmetric (A_0) and first symmetric (S_0) Lamb wave modes. The dispersion relations of both modes for an aluminum plate with a thickness of 0.81 mm are presented in Figure 15, where the design bandwidth of the device is also highlighted. The resulting transducer features a frequency bandwidth that ranges from 50 kHz to 350 kHz while spanning an angular sector that goes from 0° to 180°. For this configuration, the spiral material layout in the wavenumber domain is reported in Figure 16(a), where $N = 90$ guarantees a continuous spiraling of the material layout. The corresponding spatial electrode configuration, which has a radial extension of $a = 30$ mm, is represented in Figure 16(b) after thresholding. For this configuration, the directionality-frequency map associated with the device is reported in Figure 17.

3.3.2 Numerical Analysis of Directional Performance

In order to correctly capture the transducer behavior, it is crucial to accurately model the propagation of transient elastic waves within a plate-like domain featuring a complex piezoelectric arrangement bonded to one of its sides. Simulation techniques such as the application of in-plane nodal forces at the electrodes edges [71] to mimic the presence of a piezoelectric transducer would result impractical to implement given the complexity of the electrode geometry. A more practical idea exploits a simulation environment that allows to model coupled piezoelectric behavior. For this reason, the transducer directionality performance is assessed by means of COMSOL Multiphysics®. This software allows to

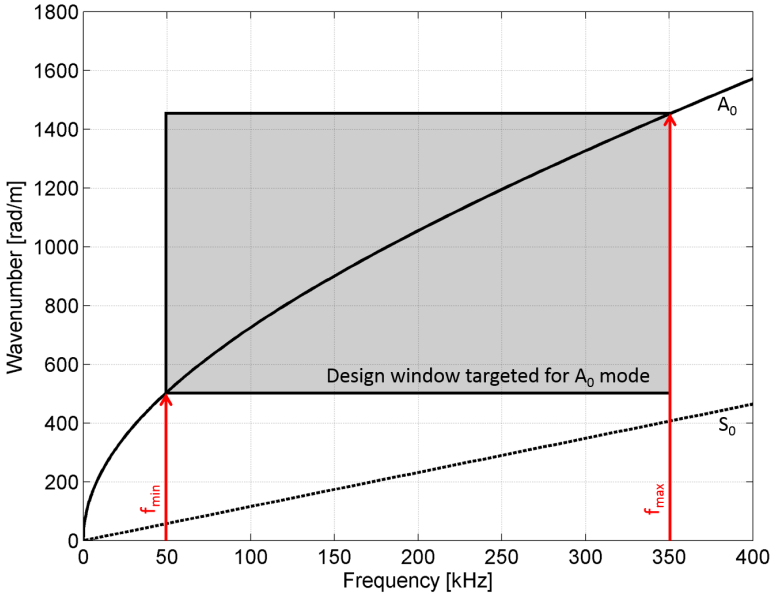

Figure 15: Dispersion relations for an aluminum plate with a thickness of 0.81 mm. Grey area: transducer operating bandwidth.

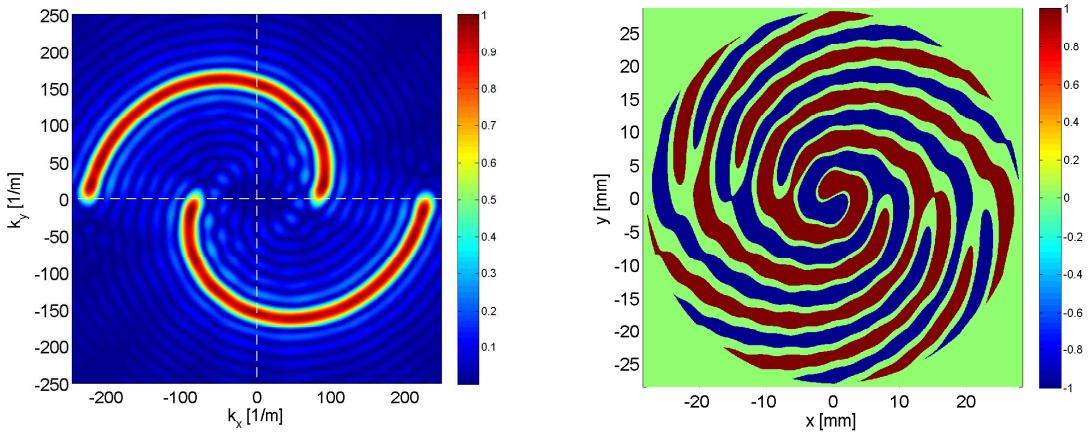

(a) (b)

Figure 16: Design steps for the spiral FSAT material distribution. (a) Wavenumber representation of the spiral FSAT. (c) Final spiral FSAT electrodes shape (threshold level $\eta = 8.2\%$). Red and blue correspond to positive and negative electrode, respectively.

account for coupled or multiphysics phenomena, making it an excellent choice for numerical simulations of the problem under analysis. The implementation of coupled piezo-elastic simulations to verify the FSAT directional performance are made possible by the COMSOL piezoelectric devices interface, that combines solid mechanics and electrostatics modeling

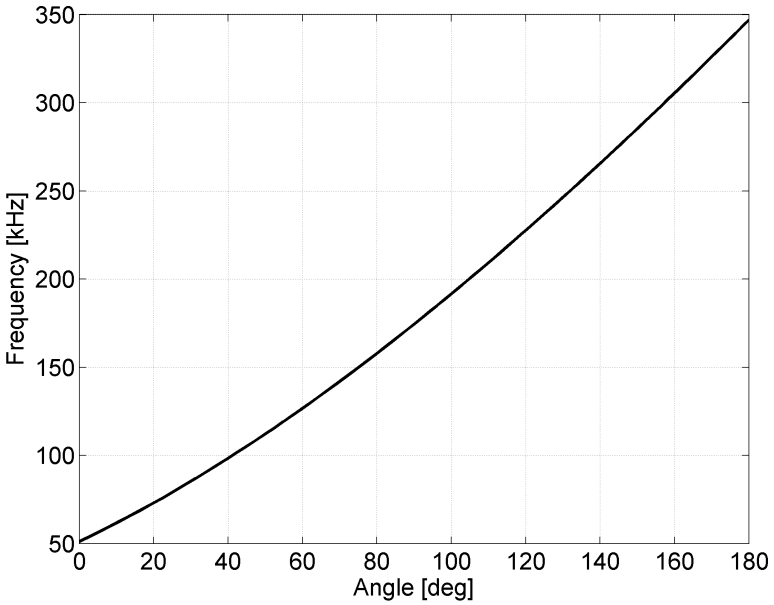

Figure 17: Spiral FSAT directionality-frequency map based on the A_0 Lamb mode in a 0.81 mm thick aluminum plate.

capabilities into a fully coupled tool for modeling piezoelectric materials.

The geometry of the FE model implemented is reported in Figure 18. The excitation input is provided to the electrodes under the form of voltage difference with respect to the ground electrode, which is in direct contact with the top surface of the plate. The signal consists of a 4-cycles Hanning-windowed Tone Burst (TB) with a maximum amplitude of 200 V. Piezoelectric constitutive relations are applied to the active layer of the transducer, for which the piezo-elastic properties of PZT-5A are used. PZT-5A piezoceramics, along with PZT-5H, are the most commonly used piezoceramics to perform GWs transduction in SHM applications. Their typical three-dimensional piezo-elastic properties can be found in [99, 35].

The FE discretization of the elastic plate and transducer is performed by means of COMSOL auto-meshing sequence set on physics-controlled mesh with a maximum element size set to 11 mm. The total number of degrees of freedom for the problem under consideration is 1397030. The FE discretization is then coupled with a transient solution procedure that yields the required piezo-elasto-dynamic response. For each analysis, the total simulation

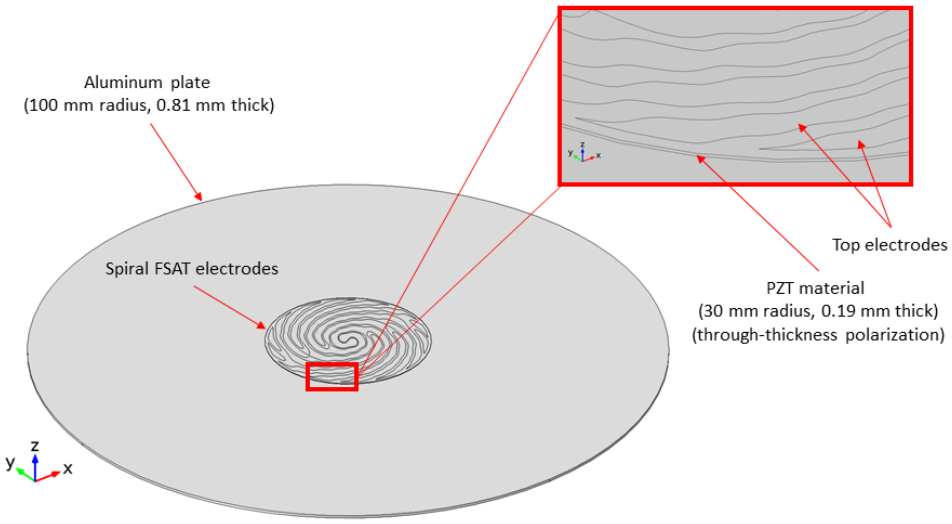

Figure 18: FE model geometry implemented to study elastic wave propagation generated by the FSAT device.

time corresponds to five times the duration of the Tone Burst (TB) used for excitation. Each FE analysis run takes approximately 4 h and 18 GB of RAM on a 12 cores workstation with 64 GB of RAM. The results of the simulations are presented in Figure 19 in terms of out-of-plane displacement at selected time instants for three bursts center frequencies: 50 kHz, 150 kHz, and 250 kHz.

The results are also presented in terms of time Root Mean Square (RMS) of the out-of-plane displacement interpolated on a circular grid of 100 mm radius centered at the transducer location. The comparison with analytical directionality predictions are reported in Figure 20 for the three frequencies analyzed.

As it can be seen, numerical results are in very good agreement with analytical predictions. Also, the directionality beam associated with the FE model is wider than the analytical one. This is due to the fact that from an analytical standpoint, the directionality function is extracted for a single frequency, i.e. for the TB central frequency. Conversely, in the FE simulations, the directionality is associated to the full spectrum of the TB signal, which spans a finite band around its central frequency (see for example Figure 12). For this reason, the directionality beam is wider in the results extracted from the FE analyses. It is

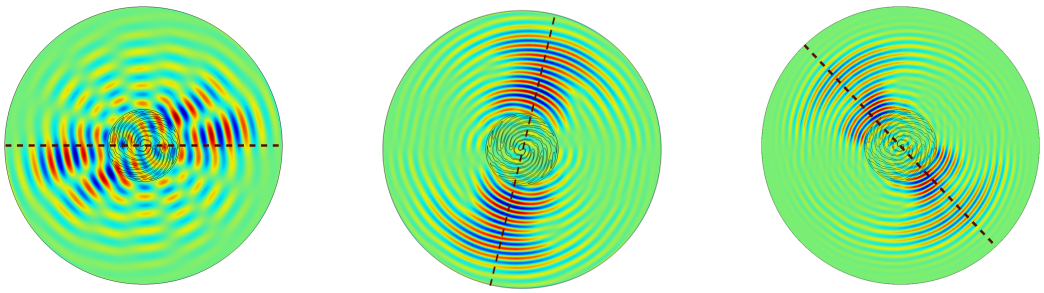

(a) f = 50 kHz (b) f = 150 kHz (c) f = 250 kHz

Figure 19: Piezo-elastic FE model results in terms of out-of-plane plate displacement at selected time instants. Dark red dashed lines: analytical directionality predictions.

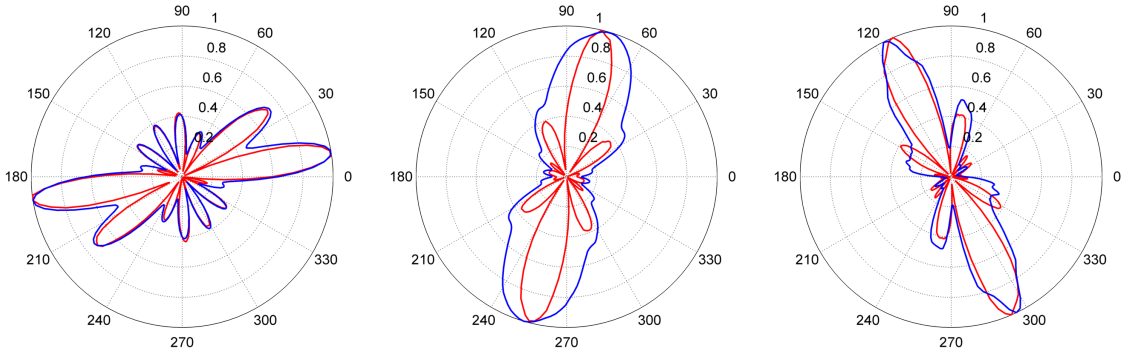

(a) f = 50 kHz (b) f = 150 kHz (c) f = 250 kHz

Figure 20: Piezo-elastic FE model results in terms of out-of-plane plate displacement RMS at selected frequencies. Blue line: numerical directionality. Red line: analytical directionality.

worth noting that the choice of an excitation signal with an increased number of cycles, e.g. a 7-cycles TB, would help mitigating this effect. The choice of a 4-cycles TB is a trade-off solution between the needs of (i) limiting the computational cost of the FE model, and (ii) increasing the radial dimension of the plate to be able to analyze a traveling wave without significant perturbations from boundaries reflections.

In conclusion, it can be stated that frequency dependent directional performance of the spiral FSAT is confirmed by numerical evidence, and the agreement with analytical predictions is very good.

3.3.3 Fabrication

The prototype discussed herein is specifically designed for actuation applications, and the active layer consists of a monolithic piezoelectric wafer, which provides excellent actuation authority for wave generation purposes [27]. Prior manufacturing, electrode areas grouping needs to be performed, so that all the branches associated to the electrode that have same polarization value (red and blue areas in Figure 16(b)) are electrically connected. This is done for example by importing the geometry in a CAD environment, such as AutoCAD, and manually connecting the areas together.

For manufacturing, two solutions can be adopted. The most direct one would be to image the spatial distribution of the electrode, which has both positive and negative polarization, on one side of a piezo wafer and perform a re-polarization with inverted signs for the two electrode groups while the other side of the wafer provides the common ground. This would allow a parallel electric connection between the two electrode groups, which is the easiest electrical implementation for the design of the circuitry needed to power to the device. Although this might seem convenient at first, commercially available piezo wafers already come pre-polarized through-the-thickness, and for this reason, in order to avoid the non-trivial re-polarization process, a different solution is implemented.

In this second solution, the electrode groups are still imaged on one side of the piezo wafer, but this time the per-existing polarization is exploited to design the necessary circuitry to power the device. In particular, as sketched in Figure 21, connecting the two electrode groups in series re-establishes the inverted polarization required by design. As a side note, in the sketch, the piezo material under each electrode group is approximated by an RC electrical block because of the weak coupling between the transducer and the hosting medium. This shift leads to a solution electrically equivalent to the one presented above, but with the ease of not having to re-polarize the piezo wafer.

At this point, is worth noting that given the directionality distortions encountered during testing of the rectangular patch at frequencies above 200 kHz (see Section 2.4.3), the spiral FSAT chosen for the prototype features a reduced frequency bandwidth that goes from 50 kHz to 250 kHz, which is reduced by 100 kHz if compared to the device used in the FE

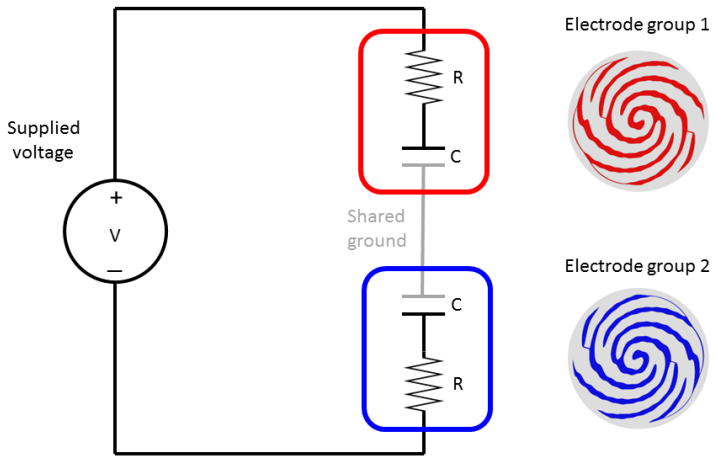

Figure 21: Electrical schematic of differential excitation of the spiral FSAT. Wiring is equivalent to a series connection, which practically re-establishes the proper "polarization" of the two electrode's groups.

simulations. The radius of the patch is set to $a = 28$ mm and the threshold level used is $\eta = 8.2\%$, which is sufficient to guarantee that the two electrode groups are well separated, so that the chance of a circuit short is remote.

For the fabrication, PZT 5A, instead of PZT 5H, is chosen based on considerations on the material Curie temperatures, which are directly involved in the fabrication procedures, where temperatures of 150° C are expected. The transducer electrode pair is thus realized by means of the Toner Transfer Method (TTM) [38], which is a patterning technique widely used for in-house manufacturing of Printed Circuit Boards (PCBs), and has been here successfully adapted to be able to transfer custom electrode layouts on piezo-ceramic disks.

In this process the trace layout of the electrode's pair is printed out on a piece of special toner transfer paper that allows the ink to come off when heat is applied. The toner transfer paper is then put print-side-down on a Nickel-plated pre-polarized piezoelectric disk, heated and pressed-on with a laminator. The heat and pressure from the laminator transfers the toner from the paper to the Nickel. The exposed Nickel surface is then chemically removed through an etching procedure, while the previously applied toner act as an etch resist, thus protecting the Nickel in the electrode's areas. The toner is finally removed using commercial

paint thinner. The entire procedure is outlined in Figure 22.

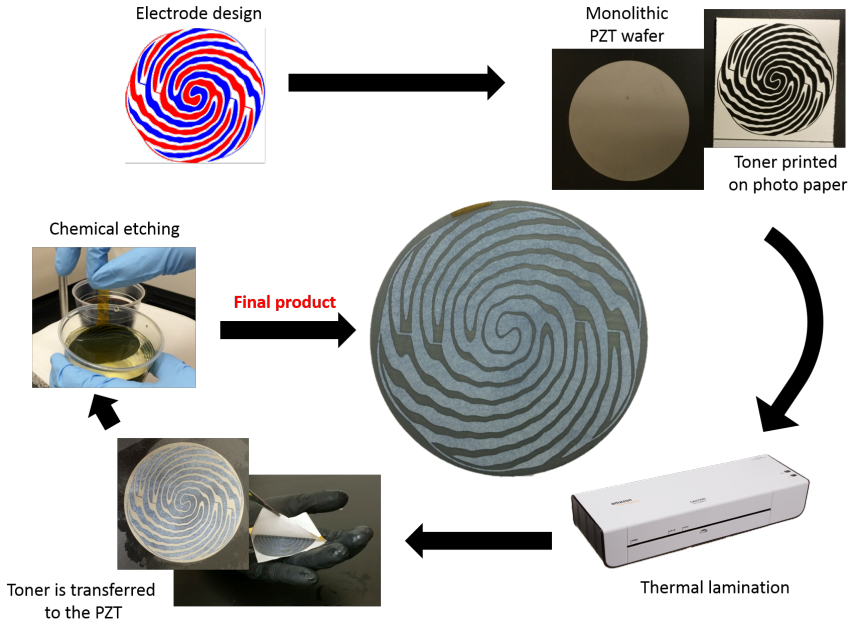

Figure 22: Toner transfer method steps for the fabrication of custom shaped electrodes out of a monolithic piezoelectric wafer.

It is worth noting that the TTM, although it allows dramatic savings when it comes to electrode manufacturing cost, has many critical steps. Firstly, both sides of the piezoelectric disk must be cleaned and rinsed properly before undergoing the thermal procedure of toner transfer. This can be done with a degreaser soap. Poor cleaning, and in particular grease residues on the Nickel plating will prevent a good toner transfer, so the use of proper gloves throughout the entire procedure is recommended. Secondly, a typical thickness of piezo wafers suitable for the FSAT manufacturing is of the order of few hundreds of μm. This, if combined with the extreme brittleness of the PZT material, makes the device fragile, so that particular care in handling the device is required. In addition, the toner removal is critical, since ultrasonic cleansers have a high probability of breaking the device, and it needs to be completed by hands.

TTM is here utilized to manufacture the spiral FSAT electrodes shape out of a circular wafer of 63.5 mm diameter and 190 μm thickness coated with 200 nm thick Nickel electrodes and polarized through-the-thickness (Piezo Systems, Inc.). The printer used to print the electrode mask is a HP Laserjet 1320n, and the paper used is HP Glossy Premium

Presentation Paper (120 g). The laminator used is the AmazonBasic Thermal Laminator set on 5 mil. Kapton film is used to secure the photographic paper to the piezo wafer, while 9 passages through the laminator provide a reliable transfer of the toner mask on the wafer electrodes down to feature sizes as small as 50 μm. Etching through Radioshack PCB etchant solution is performed in a controlled environment (low fumes hood). The wafer is immersed in the solution for a total time of 45 s followed by proper rinsing and drying. Finally, the toner mask is removed by gently stripping the toner off with Acetone. This fabrication process is fast and provides absolute flexibility in the shape that can be patterned. In addition, the mask-end-etch approach ensures optimal performance from an electrode standpoint, as it exploits the original coating provided by the vendor.

3.3.4 Testing

The resulting transducer, pictured in Figure 23(a), is then vacuum bonded with bi-component high strength epoxy (Loctite® Epoxy Adhesive, Hysol E-20HP) to a 0.81 mm thick aluminum plate, Figure 23(b). The vacuum bonding procedure guarantees that the epoxy layer underneath the device is as thin and uniform as possible.

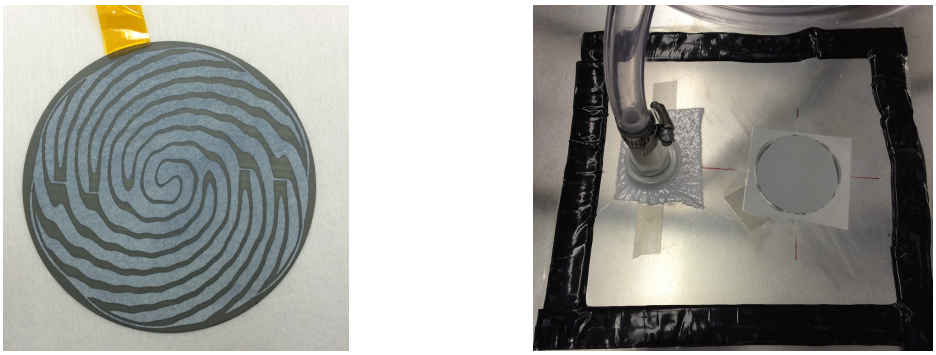

(a) (b)

Figure 23: (a) Spiral FSAT prototype manufactured onto a piezo wafer. (b) Vacuum bag used for the bonding procedure.

The frequencies selected to verify the directional performance of the device span its bandwidth, ranging from 50 kHz to 200 kHz with incremental steps of 50 kHz. The results are presented in Figure 24 in terms of time RMS of the out-of-plane velocity recorded with a Scanning Laser Doppler Vibrometer (SLDV) on a circular grid centered at the transducer

location, as sketched in Figure 12. The device shows consistent beam-forming capabilities, and the overall directionality performance is considered excellent, although directionality distortions are present for frequencies above 200 kHz, as expected. As previously stated, this is believed to be related to shear-lag phenomena due to the epoxy bonding layer used to attach the device to the structure, and non-linear PZT effects which have both been neglected at design stage.

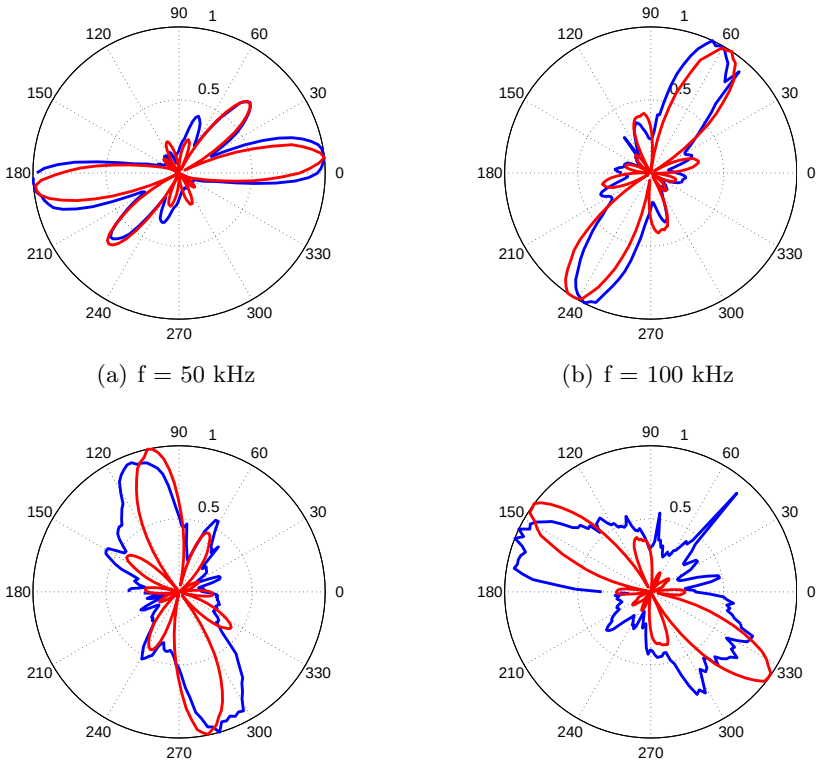

(a) f = 50 kHz (b) f = 100 kHz

(c) f = 150 kHz (d) f = 200 kHz

Figure 24: Actuation mode spiral piezo wafer-based FSAT experimental directionality at selected frequencies. Blue line: experimental. Red line: analytical.

3.4 Monolithic Designs on Piezo-ceramic Substrates for Anisotropic Composite Plates

Dispersion relations of Lamb waves in anisotropic composite plates are considered in the following section, and design refinements of the spiral FSAT design that enable the application to anisotropic media are discussed.

3.4.1 Isotropic VS. Anisotropic Media: an FSAT Perspective

Although the isotropy requirement is not strictly necessary for the frequency beam steering concept to be valid, a modification of the design framework needs to be performed when dealing with anisotropic plates such as composites. Iso-frequency lines are no longer represented by circles in the wavenumber domain, which needs to be accounted for in order to achieve continuous and smooth beam steering capabilities.

Specifically, the adoption of a spiraling distribution of material does not guaranteed that iso-frequency lines representing dispersion relations intercept a single directivity maximum for a given wavenumber. For example, Figure 25 shows intersection of a potential spiraling material distribution (represented by blue circles) with three iso-frequency lines for a unidirectional Glass laminate. The example clearly illustrate how increasing wavenumbers do not correspond to transducer sensitivity at increased angles of directionality. More in detail, for the angular sector highlighted in red, the directional performance of the device are severely compromised, and effective beam steering of GWs cannot be achieved.

The design of FSAT for isotropic media is based on the Archimedean spiral. From Equation (34), the location of directionality maxima in the wavenumber domain is given by

$$\boldsymbol{k}_n(\vartheta) = \frac{k_M - k_m}{\vartheta_M - \vartheta_m}\vartheta + k_m - \frac{k_M - k_m}{\vartheta_M - \vartheta_m}\vartheta_m \tag{37}$$

or simply

$$\boldsymbol{k}_n(\vartheta) = a_1\vartheta + a_0. \tag{38}$$

In order to cope with anisotropy issues the Archimedean expression is expanded by considering higher order terms that actively "guide" the spiral shape to better conform to non-isotropic dispersion relations.

3.4.2 Expansion on the Spiral Shape

An expansion on the spiral geometry in the wavenumber domain is adopted in the form of

$$\boldsymbol{k}(\vartheta) = \sum_{p=0}^{P} a_p \vartheta^p \tag{39}$$

where P represents the order of the expansion, the case for $P = 1$ corresponding to the original spiraling distribution in Equation (38). The spiral expansion of Equation (39) is

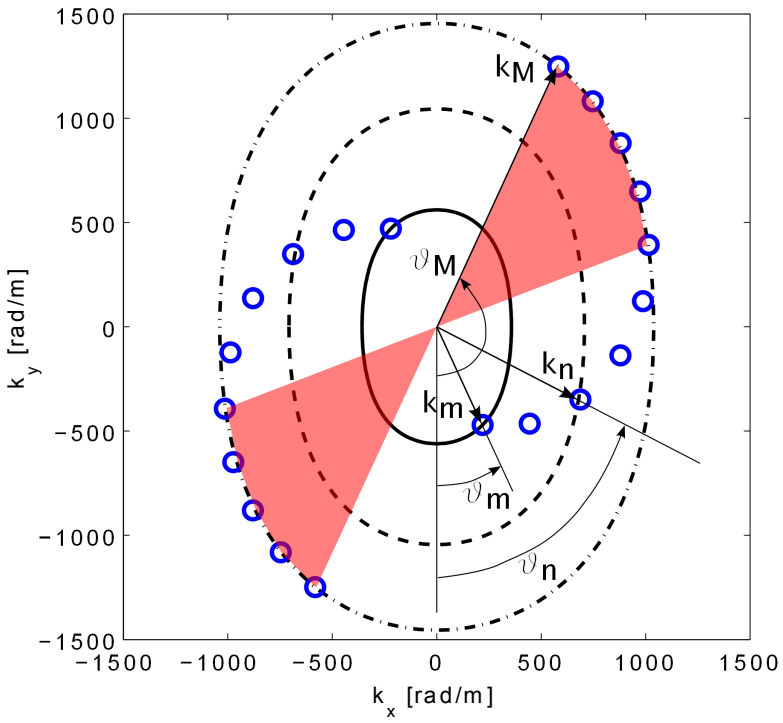

Figure 25: Schematic of spiral directivity in the wavenumber domain for the representative case of a unidirectional Glass laminate. Fibers are in the horizontal direction.

used to adapt the spiraling material distribution to the anisotropic dispersion through the series coefficients a_p, which are selected based on the interpolation of dispersion relations of the hosting medium.

As an example, consider a second order expansion of the spiral distribution ($P = 2$). In this case, expanding the terms under the summation sign in Equation (39), the radial wavenumber is expressed as

$$\boldsymbol{k}(\vartheta) = a_0 + a_1\vartheta + a_2\vartheta^2 \tag{40}$$

where the coefficients a_0, a_1, and a_2 represent the unknowns of the problem and are to be determined. In order to determine the three coefficients that will define the spiraling material distribution, the values of $k(\vartheta)$ are retrieved for three directions corresponding to three different iso-frequency curves that are equally spaced inside the design bandwidth of the device, Figure 26. As it can be seen, k_1, corresponds to k_m, and k_3 to k_M: this ensures that the interpolation spans the entire angular sector associated with the device.

In order to retrieve the the values for k_1, k_2, and k_3 to plug into the approximation

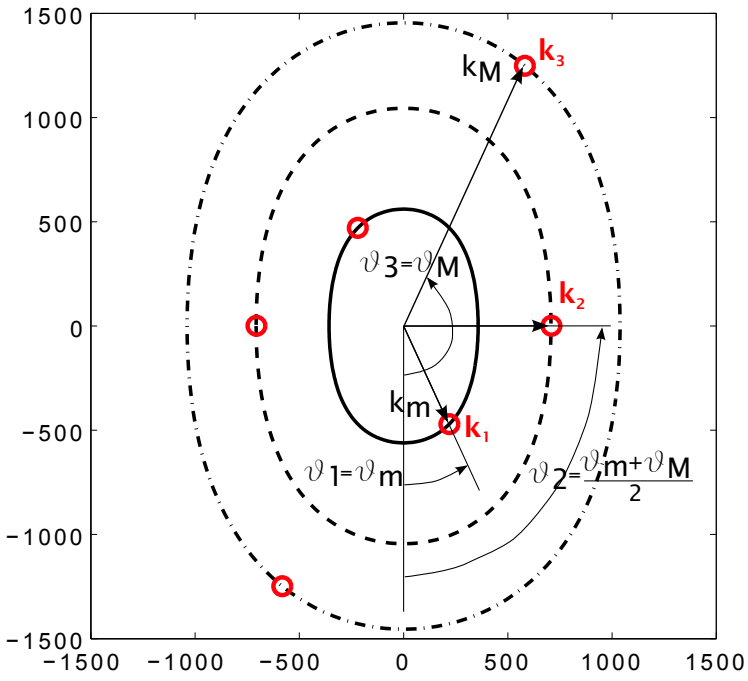

Figure 26: Wavenumber picking for the setup of a higher order spiral with $P = 2$. Dispersion relations are those associated to a unidirectional Glass laminate. Fibers are in the horizontal direction.

problem, dispersion relations associated with the specific composite laminate under consideration are calculated based on the Semi-Analytical Finite Elements (SAFE) analysis [6], can be implemented. Given the dispersion relations, the following system of equations is setup

$$\underbrace{\begin{bmatrix} 1 & \vartheta_{(1)} & \vartheta_{(1)}^2 \\ 1 & \vartheta_{(2)} & \vartheta_{(2)}^2 \\ 1 & \vartheta_{(3)} & \vartheta_{(3)}^2 \end{bmatrix}}_{\boldsymbol{A}} \underbrace{\begin{Bmatrix} a_1 \\ a_2 \\ a_3 \end{Bmatrix}}_{\boldsymbol{x}} = \underbrace{\begin{Bmatrix} k_1(\vartheta_{(1)}) \\ k_2(\vartheta_{(2)}) \\ k_3(\vartheta_{(3)}) \end{Bmatrix}}_{b} \tag{41}$$

and solved for the vector of the unknowns $\boldsymbol{x}$, which leads to the definition of the higher order spiral shape. The design procedure illustrated in Section 3.2 can now be applied.

3.4.3 Devices and Composite Plates Specifications

The design procedure outlined above is applied to two case studies: (i) a quasi-isotropic Glass laminate (GlassQI), and (ii) a unidirectional Glass laminate (GlassUD). Their geometrical and mechanical properties are reported in Table 2 and Table 3 respectively.

Table 2: Geometrical properties of the composite laminates.

Plate flag	Units		
GlassUD	Material		S2/CYCOM5216
	Lamination sequence		$[0°]_8$
GlassQI	Material		S2/CYCOM5216
	Lamination sequence		$[0°, 90°, 45°, -45°]_s$
	Dimensions	[mm]	600 x 600 x 1.684

Table 3: Mechanical properties of the composite laminae.

Parameter	Units	S2/CYCOM5216
ρ	[kg/m^3]	1980
E_1	[MPa]	47800
$E_2 = E_3$	[MPa]	13600
$\nu_{12} = \nu_{13}$	[ ]	0.257
ν_{23}	[ ]	0.3
$G_{12} = G_{13}$	[MPa]	5900
G_{23}	[MPa]	5200

The selected frequency bandwidth of the spiral FSATs ranges from 50 kHz to 250 kHz, with an associated beam steering azimuthal range that goes from $-90°$ to $+90°$. The dispersion relations associated to the targeted A_0 mode corresponding to the frequencies defining the devices bandwidth are reported in Figure 27 for both laminates.

The order of the spiral expansion, P in Equation (39),. is chosen in order to maximize the linearity of the directionality-frequency mapping associated with the device. This is believed to be of help in future implementations of the devices, where instead of a having a full map to relate directionality with frequency, the only information required would be a gain parameter.

A parametric study is then conducted in order to identify a representative value for P that would allow a linear mapping between directionality and frequency. For this reason, the study is conducted with the dispersion relations corresponding to the GlassUD laminate, for which the anisotropy level is more significant. For the study the value for N is varied from $P = 1$, which corresponds to the Archimedean spiral, to $P = 6$. The results of the study are shown both in terms of shape of spiraling material distribution, Figure 28(a), and

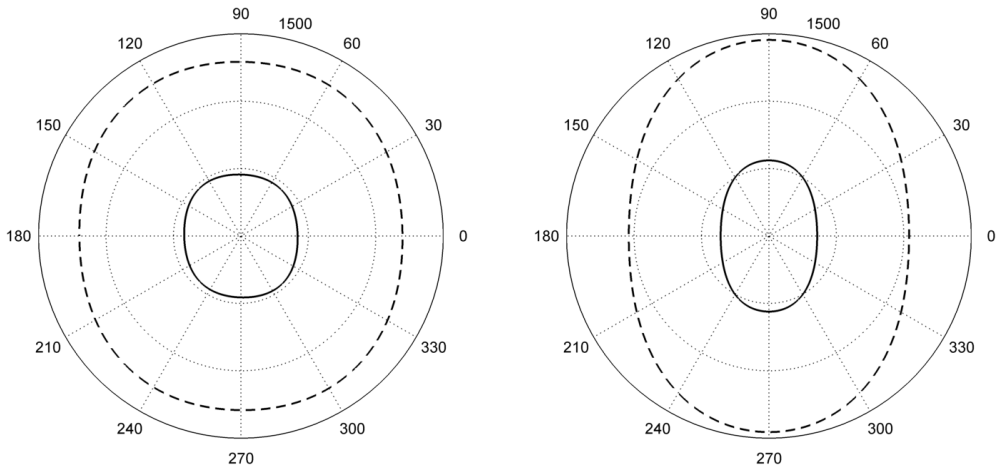

(a) GlassQI (b) GlassUD

Figure 27: Dispersion relations for the A_0 mode associated with the composite laminates under consideration. Solid black line: 50 kHz. Dashed black line: 250 kHz.

corresponding directionality-frequency map, Figure 28(b). As the spiral order increases, the trend in the directionality frequency map is to assume a linear relationship. For $P = 6$, the R^2 statistic of the linear regression performed on the map is $R^2 = 0.9988$, which is considered sufficient to guarantee an excellent linear correlation between directionality angle and frequency even in presence of strong anisotropy levels in the dispersion relations of the hosting medium. Thus, the order used for the expansion on the spiral design is $P = 6$.

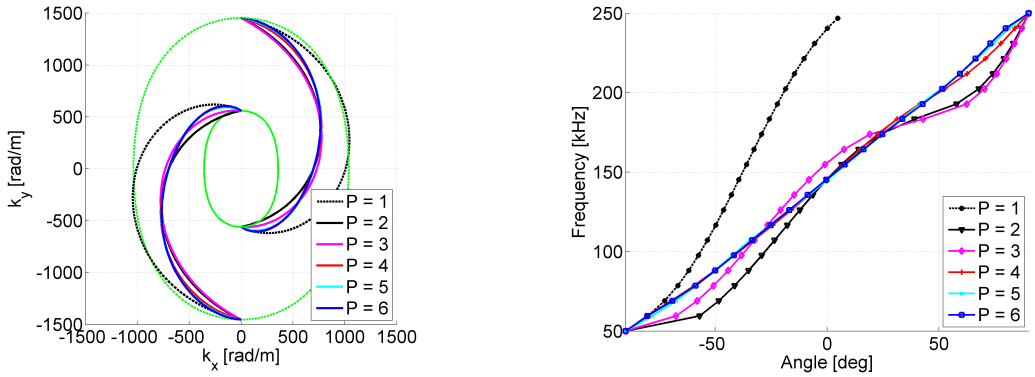

(a) (b)

Figure 28: (a) Spiraling arrangement of material for different spiral orders. Green lines: GlassUD laminate dispersion relationships: 50 kHz (solid), and 250 kHz (dashed). (b) Directionality-frequency maps for different spiral orders.

The resulting transducer shapes are reported in Figure 29 for the GlassQI laminate, and

Figure 30 for the GlassUD one. For both, spatial and wavenumber domain, showing the spiraling of the material, are reported.

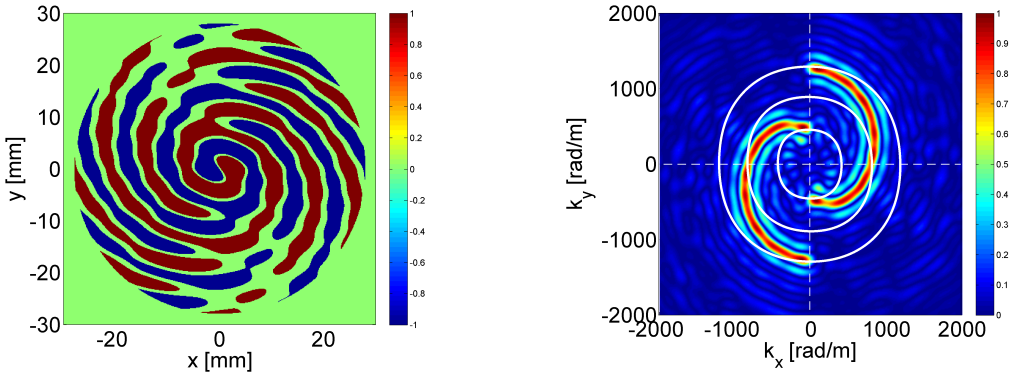

(a) Spatial Domain (threshold $\eta = 8.2\%$) (b) Wavenumber Domain

Figure 29: Sixth-order spiral FSAT design for the GlassQI laminate. Wavenumber domain represents the one associated with threshold transducers. White curves: dispersion relations of the hosting medium. Fibers are in the horizontal direction. Target wave mode: A_0.

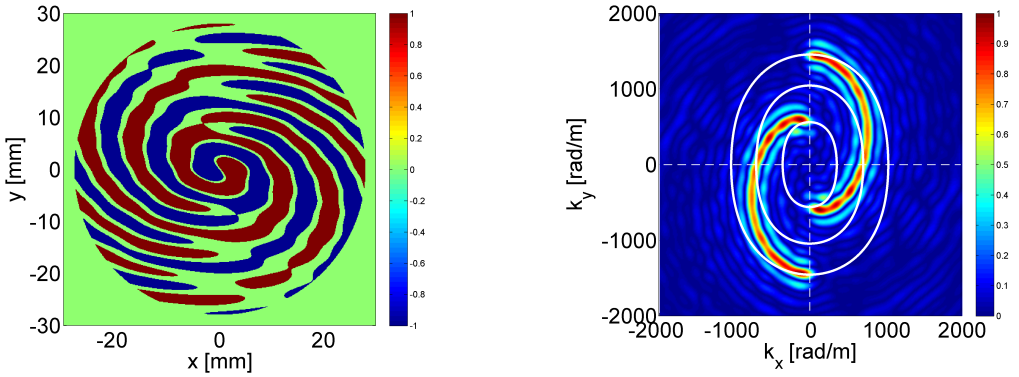

(a) Spatial Domain (threshold $\eta = 8.2\%$) (b) Wavenumber Domain

Figure 30: Sixth-order spiral FSAT design for the GlassUD laminate. Wavenumber domain represents the one associated with threshold transducers. White curves: dispersion relations of the hosting medium. Fibers are in the horizontal direction. Target wave mode: A_0.

3.4.4 Fabrication

The devices represented in Figure 29(a) and Figure 30(a) are fabricated on a monolithic piezo wafer using the TTM outlined in Section 3.3.3. Successively, they are bonded to the corresponding composite plate through vacuum bonding. This ensures uniformity both in thickness and distribution of the adhesive layer underneath the devices. Figure 31 shows

the devices bonded to the composites plates and ready for testing.

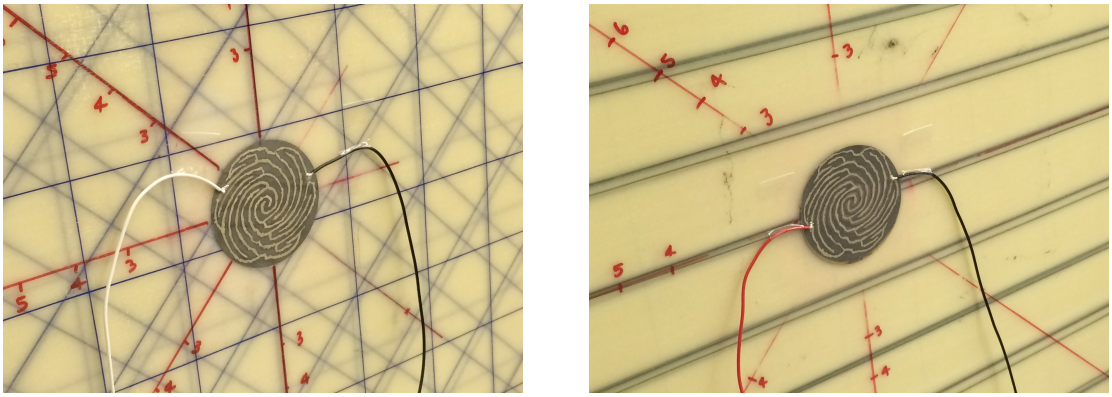

(a) GlassQI (b) GlassUD

Figure 31: Higher order spiral FSATs bonded to their corresponding composite plate and ready for testing.

3.4.5 Testing

Testing of the directional performance of the devices in actuation mode is performed following the same procedure used in Section 3.3.4, with the only difference being that here the azimuthal beam steering of the devices ranges from $-90°$ to $+90°$, instead of $0°$ to $180°$.

The frequencies selected to verify the directional performance of the device span its bandwidth, ranging from 50 kHz to 200 kHz with incremental steps of 50 kHz. For each frequency, time RMS of the out-of-plane velocity recorded with a SLDV on a circular grid centered at the transducer location is analyzed. The experimental setup is the same as the one sketched in Figure 12.

Results are reported in Figure 32 for the GlassQI plate, and Figure 33 for the GlassUD one. As it can be seen, both configurations achieve good directionality results when compared to analytical predictions. Also, if compared to the ones obtained for the case of aluminum, the results gathered for the composite laminates tend to present higher levels of noise. The reason of this is believed to be associated with the presence of a high level of material attenuation, which significantly contributes to damp out the amplitude of traveling waves, even for short traveling distances [12], thus reducing the signal-to-noise ratio of the acquired waveform time traces. Although material attenuation is acknowledged to play an

important role regarding wave propagation in composites, its effects are not studied as part of this work.

Despite the problems highlighted above, the results presented show an overall good agreement between analytical directionality prediction and the experimental performance of the devices, suggesting that the design framework can be consistently used for directional actuation of GWs even on composite laminates presenting strong anisotropy levels.

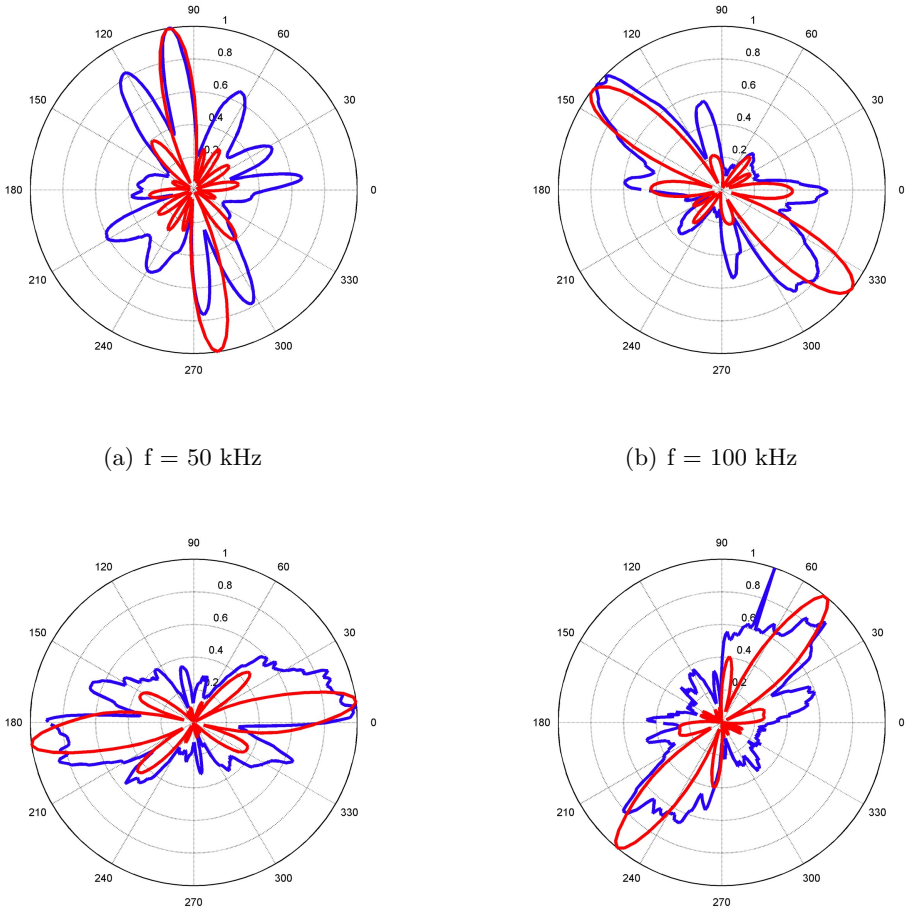

(a) f = 50 kHz

(b) f = 100 kHz

(c) f = 150 kHz

(d) f = 200 kHz

Figure 32: Actuation mode experimental directionality at selected frequencies for the sixth-order spiral FSAT on monolithic piezo wafer prototype for the GlassQI plate. Blue line: experimental. Red line: analytical.

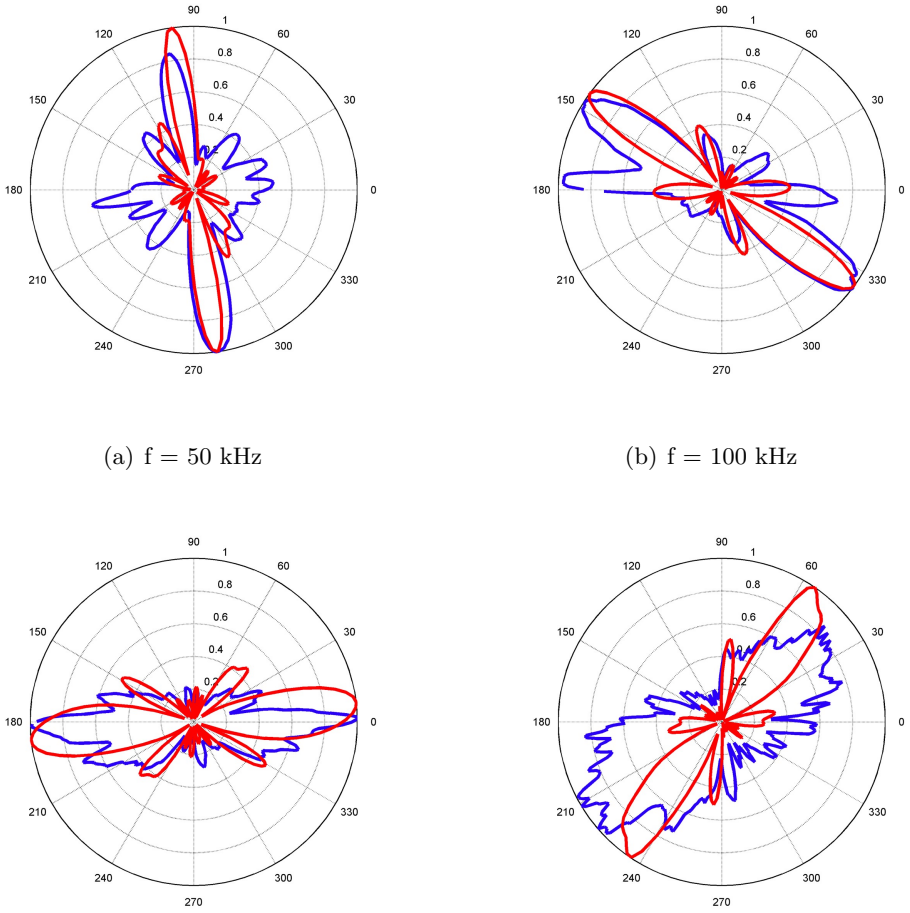

(a) f = 50 kHz

(b) f = 100 kHz

(c) f = 150 kHz

(d) f = 200 kHz

Figure 33: Actuation mode experimental directionality at selected frequencies for the sixth-order spiral FSAT on monolithic piezo wafer prototype for the GlassUD plate. Blue line: experimental. Red line: analytical.

3.5 Piezo-fibers Implementation of FSATs

The directional performance of the spiral FSAT manufactured on a monolithic PZT wafer were demonstrated in Section 3.3, and Section 3.4 for isotropic and anisotropic hosting media, respectively. That solution, although very convenient for laboratory testing and flat surfaces, is of limited applicability to curved scenarios due to the intrinsic brittleness of piezo wafers. In order to overcome such a limitation, a design featuring a flexible active layer is proposed. The new transducer aims to leverage the advanced design of the spiral FSAT frequency-based beam steering concept, and the durability, conformability, and robustness

associated with piezo fibers-based constructions [92].

3.5.1 Overview of Piezo-fibers Based Devices and Architectures

Typically, crystalline materials show much higher mechanical strength in fiber form, since the volume fraction of flaws is reduced. In addition, the polymeric matrix phase that embeds the fibers is flexible in nature, and thus confers flexibility to the material which may conform more easily to curved surfaces found in the majority of applications.

Recent years have seen an ever-increasing number of research-grade and commercially available devices containing piezo fibers. Piezoelectric fiber composites, called Active Fiber Composites (AFCs), were introduced by Hagood and Bent [32] as an alternative to monolithic piezo wafers for structural actuation applications. AFCs use cylindrically extruded piezoceramic fibers encasted between interdigitated electrodes and bonded using a structural epoxy. A similar concept to that of AFCs are the Macro Fiber Composites (MFCs) developed at the NASA-Langley Research Center [94]. The main difference with respect to AFCs is that the MFC fibers have a rectangular cross section, and thus can be directly diced from commercially available ceramic wafers. For this reason, MFCs provide a cheaper alternative for device prototyping on small scales if compared to AFCs, even though their square fibers arrangement have issues deriving from stress concentrations at the edges of the fibers causing potentially shortened life spans. Following the same conceptual idea, Salas and Cesnik [72, 69] developed a Composite Long-range Variable-direction Emitting Radar (CLoVER) transducer, which is a device consisting of a series of wedge-shaped sectors that are individually excited to provide directional interrogation or sensing of a structure while also providing full azimuthal coverage.

A typical piezo fibers transducer comprises an active layer, formed by uniaxially aligned fibers, surrounded by a polymeric matrix and sandwiched between two flexible thin encapsulating layers. The electrodes can be either continuous, in which case a voltage difference is applied between the top and bottom electrodes resulting in an electric field perpendicular to the plane of the transducer, Figure 34(a), or interdigitated [32], resulting in a curved electric field mostly aligned in the direction of the fibers, Figure 34(b). In the former case,

the piezoelectric fibers are driven in the d_{31} mode, for which the poling direction (conventionally denoted by 3) is normal to the plane of the patches, while in the latter the fibers are driven in the d_{33} mode, for which the poling direction can be consider that of the fibers, although the electric field lines do not have a constant direction [18].

The theory for directional sensing and generation of GWs with shaped piezo patches developed by Senesi [74] and refined herein assumes a through-the-thickness polarization of the active material, i.e. it assumes that the electric field is perpendicular to the transducer plane. A piezo fibers device operating in the d_{31} mode presents the same electrical configuration and it is therefore a sound substrate choice for the prototyping of conformable spiral FSATs.

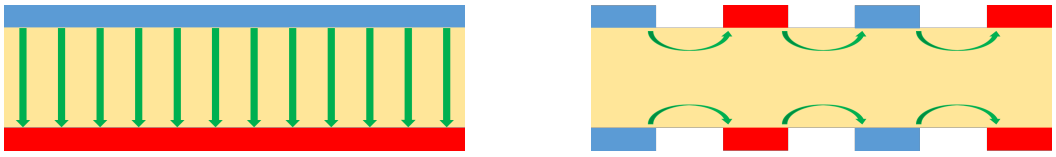

(a) d_{31} mode (b) d_{33} mode

Figure 34: Electric field distribution (green arrows) for different electrode configurations. Blue: negative electrode. Red: positive electrode.

3.5.2 Design

Due their composite nature piezo fibers-based devices exhibit anisotropic properties, both mechanical and piezoelectric, which is manifested in the material-related directivity $\mathcal{H}(\vartheta)$ defined by Equation (12) and reported herein for convenience

$$\mathcal{H}(\vartheta) = \frac{t_P}{A_P} \frac{\boldsymbol{b}^T \boldsymbol{d}^\sigma \boldsymbol{C}^E \boldsymbol{r}(\vartheta)}{\left[\boldsymbol{b}^T (\boldsymbol{d}^\sigma \boldsymbol{C}^E \boldsymbol{d}^{\sigma^T} - \boldsymbol{\varepsilon}^\sigma) \boldsymbol{b}\right]}. \tag{42}$$

As it can be seen from Equation (42), the value of $\mathcal{H}(\vartheta)$ is no longer constant with respect to the angular coordinate ϑ.

Considering the values listed by Deraemaeker in [19], and reported in Table 4 for convenience, for the properties of MFC operating in d_{31} mode, the angular variation of $\mathcal{H}(\vartheta)$ is showed in Figure 36(a). The horizontal direction is assumed aligned with the fibers, Figure 35. The transverse-to-the-fibers direction has a value that is approximately half of that in the direction aligned along the fibers, which means that the voltage level generated

by a wave packet traveling with an incidence angle of 90° direction is about half of that of a wave incident at 0°.

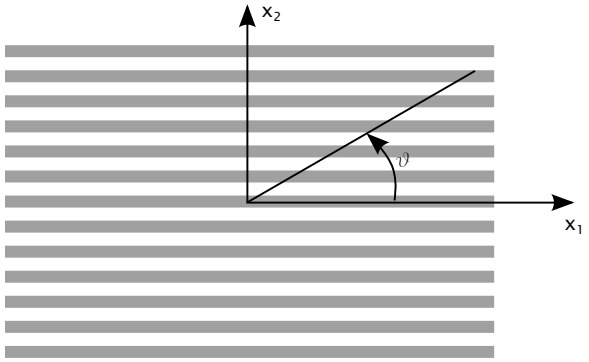

Figure 35: Fibers orientation with respect to the wave propagation direction ϑ.

An important parameter in determining this material-related anisotropy is the fibers-to-volume fraction (i.e. ρ) of the active layer assembly, which enters Equation (42) through the piezoelectric matrix C^E. Its influence is reported in Figure 36(b), where it can be seen that the anisotropy level decreases when the fibers-to-volume ratio approaches the value of $\rho = 1$. Also, as expected, for $\rho = 1$, i.e. for the case of a monolithic active layer, the function $\mathcal{H}(\vartheta)$ becomes isotropic.

Table 4: Typical MFC material properties with a fiber-to-volume fraction ($\rho = 0.865$). Fibers are assumed to be aligned with the 11 direction.

Quantity	Value	Unit of Measure
c_{11}	31	GPa
c_{22}	16	GPa
ν_{12}	0.31	[ ]
d_{31}	−182	pC/N
d_{32}	−173	pC/N

The extension of the FSAT concept that takes advantage of piezo-fibrous arrangements requires material anisotropy compensation.

Looking at the expression for the voltage of Equation (11), the idea is to use the function $\mathcal{H}(\vartheta)$ to derive an azimuthal compensating factor to juxtapose to the geometrical directionality term $\mathcal{D}(\boldsymbol{k}(\omega), \vartheta)$. To this aim, a compensation function is introduced in the expression of the voltage to remove the effect of the material anisotropy associated to the active layer

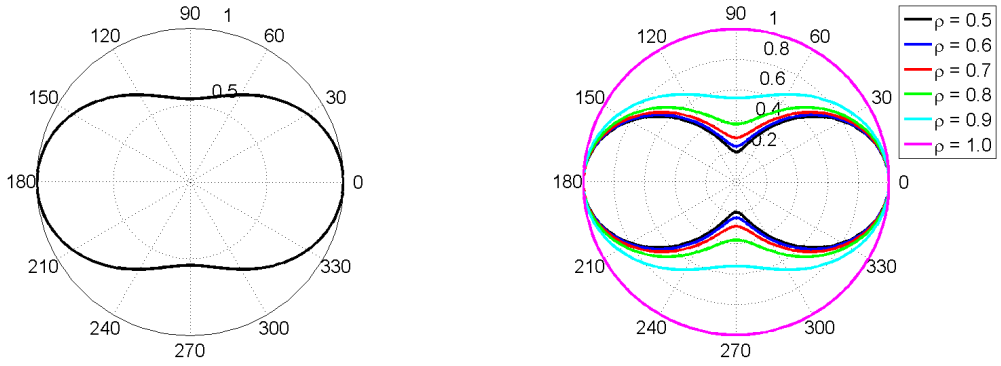

(a) $\rho = 0.865$ (b) ρ variable

Figure 36: (a) Material directionality function $\mathcal{H}(\vartheta)$ for a typical d_{31} type MFC material. (b) Influence of the fibers-to-volume fraction on the anisotropy level of the substrate. Fibers are in the horizontal direction.

properties. Specifically, this is done to make the product $\mathcal{H}(\vartheta) \cdot \mathcal{D}(\boldsymbol{k}(\vartheta), \omega)$ a constant, maximum, value, regardless of the direction of wave propagation. The simplest way to conceive such a compensation function is to consider the use of a multiplier for the voltage. Conceptually, this idea assumes the following form

$$\mathcal{C}(\vartheta) = \frac{1}{\mathcal{H}(\vartheta)}. \tag{43}$$

From a practical standpoint, the multiplier of Equation (43) is introduced as a modulation parameter for the radial extension of the transducer (a_n), which is now ϑ-dependent.

One effective way to achieve this, is to introduce the radial modulation at a design stage, with a procedure that takes place in the wavenumber domain. The compensated directivity function in the wavenumber domain is given by the following expression

$$\mathcal{D}(\boldsymbol{k}_0(\omega),\, \vartheta) = -j \frac{1}{N} \sum_{n=1}^{N} a_n^2 \left[\frac{J_1(a_n|\boldsymbol{k}_0 - \boldsymbol{k}_n|)}{a_n|\boldsymbol{k}_0 - \boldsymbol{k}_n|} - \frac{J_1(a_n|\boldsymbol{k}_0 + \boldsymbol{k}_n|)}{a_n|\boldsymbol{k}_0 + \boldsymbol{k}_n|} \right] \tag{44}$$

where $a_n = a\bar{\mathcal{C}}(\vartheta_n)$ represents the modulated radial extension of the transducer, and $\bar{\mathcal{C}}(\vartheta_n) = \frac{\mathcal{C}(\vartheta_n)}{max(\mathcal{C}(\vartheta_n))}$ represents the normalized modulation factor. This operation result in an "apodized" spatial shape, which compensate, in terms of spatial extension, for the active layer anisotropy introduced by the piezo-fibers configuration. The term *apodized* is borrowed from optics, where *apodization* is the technical term for changing the shape of a

mathematical function. Indeed, in optics design jargon, an apodization function is used to purposely change the input intensity profile of an optical system.

As it can be seen from Equation (44), the compensation directly acts on the wavenumber representation of the transducer, modulating the peaks that define the spiraling of the material both in terms of (i) amplitude, and (ii) width. This can be seen in the schematic of Figure 37, where the peaks along the spiraling of the material are defined by blue circles, amplitude modulation is represented by a thicker line associated with the circle, and width modulation is outlined by a different radial dimension of the circle.

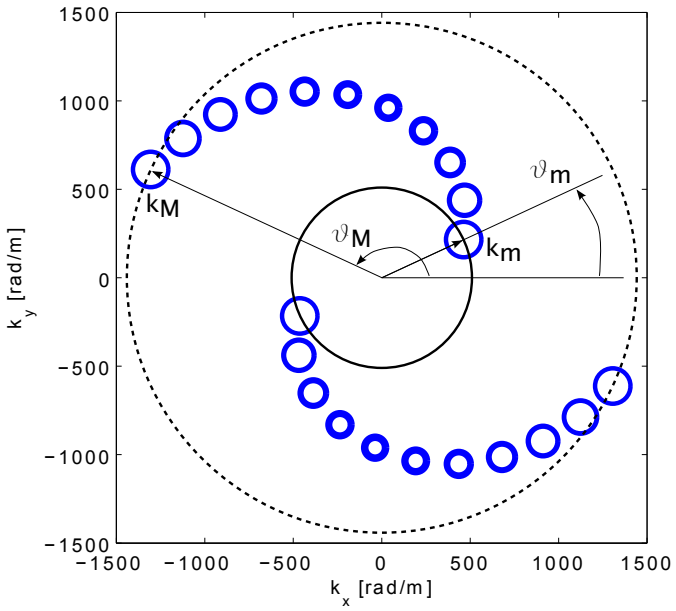

Figure 37: Schematic of compensated spiral directivity in the wavenumber domain for the case of an aluminum plate. Piezo-fibers of the active layer are in the horizontal direction.

It is worth noting that peaks amplitude modulation is of little help in achieving anisotropy compensation, given the fact that a threshold procedure is later applied to the spatial shape of the transducer in order to allow manufacturing. The reason why it is included resides in the fact that it makes the mathematical formulation of the compensation problem mathematically more elegant by enabling the existence of exact FT pairs between spatial and wavenumber domain. Conversely, peaks amplitude width plays a key role in achieving anisotropy compensation, since it directly acts on the radial extension of the device. More

in detail this enables the achievement of a higher actuation authority in the transverse-to-the-fibers direction by allowing a larger device footprint, indicated by a smaller circle radius in Figure 37, that makes up for its weaker piezoelectric coupling due to the prevalence of the matrix material.

Thanks to existence of an exact FT pair, the analytical expression for the spatial distribution of the piezoelectric material given by Equation (44) can be obtained analytically through an IFT, Equation (16). This operation results in the following expression

$$f(\boldsymbol{x}) = \frac{1}{N} \sum_{n=1}^{N} \text{rect}\left(\frac{|\boldsymbol{x}|}{a_n}\right) \sin(\boldsymbol{k}_n \cdot \boldsymbol{x}) \tag{45}$$

where a_n is the ϑ-dependent radius of the device, and $\boldsymbol{k}_n$ denotes the wave vector corresponding to the angle ϑ_n, at which the nth maximum of the transducer is located in the wavenumber domain.

This procedure is adopted to design an apodized spiral FSAT on a 0.81 mm thick aluminum plate. The transducer features a frequency bandwidth that ranges from 50 kHz to 350 kHz while spanning an angular sector that goes from 0° to 180°. For this configuration, the device spatial and wavenumber domains are represented in Figure 38. As it can be seen, the transducer shape is more compact in the direction aligned with the fibers, i.e. where the piezoelectric coupling is stronger, while it features a wider footprint in the transverse direction, i.e. where piezoelectric coupling is weakened by the presence of the matrix of the piezo-fibers configuration. For this configuration, the directionality-frequency map is the same as the one represented in Figure 17 for the non-apodized device. The reason behind this resides in the fact that the compensation does not act on the geometrical shape of the spiraling of the material, and this allows the use of the Archimedean version of the spiral of Equation (34).

For the transducer reported in Figure 38, it can be easily verified that the compensation effect introduced allows to maintain a constant product between $\mathcal{H}(\vartheta)$ and $\mathcal{D}(\boldsymbol{k}(\omega), \vartheta)$, across the entire frequency bandwidth, regardless of relative alignment between actuation direction and fibers orientation. This means that in a hypothetical actuation scenario, provided that the power fed to the device is constant over the whole frequency bandwidth,

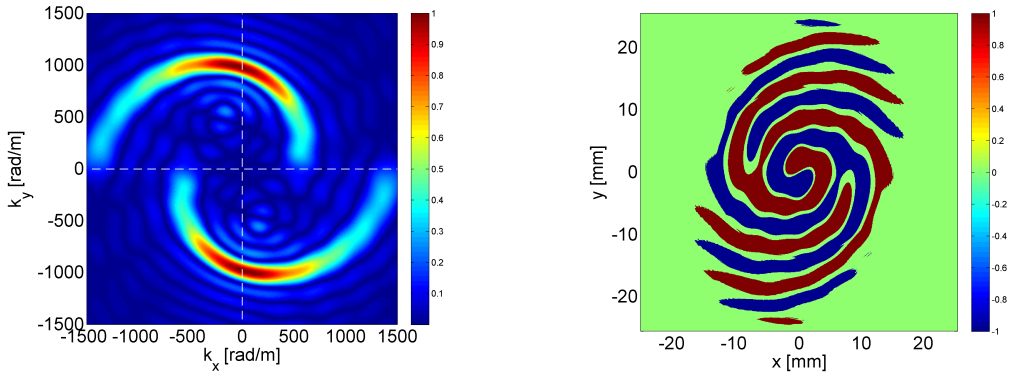

(a) (b)

Figure 38: (a) Spiraling of material distribution in the wavenumber domain compensated for active layer anisotropy. (b) Corresponding spatial shape of the apodized transducer after threshold procedure ($\eta = 8.2\%$). Radial extension of the actuator is varied by modulating the spiral peak width and amplitude. Fibers direction is aligned with the x-axis.

the actuation authority is constant for the whole angular sector covered by the device. Figure 39 reports three examples of this situation for three different frequencies, highlighting the beneficial effects of the compensated design over the non-compensated one in presence of anisotropic active layers.

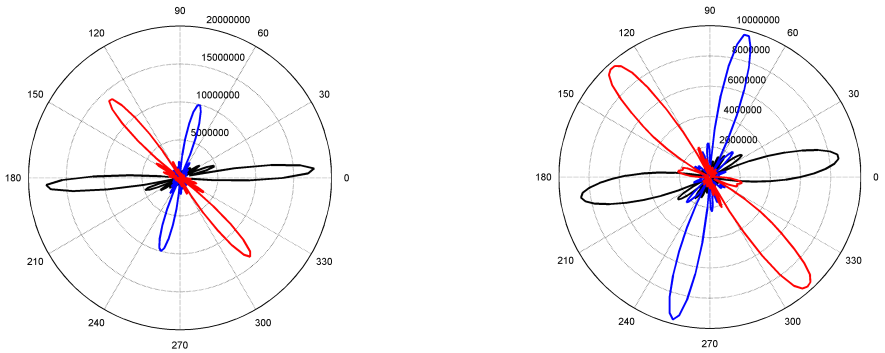

(a) Traditional design authority (b) Apodized design authority

Figure 39: Analytical actuation authority voltage levels in presence of a piezo fibers active layer. Solid black line: 50 kHz. Solid blue line: 150 kHz. Solid red line: 250 kHz. (a) Non-compensated original design. (b) Compensated design. Radial amplitudes are arbitrary.

3.5.3 Numerical Analysis of Directional Performance

The performance of the apodized version of the device reported in the previous section, is tested numerically through FE procedures. As performed for the monolithic piezo-wafer design in Section 3.3.2, a coupled piezo-elastic FE model is built using COMSOL Multiphysics®. The hosting medium consists of a 0.81 mm thick aluminum plate, with the apodized spiral FSAT bonded on one side. The FE model is in all similar to the one reported in Figure 18, the only exception being the electrodes shape, that are now designed according to the compensated design procedure described above. The thickness of the piezo-fibrous active layer is set to 0.19 mm, and the MFC-like d_{31} operational mode is considered, for which the averaged piezo-mechanical properties reported by Deraemaeker [19] are used.

The excitation is provided through an electrical boundary condition with a 200 V 4-cycles Hanning-windowed TB applied between the spiral electrodes and the commonly shared ground (which is coincident with the plate top surface). Two different burst center frequencies, 50 kHz and 150 kHz are considered, so that the transducer frequency-dependent directionality performance can be highlighted.

The FE discretization of the elastic plate and transducer is performed by means of COMSOL auto-meshing sequence set on physics-controlled mesh with a maximum element size set to 11 mm. The total number of degrees of freedom for the problem under consideration is 1433271. The FE discretization is then coupled with a transient solution procedure that yields the required piezo-elasto-dynamic response. For each analysis, the total simulation time corresponds to five times the duration of the TB used for excitation. Each FE analysis run takes approximately 4 h and 18 GB of RAM on a 12 cores workstation with 64 GB of RAM. The results of the simulations are presented in Figure 40 in terms of out-of-plane displacement at selected time instants.

Results in terms of full-field time slices at selected time instants are presented in Figure 40, where it can be seen that the directional performance is consistent with qualitative analytical predictions. A quantitative assessment of the performance is then reported in Figure 41. In there, the time RMS of the out-of-plane displacement interpolated on a circular grid of 100 mm radius centered at the transducer location is compared to analytical

predictions. In particular, the directionality performance from an analytical standpoint is retrieved by direct interpolation of the material spiraling in the wavenumber domain along iso-frequency circles corresponding to the TB center frequencies.

In light of the results presented, it can be stated that frequency dependent directional performance of the apodized spiral FSAT is confirmed by numerical evidence, and the agreement with analytical predictions is very good.

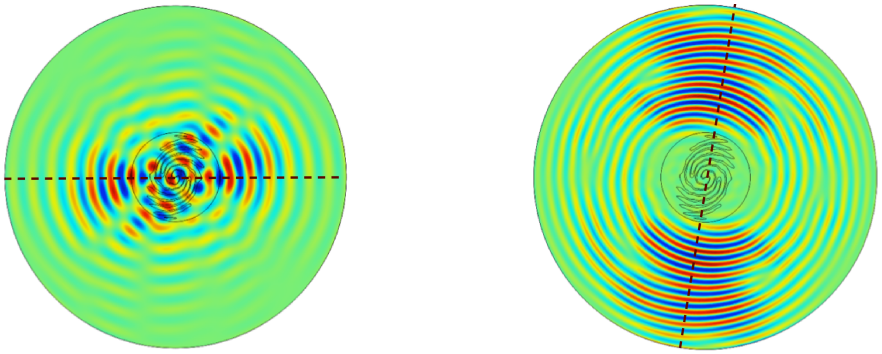

(a) f = 50 kHz (b) f = 150 kHz

Figure 40: Apodized spiral FSAT time snaps deriving from FE analyses. Clear wave beaming is visible. Dark red dashed line: expected directionality.

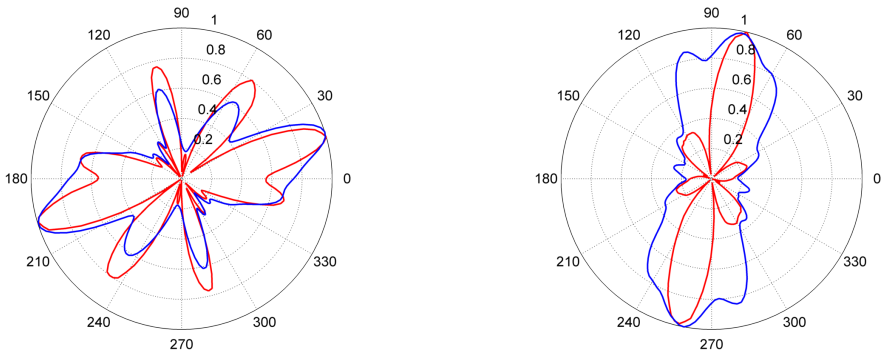

(a) f = 50 kHz (b) f = 150 kHz

Figure 41: Piezo-elastic FE model results in terms of out-of-plane plate displacement RMS at selected frequencies. Blue line: numerical directionality. Red line: analytical directionality.

3.5.4 Fabrication

Typically, a piezocomposite transducer comprises of an active layer sandwiched between two thin Copper-Kapton films to compensates for the brittleness of the PZT fibers. The fibers,

which embedded in a polymeric matrix, feature a rectangular cross-section and are machined from piezoceramic wafers using a computer controlled dicing saw [96]. The packaging brings the electric field to the active layer through the use of a specific surface electrode pattern. Given the piezoelectric operational mode, the fabrication approach consists in utilizing the apodized spiral FSAT shape as the top electrodes' geometry, while the back side metalization provides the common ground electrical connection, as sketched in Figure 42. Assembly and manufacturing, performed by Professor Cesnik's group at the University of Michigan at Ann Arbor, closely follow the procedures developed for the CLoVER transducer reported in [72] which are now summarized.

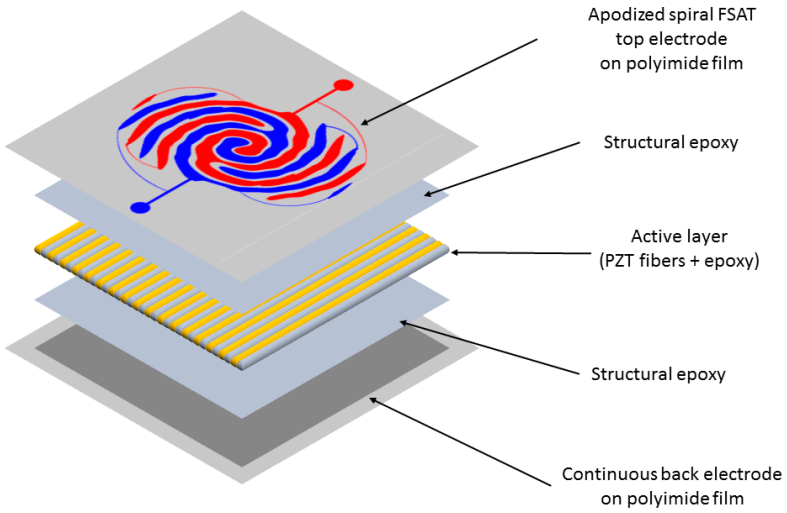

Figure 42: Exploded view of all the constituting layers of the apodized spiral FSAT assembly.

The manufacturing procedure is itself an adaptation of the process presented by Wilkie [95, 39] for MFC actuators. A high-level overview of the manufacturing technique is outlined in Figure 43. Once the CAD drawing is extracted from MATLAB following the design procedure outlined above, the electrode pattern is printed on a copper-clad kapton film (Pyralux® LF7062R) using photolithography (Metro-Circuits Inc).

PZT-5H monolithic piezoceramic wafers with 0.19 mm thickness (EBL Products) are diced into wedge-shaped fibers (American Dicing), with the single fiber width set to 0.36 mm.

This value corresponds to the width of prismatic piezoceramic fibers used in typical APT devices [93]. The fibers and electrodes are then bonded using an epoxy adhesive (Hysol Loctite E-120HP).

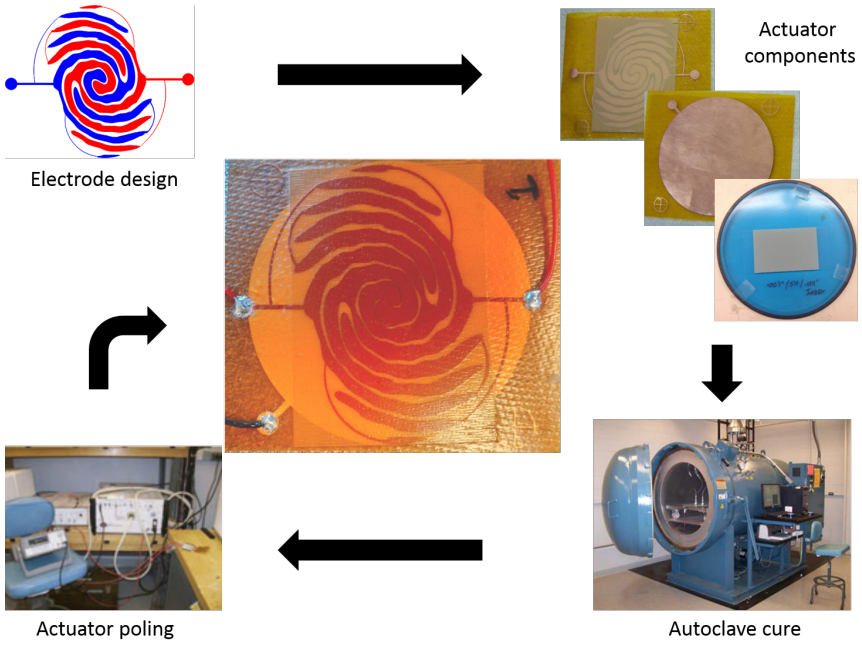

Figure 43: Apodized spiral FSAT transducer development stages.

The transducers are subsequently cured in an autoclave facility, and the standard manufacturing procedure employs a vacuum hot press. Each actuator is cured for 2 h in a vacuum (28.2 in Hg) bag at 100 psi (689.5 kPa) and 250°F (121°C). This cure time and temperature have been previously shown to be sufficient for full actuator cure based on experimentally-calibrated cure kinetics models [95].

The required set of poling parameters would result in transducers with performance levels, and piezo-elastic properties, similar to those of NASA-standard MFCs. Unfortunately, due to a high burning rate of the transducers during poling procedures, the poling voltage is reduced to about 80% of the one required. Although this represents a non-negligible deterioration of the device actuation authority, it is judged sufficient in order to demonstrate the directional performance of the apodized FSAT. In addition to this, the device wide frequency bandwidth (50 kHz - 350 kHz) introduces an additional performance deterioration factor. Recalling the results of Section 3.3.4 directionality distortion is expected for

frequencies above 200 kHz (i.e. for steering angles above 120° in this case). Further details of the manufacturing and characterization procedures for CLoVER devices can be found in separate works by Salas [70, 71].

3.5.5 Testing

The final cured and poled product is vacuum bonded with bi-component high strength epoxy (Loctite® Epoxy Adhesive, Hysol E-20HP) to a 0.81 mm thick aluminum plate. The vacuum bonding procedure is the same as the one adopted for the monolithic piezo wafer bonding previously performed.

The frequencies selected to verify the directionality performance of the device in actuation range from 50 kHz to 200 kHz. The results are presented in Figure 44 in terms of time RMS of the out-of-plane velocity recorded with an SLDV on a circular grid centered at the transducer location. The experimental setup is the same as the one sketched in Figure 12.

The device shows consistent beam-forming capabilities, and the overall directionality performance is good agreement with the analytical prediction. One thing that can be noticed, Figure 44(a), is that the directionality performance for the frequency of 50 kHz is poor, even from an analytical standpoint. This is due to the compensation procedure, which probably penalizes too much the spiraling distribution for the 0° direction, as seen in Figure 38(a).

Also, as it can be seen from Figure 44(b) through (d), a slight mis-alignment between the analytically predicted directionality and the experimental one is visible, even at lower frequencies. This is believed to be due to the fact that the actual piezo-elastic properties of the manufactured piezo-fibers assembly are known only with a certain degree of approximation.

3.6 Conclusions

In this chapter, the concept of frequency-based beam steering has been introduced through the presentation of the spiral FSAT concept in actuation mode. The design procedure, which takes place in the wavenumber domain, is exploited and adapted to allow device operations on (i) isotropic and anisotropic hosting media in presence of a monolithic piezo wafer-based arrangement, and (ii) isotropic hosting media in presence of piezo-fibrous arrangements

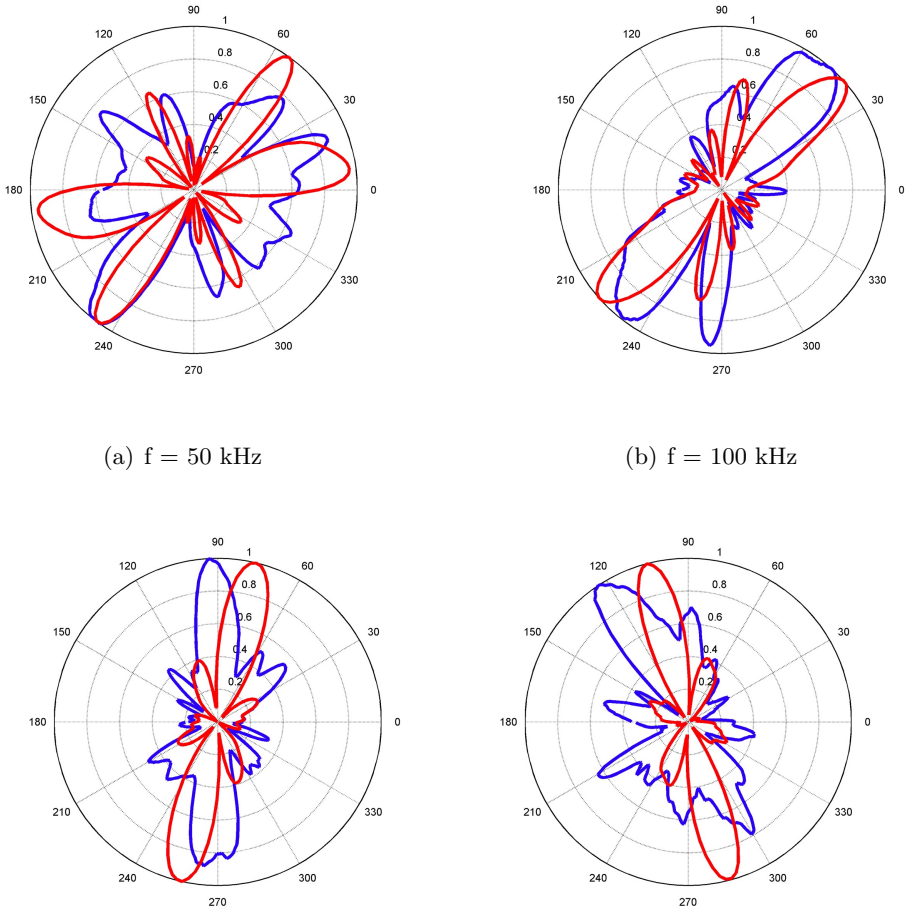

(a) f = 50 kHz

(b) f = 100 kHz

(c) f = 150 kHz

(d) f = 200 kHz

Figure 44: Actuation mode apodized spiral FSAT experimental directionality at selected frequencies. Blue line: experimental directionality. Red line: analytical directionality. Fibers are in the horizontal direction.

of the active layer. Numerical and experimental validations of the devices, along with fabrication procedures that enable device prototyping, have been presented in support of the efforts performed towards the design of the transducers.

The next chapter presents the application of monolithic piezo wafer-based devices in a damage detection scenario. The approach adopts the usage of pulse-echo testing procedures coupled with damage imaging techniques. The results will show consistent retrieval of both radial and azimuthal location of simulated damages while using a single spiral FSAT device.

CHAPTER IV

SPIRAL FREQUENCY STEERABLE ACOUSTIC TRANSDUCERS FOR PULSE-ECHO DAMAGE DETECTION

4.1 Overview

This chapter presents the efforts conducted to assess the performance of spiral FSATs as damage detection devices. In particular, the discussion is focused on assessing their damage localization performance when operated individually in pulse-echo mode. Firstly, the state of the art regarding pulse-echo operations in presence of propagating Lamb waves is analyzed, and benefits of such a technique are outlined. Then, damage detection performance of the monolithic piezo wafers spiral FSATs is tested on aluminum and composites. For both cases, damage sites are simulated by means of a stack of magnets, and device performance with single as well as multiple damage scenarios is discussed. The analysis also includes the presentation of ad hoc imagining techniques tailored to the FSATs design characteristics that allow a visual estimation of the location of damages.

4.2 GWs for Non Destructive Testing and SHM

Guided acoustic waves, such as Lamb waves, have many applications in non-destructive testing (NDT). One important application area of such waves is for long-range testing, since GWs are capable of rapidly interrogating large areas of plate-like structures [90]. In combination with GWs, ultrasonic methods have been considered to monitor the integrity of critical structural components because they are one of the few, if not only, techniques that can interrogate large areas while maintaining sensitivity to damage [57]. The potential of using Lamb waves for non-destructive testing (NDT) has been pursued since their existence was proved experimentally at ultrasonic frequencies [28, 47]. Since then, it has been demonstrated that GWs may be used effectively in NDT applications, given their sensitivity to cracks [83], corrosion [81], and delamination [45].

Whereas traditional NDT methods obtain large area coverage by scanning, it is desirable that SHM approaches can achieve large area coverage using a limited number of fixed sensors [47]. Within this scenario, distributed sparse arrays of inexpensive, piezoelectric transducers have been proposed as a cost-effective alternative to traditional bulk-wave C-scans for plate-like structures [67]. In array configurations, signals between multiple transducer pairs are monitored with the goal of detecting and locating damage based upon changes over time [57].

GW sparse arrays detection is made challenging by the large number of reflections from geometric scattering, and by the multimodal and dispersive nature or GWs. To cope with this, suitable GWs imaging techniques have been widely investigated [33]. In this context, GW imaging can be defined as the process of creating visual representations of a portion of a structural component providing indications on the presence of damage. A comprehensive review of such techniques is detailed in [33].

4.3 Lamb Wave Pulse-echo Operations with FSAT Devices

Common ultrasonics approaches to detect damage in plate-like structures, such as the one described in [29], that employ permanently attached piezo transducers fired in "pulse-echo" mode are now detailed for applications that take advantage of the spiral FSAT operation mode. In conventional NDT, the pulse-echo method has been traditionally used for through-the-thickness testing exploiting bulk-waves, Figure 45. In detail, the pulse-echo mode is an ultrasound diagnostic technique in which short-duration ultrasound pulses are transmitted into the region to be studied, and echo signals resulting from scattering and reflection are detected and displayed. The same transducer performs both the sending and the receiving of the pulsed waves, thus the name: pulse-echo.

The main drawback of this modality of operation is that, for large areas, it requires manual or mechanical moving of the transducer over the area of interest, which is labor-intensive and time-consuming. For this reasons, GWs-based pulse-echo operations appear to be more appropriate for SHM operation, since wide area coverage can be achieved from a single location, thus reducing the hardware requirements to a minimum. The employment

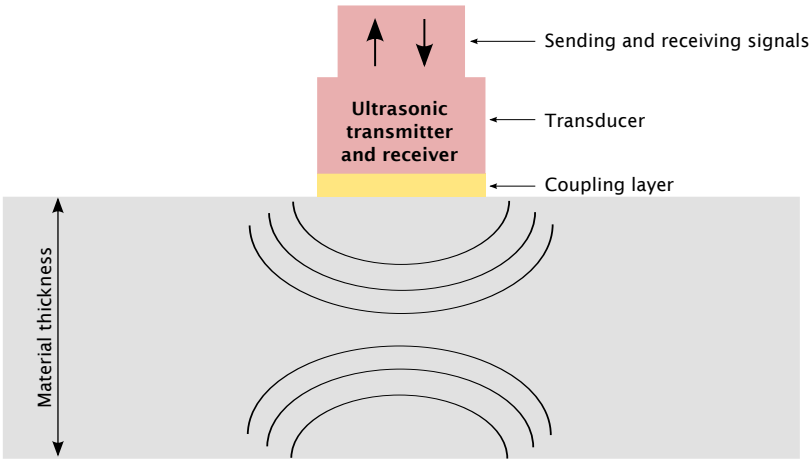

Figure 45: Through-the-thickness schematic of the pulse-echo method for ultrasonic testing.

of spiral FSATs in pulse-echo mode follows the general principles of conventional techniques developed for the NDT industry. The device, which is bonded to the structure, acts both as a transmitter and a receiver. The wave packet generated by the transducer in actuation mode is partially reflected by boundaries and damages, and the echo is captured by the same device acting in sensing mode.

For damage detection with the pulse-echo mode, high frequency (> 500 kHz) S_0 Lamb mode is typically employed, since (i) the wavelength is sufficiently smaller than typical damage sizes, and (ii) it leads to stronger reflections than A_0 mode from through-the-thickness damages [26]. This latter effect can be attributed to the fact that S_0 provides (i) a higher damage reflection coefficient which, in turn, provides a stronger signal for feature extraction, and (ii) much less dispersion which ensures compactness and ease of interpretation of the signal. In the case of the FSAT prototypes presented in the previous chapter the above-mentioned requirements of high frequency ranges and low mode dispersion are not fulfilled, since the devices targeted the more dispersive A_0 mode in a frequency range that spanned from 50 kHz to 250 kHz.

First, from a frequency standpoint, the wavelength associated to A_0 is much smaller than the one associated to S_0 as depicted in Figure 46. This ensures that the device is sensitive to damages that are down to few mm in size without the need to move to higher frequencies, where FSAT design complications would arise by the appearance of higher

order modes (A_1, S_1, etc.). In addition, from a dispersion standpoint, there exist a number of techniques that can be effectively used to compensate for dispersion [91, 16] without deteriorating the damage localization performance.

Experimental results in literature show that the pulse-echo method combined with piezoelectric transducers can be used to effectively locate damage in various engineering materials and structures [100] through imaging algorithms [57, 33]. Among the others, the use of elliptical (or hyperbola) imaging algorithms [33] is believed to be particularly suited for FSAT devices. These methods use the relationship between back-propagated signals to construct an image of the interrogation area, where the location of damage sites appear as high energy spots. They typically operate on differenced signals, i.e. baseline signals from the damage-free condition are subtracted from current ones.

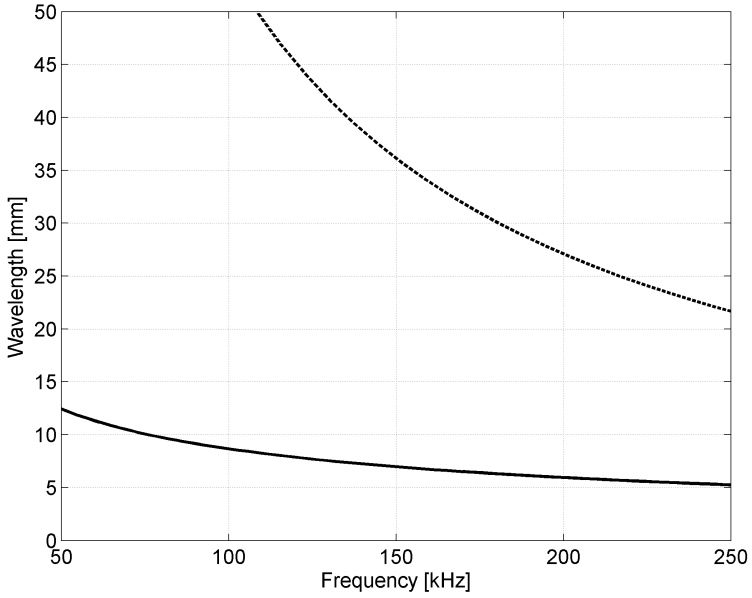

Figure 46: Wavelength comparison between A_0 (solid) and S_0 (dashed) Lamb modes for the frequency bandwith associated with the prototyped FSAT.

FSAT pulse-echo operations can be summarized through the schematic presented in Figure 47: in active mode, the device generates Lamb waves through a broadband pulse that excites the frequency bandwidth of the device, Figure 47(a). The wave packet travels within the plate and is scattered by damage sites (red circle), Figure 47(b). Finally, the

damage-reflected wave travels back to the device, which now operates in sensing mode. The damage echo is recorded by the same FSAT device, which now operates passively.

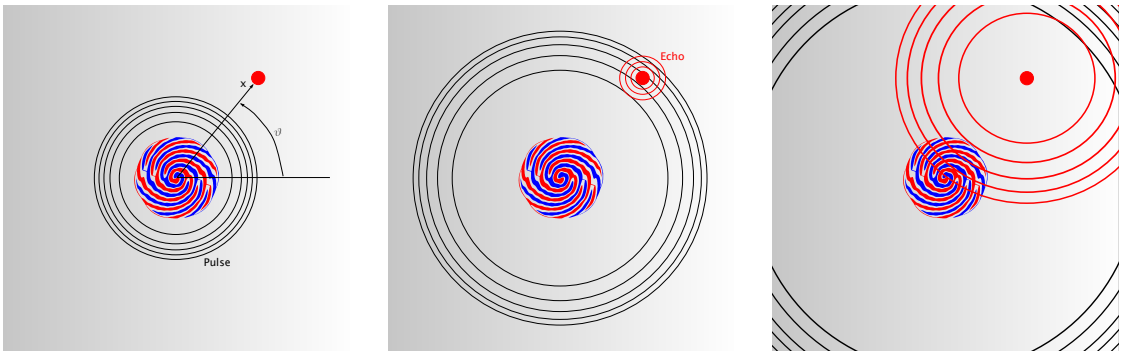

(a) (b) (c)

Figure 47: Schematic of the pulse-echo operations envisioned for the spiral FSAT.

The frequency dependent directional properties of the spiral FSAT enable imaging of 2D areas by employing the differential signal recorded from the device, so that only waves reflected off the damages can be highlighted. The information on the azimuthal location of the damage is associated with the spectral features of the acquired waveform, according to the directionality-frequency mapping of the device. The Direction of Arrival (DOA) that determines the damage azimuthal location is defined by a peak in the signal spectrum centered around the frequency corresponding to the direction of the wave reflected from the damage. This relies on the assumption that the FSAT in actuation mode provides a sufficiently uniform excitation throughout the whole azimuthal span, so that the filtering properties of the device in sensing mode are not biased. The information on the radial location of the damage is then evaluated through the estimation of the Time Of Flight (TOF), which is the time that takes the wave from when it is fired by the spiral FSAT, to when the echo of the damage-reflected wave gets picked up by the device, Figure 47(c).

Generally speaking, the retrieval of the radial location of the damage is complicated by the fact that an infinite number of GW modes exist and are dispersive. Within this scenario, transducer design can be used to target a specific mode, but it cannot overcome the effect of dispersion, since this phenomenon occurs to the wave as it propagates in the structure. In practical terms, dispersion causes the energy of a signal to spread out in space and time as it

propagates. This phenomenon worsen the resolution and makes experimental data hard to interpret. A graphical illustration can be found for example in [89]. Complications in signal interpretation due to dispersion can be minimized through the analysis and implementation of a dispersion compensation procedure, as explained in [25, 16, 90]. The case of the spiral FSAT damage detection performance on aluminum is now discussed.

4.4 Damage Detection in Aluminum

Given the promising results obtained in actuation mode on the spiral FSATs attached to the aluminum plate tested in Section 3.3 the employment of such devices is now tested to verify their damage detection capabilities through pulse-echo operations. The experimental setup consists of a 0.81 mm thick aluminum plate with the monolithic spiral FSAT bonded to one of its sides, as pictured in Figure 48(a). Damages are simulated through the use of magnets which provide a fast and non-invasive way to induce scattering of the incident wave. Stacks of 5 magnets (1 on the back of the plate, and 4 on the front) are used. Each magnet is a cylinder of 6 mm diameter and 6 mm thickness, Figure 48(b).

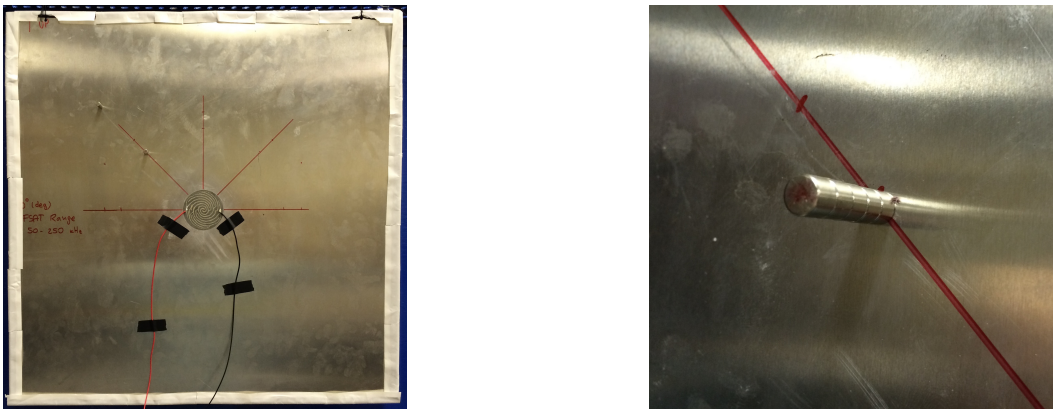

(a) (b)

Figure 48: (a) Experimental setup for the FSAT tests in pulse-echo mode. The differential channel setup is clearly visible. (b) Stack of 5 magnets used to simulate acoustic events. The single magnet has both diameter and height of 6 mm.

The FSAT is operated in differential mode, i.e. as described in Figure 21. The signal input consists of a broadband impulse that covers the entire bandwidth of the device, which is provided to the device by a pulser/receiver (Olympus 5058PR HV Pulser/Receiver). The

same instrument also provides all the required circuitry to automatically switch to sensing mode, allowing to retrieve the structural response (echo) recorded by the FSAT. The time-trace reading is finally performed by feeding the FSAT signal to an oscilloscope (Tektronix TDS2024), from which the data are recorded and analyzed through MATLAB.

4.4.1 Baseline Subtraction Procedure

First, the baseline response of the plate is recorded, $u_{REF}(t)$. Figure 49(a) shows the time trace as recorded by the device for the pristine plate condition, i.e. with no simulated damages. Later, a simulated damage is added to the plate in the location described above. For this case, the response recorded by the device, $u_D(t)$ is reported in Figure 49(b). As it can be seen, a new wave packet (circled in red) appears in the time trace recorded by the device, showing the presence of a reflection that was not present in the pristine plate condition, and thus cannot be attributed to boundaries. The new wave packet can be regarded as the "signature" of the damage as seen from the spiral FSAT.

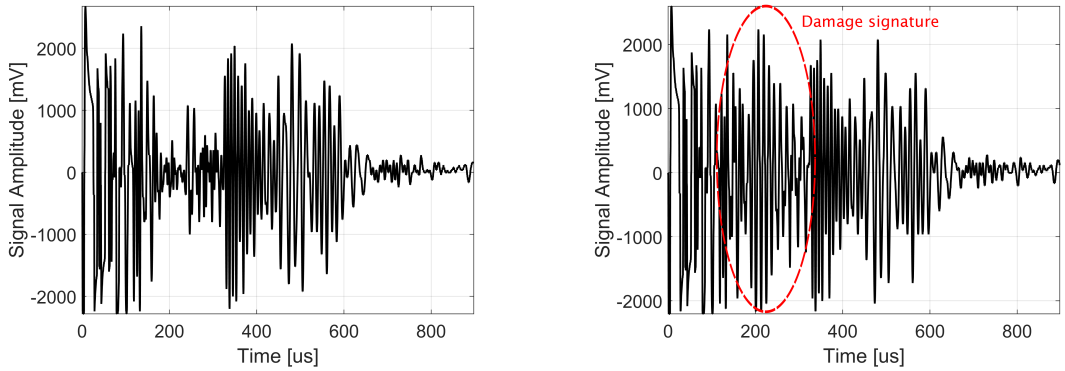

Figure 49: (a) Baseline signal $u_{REF}(t)$ recorded by the spiral FSAT. (b) Signal $u_D(t)$ recorded by the spiral FSAT with a damage located at 6 in from the device center, with an angular position of 45°.

In order to better highlight the damage signature, baseline subtraction is performed. The new time trace under investigation, $g(t)$, can be expressed as

$$g(t) = u_D(t) - u_{REF}(t). \tag{46}$$

In practice, $g(t)$ contains the information regarding the 2D location of the defects. The

resulting signal is reported in Figure 50.

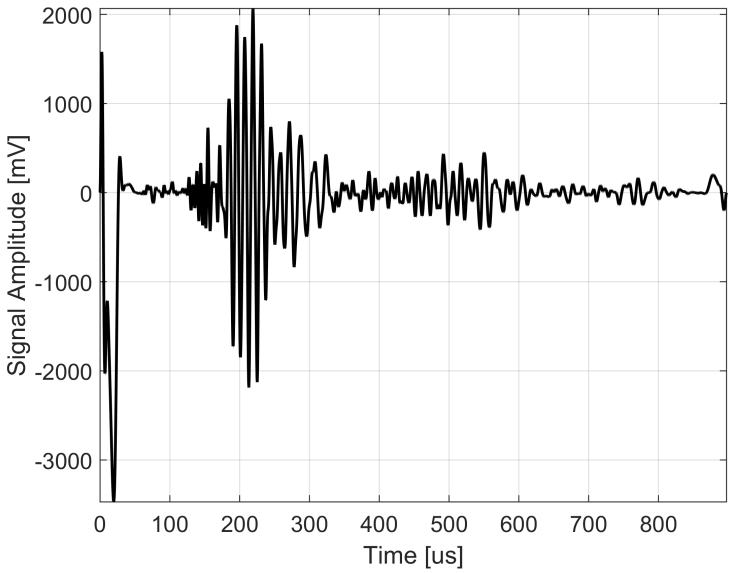

Figure 50: Signal $g(t)$ computed by subtracting the baseline signal to the one recorded with the simulated damage on the structure. The damage signature is evident.

Without dispersion, $g(t)$ can be mapped to a function of propagation distance, x, by the simple relationship

$$x = c_{gr}t \tag{47}$$

where c_{gr} represents the group velocity of the GW mode under consideration, A_0 in this case. This mapping is clearly trivial and can readily be achieved by scaling the time axis of $g(t)$ to propagation distance.

Things get significantly more complicated when dispersion comes into picture, because c_{gr} is now frequency-dependent, and Equation (47) cannot be used anymore. Dispersion compensation replaces the simple mapping of Equation 47 by one that is performed in the frequency-wavenumber domain. This enables frequency-dependent velocity (which can be considered as a definition of dispersion) to be taken into account. To perform this mapping it is necessary to know upfront the medium dispersion relations over the full bandwidth of the input signal. Details of the adopted compensation procedure can be found in [90], and are reported here for sake of completion.

4.4.2 Dispersion Compensation

Consider the case of the monolithic spiral FSAT mounted the aluminum plate that operates in pulse-echo mode. The out-of-plane surface displacement is used to represent the GW mode of interest, i.e. A_0. This is denoted by $u(x,t)$ where t represents time and x the propagation distance measured from the device location. The FSAT is supplied with an input signal $f(t)$. Furthermore, the following assumptions are made: (i) the FSAT is considered an ideal transducer, i.e. it excites only the GW mode of interest, and (ii) at the location of the FSAT $u(x,t) = f(t)$, and (iii) the actuation pulse has a time duration that never overlaps with echoes from damages, which are supposed to be located in the medium to long range.

Given $u(x,t)$ at one point in space, and knowing the propagation characteristics of the GW mode means that u can be evaluated at any point in time after any propagation distance by considering the phase-shift of each frequency component separately

$$u(x,t) = \int_{-\infty}^{+\infty} F(\omega) e^{j(k(\omega)x - \omega t)} d\omega \tag{48}$$

where $k(\omega)$ is the wavenumber associated with the GW mode as a function of the frequency, ω, and $F(\omega)$ is the FT of $f(t)$.

In a long-range inspection system, FSAT is operated in pulse-echo mode. After being excited with the input signal $f(t)$ the transducer is switched to sensing mode to detect reflections of GWs from features in the structure. Moreover, the baseline subtraction method outlined in Section 4.4.1 is performed, so that the time trace considered for dispersion compensation is $g(t)$.

The goal is to convert $g(t)$ to a function of propagation distance rather than time, and to compress the dispersed signal in $g(t)$. To this aim, the forward, or backward, propagation of the signal in $g(t)$, which has already propagated an unknown distance, can be simulated through Equation (48) if a new propagation distance, x', is defined with its spatial origin at the position where the received time trace was recorded. If a complete distance-time map were to be computed, then the forward-propagating signal would continue diverging in space and time, while the back-propagating signal would converge, as shown in Figure 51.

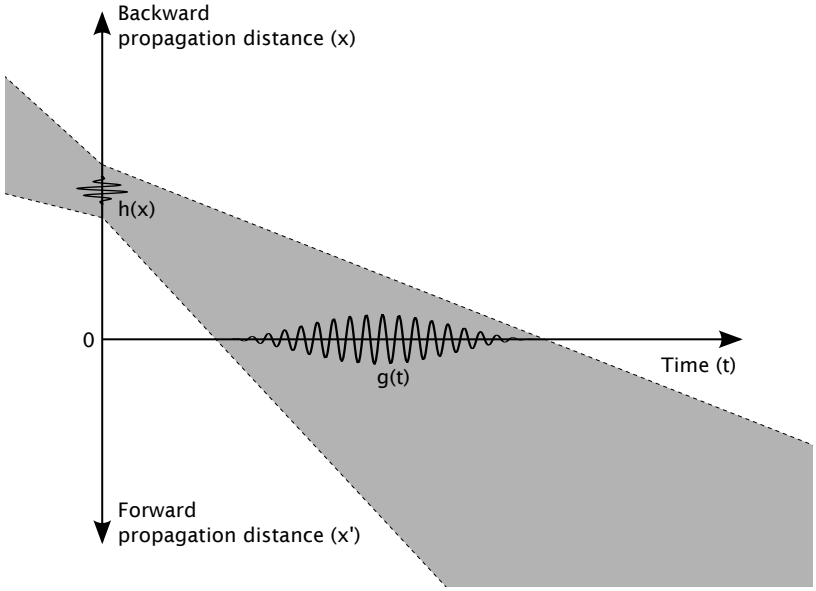

Figure 51: Distance-time diagram showing how the forward and backward propagation of $g(t)$ can be simulated.

Specifically, in the back-propagating direction the signal reaches a minimum as it passes through the $t = 0$ line, i.e. the distance line, and then it diverges again. The calculation of the back-propagated signal for negative values of x' at $t = 0$ gives precisely the desired mapping from time to propagation distance that compensates for the dispersion of the received signals. For clarity, a new distance variable, $x = -x'$ is defined, so that the back-propagation can be written as

$$h(x) = u(-x', 0) = \int_{-\infty}^{+\infty} G(\omega) e^{-jk(\omega)x} d\omega \tag{49}$$

where $G(\omega)$ is the FT of the time-trace $g(t)$, and $h(x)$ is referred to as the dispersion compensated distance-trace, which can be regarded as an alternative to using Equation (47) to convert the original time-domain signal, $g(t)$, to propagation distance, x.

Dispersion compensation is thus tackled in order to transform $g(t)$, which is a function of time, in $h(x)$, which is a function of space. This provides information regarding the radial location of the damage. To this aim, the spatial trace $h(x)$ is reported in Figure 52, where it can be seen that the damage signature is concentrated at a spatial distance around 304.8 mm (red dashed line), which corresponds to two times the actual distance of the damage site on the plate. This is expected, since the wave travels the distance between the

actuator two times: the first time when actuated by the spiral FSAT, and the second when reflected back by the damage. For this reason, the distance x will be divided by a factor of 2 when computing the spectrogram, in order to highlight the actual radial distance of the damage from the transducer.

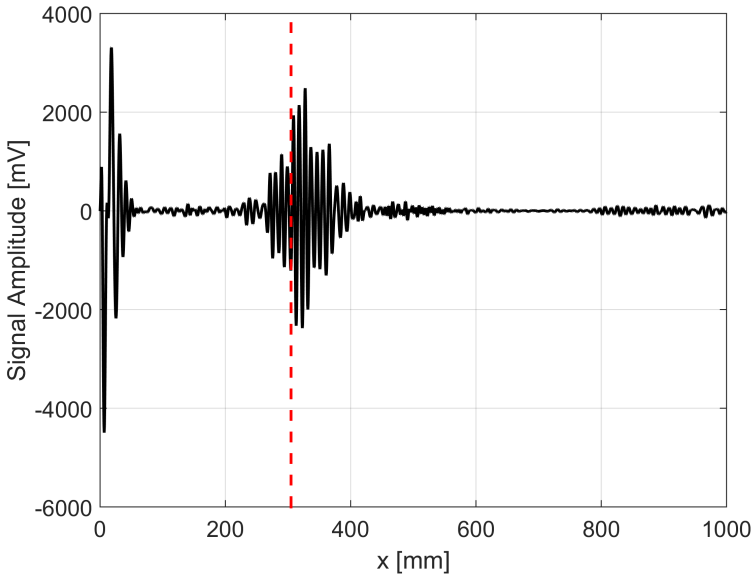

Figure 52: Signal $h(x)$ computed by compensating for dispersion the time trace $g(t)$. Red dashed line: radial location of the damage site.

Although the dispersion compensation algorithm presented above provides the desired signal compression and distance information that allow to estimate the radial location of the damage, it does not provide any insight regarding the damage azimuthal location. In order to retrieve that information, the filtering properties associated with the spiral FSAT design are used. Figure 53 shows the signal $H(k)$ computed by applying a FT to $h(x)$. As it can be seen, the wavenumber spectrum $H(k)$ filters quite sharply around the wavenumber associated to the 45° direction (represented by a red dashed line), which corresponds to the direction associated with the damage.

4.4.3 Short Time Fourier Transform for Imaging

From the results presented in Figure 53 and Figure 52 it is clear how both radial and azimuthal location of the damage can be retrieved. An effective way to get retrieve both information simultaneously can be achieved through the computation of the spectrogram

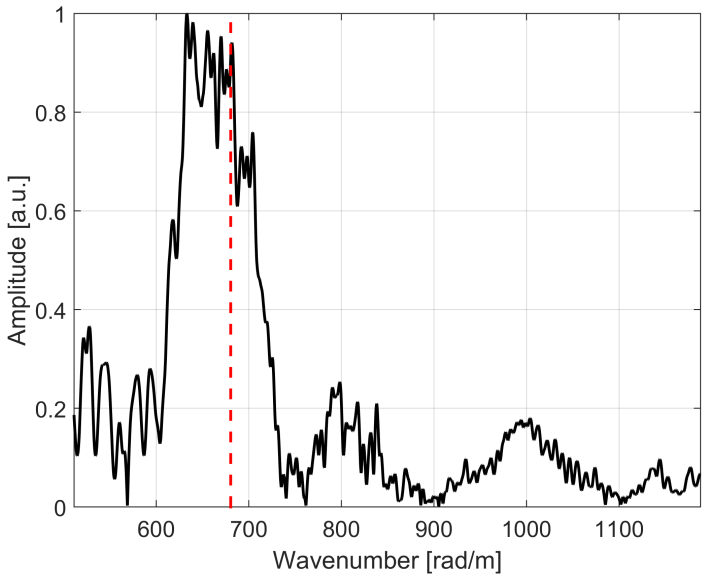

Figure 53: Signal $H(k)$ computed by applying a FT procedure to $h(x)$. Red dashed line: wavenumber corresponding to the 45° direction.

of the signal $h(x)$. More in detail, a common way of representing the spectrogram of a spatial trace consists of a graph with two geometric dimensions: the horizontal axis which represents space, and the vertical axis which represents wavenumbers. A third dimension indicating the amplitude of a particular wavenumber (angle) at a particular space (radial location) is represented by the intensity or color of each point in the image.

Within this scenario, acoustic events due to wave reflection from damages appear as localized high energy spots in the spectrogram, where range and angular information are provided. This operations allow the generation of an image that contains visual information regarding the presence and position of eventual damages, thus providing an effective way to localize them.

The spectrogram of $h(x)$ can be estimated by computing the squared magnitude of the Short Time Fourier Transform (STFT) as follows

$$\text{spectrogram}(x,k) = |\text{STFT}(x,k)|^2 . \tag{50}$$

Moreover, exploiting the spiral FSAT directionality map, wavenumber information can be

replaced by angular locations

$$\text{spectrogram}(x, k) \rightarrow \text{spectrogram}(x, \vartheta). \tag{51}$$

Figure 54 represents the spectrogram representation of $h(x)$, which is computed through the STFT algorithm. As it can be seen, the wavenumber axis has been replaced by the angle information. The damage is highlighted by a high energy spot that represents the estimated location of the damage. The prediction is in excellent agreement with the actual location of the damage (white circle), with an error that is below 20 mm.

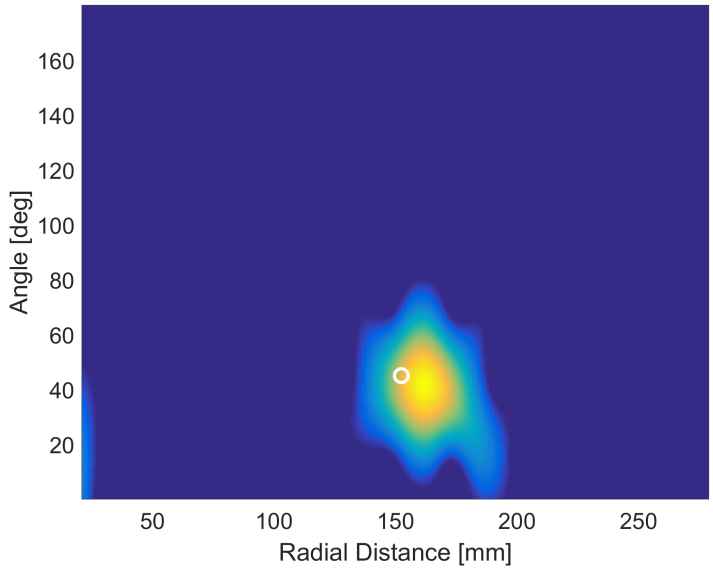

Figure 54: Spectrogram of the signal $h(x)$ with the wavenumber axis replaced by the corresponding angle. White circle: actual location of the damage.

The representation of the spectrogram of Figure 54 can be finally re-mapped to physical coordinates by noting that angle and radial distance are, in fact, the polar coordinates associated with the map. Figure 55 shows the the spectrogram remapped in Cartesian coordinates, where indications on actual location *and size* of the damage are also provided (red circle).

In summary, the STFT of the acquired signal, combined with the dispersion compensation algorithm, provides an ideal tool for the simultaneous retrieval of both azimuthal and radial location of damages. The imaging is completed by converting the spectrogram into a polar image of the domain.

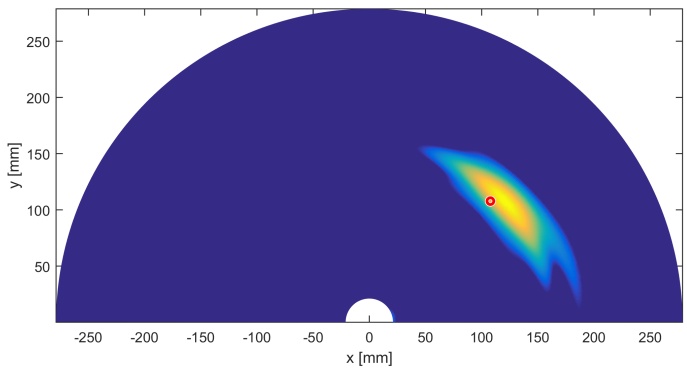

Figure 55: Re-mapped spectrogram of the signal $h(x)$ in Cartesian coordinates. Red circle: actual location and size of the damage.

4.4.4 Experimental Results

The technique presented above is applied to the signal recorded by the spiral FSAT prototype for different damage scenarios. A number different scenarios are tested, featuring both single and multiple damage sites at different radial distances from the FSAT as well as azimuthal locations. The first case presented is that of a single damage placed at 90° and 6 in away from the FSAT center, Figure 56(a). As expected, a high-energy spot appears in the proximity of the actual location of the magnet's stack, with a localization error below 20 mm. Figure 56(b) reports the remapped spectrogram for a single damage placed at 135°, again showing excellent agreement between the actual location of the damage and the one predicted by the spiral FSAT. Even for this direction (135°), for which some directionality disruption was observed in actuation mode, Figure 24(d), the location of the damage is reconstructed quite well, with a location estimate error below 35 mm.

Next, two more complicated scenarios are tested: the first features 4 scatterers at 4 different angular locations and different radial positions, while the second features 2 scatterers at the same angular location with different radial positions ("shadow mode"). The results are reported under the form of remapped spectrograms in Figure 57. As it can be seen, high

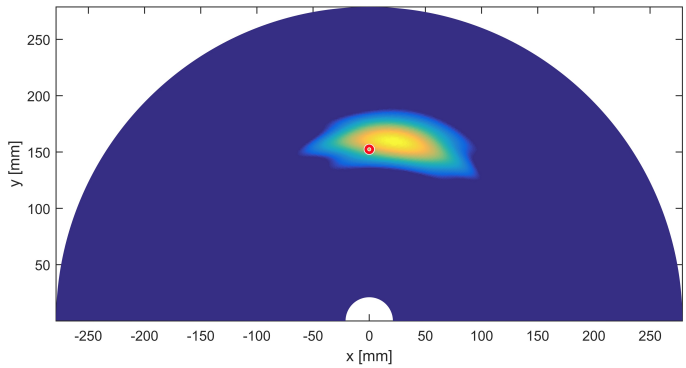

(a) 45° and 6 in

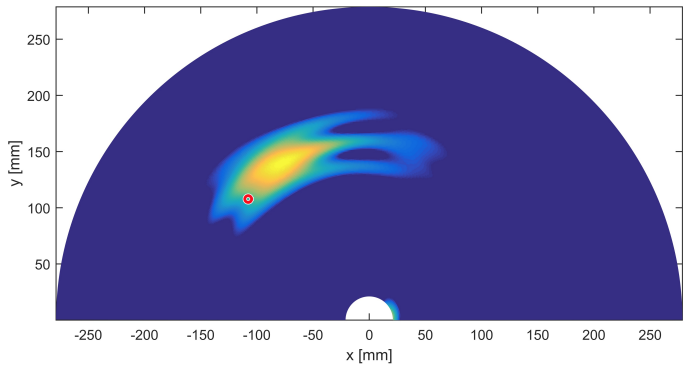

(b) 45° and 6 in

Figure 56: Re-mapped spectrogram of single acoustic source scenarios at different radial and azimuthal locations from the FSAT center location. Red circle: actual location and size of the damage.

energy spots are still present in the proximity of the actual damages locations. In this plots it can be noted that the relative amplitude of the peaks associated with different damages varies. The reasons behind this phenomenon are two: (i) the broadband signal used as the interrogation input does not provide a sufficiently constant actuation authority throughout the FSAT frequency bandwidth, and (ii) being the radial distance variable, wave packets are subjecy to attenuation due to cylindrical spreading. This varies with the traveled distance and represents a factor that contributes to the non-uniformity of the peaks amplitude.

This second reason can be addressed for the case of metallic materials by scaling the spatial trace amplitude of $h(x)$ by a factor of $\sqrt{x}$, which corresponds to the attenuation associated to energy spreading in bi-dimensional domains. For the case of composite materials

the issue is more complex, and ad hoc studies regarding composite directional attenuation are required. Since this improvement does not substantially change the results, its implementation is not performed.

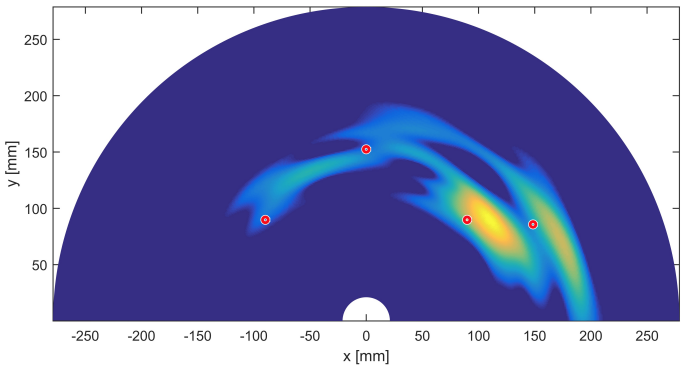

(a) 30° and 6.75 in, 45° and 5 in, 90° and 6 in, and 135° and 5 in

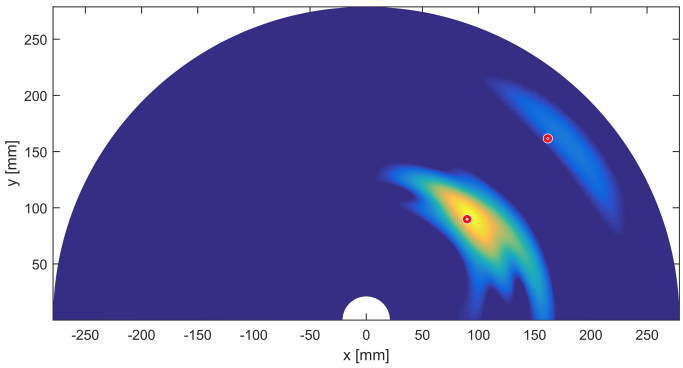

(b) 45° and 6 in, and 45° and 9 in

Figure 57: Re-mapped spectrogram of multiple acoustic source scenarios at different radial and azimuthal locations from the FSAT center location. Red circle: actual location and size of the damage.

4.5 Damage Detection in Composites

According to literature [33], much of the work done with GW imaging algorithms has been applied to isotropic media, such as aluminum plates, in a non-dispersive frequency regime. However, composites are in widespread use in modern aerospace structures. As with all plate-like structural components, these materials are dispersive and capable of supporting multiple propagating modes. In addition, composites also exhibit some degree of anisotropy meaning that the dispersive nature of the material is direction dependent, which constitutes

an additional, complex, challenge.

Given the promising results obtained in actuation mode on the spiral FSATs attached to the composite plates tested in Section 3.4 the employment of such devices is now tested to verify their damage detection capabilities through pulse-echo operations. In the same way as it was presented in Section 4.3, the devices are expected to generate Lamb waves (pulse) whose reflections off ddamage sites are sensed with the same device (echo) and a damage map is created by analyzing the spectrogram of the collected signal.

As discussed previously, in order to locate acoustic events, bi-dimensional imaging through STFT of the collected signals needs to be performed. As seen before, the estimate of the azimuthal location of the simulated damage can be retrieved through the directionality-frequency mapping associated with the transducer. Moreover, the estimate of the radial location of the damage sites can be evaluated through TOF retrieval combined with a dispersion compensation technique.

4.5.1 Algorithm for Damage Localization

It is worth noting that the procedure detailed in Section 4.4.2 is generally valid for isotropic media, for which iso-frequency dispersion relations are represented by circles in the wavenumber domain, i.e. group velocities are independent on the direction. This is not the case anymore when dealing with composites. Like all plate-like structures, these materials are dispersive and capable of supporting multiple propagating modes. In addition, composites also exhibit anisotropy even for quasi-isotropic layups, meaning that the dispersive nature of the material is direction dependent [33]. In other words, composites are characterized by group velocities that depend not only on frequency, but also on the wave vector. Figure 58 reports the group velocity as a function of frequency for the GlassUD and GlassQI laminates for three different directions: 0° (black curve), 45° (red curve), and 90° (blue curve). As it can be seen, the variation with respect to the azimuthal position of the wave vector increases for increasing levels of anisotropy of the laminate. For this reason, the procedure that maps $g(t)$ to $h(x)$ illustrated in Section 4.4.2 cannot be used.

A simple idea that allows to circumvent this problem is that of exploiting the intrinsic

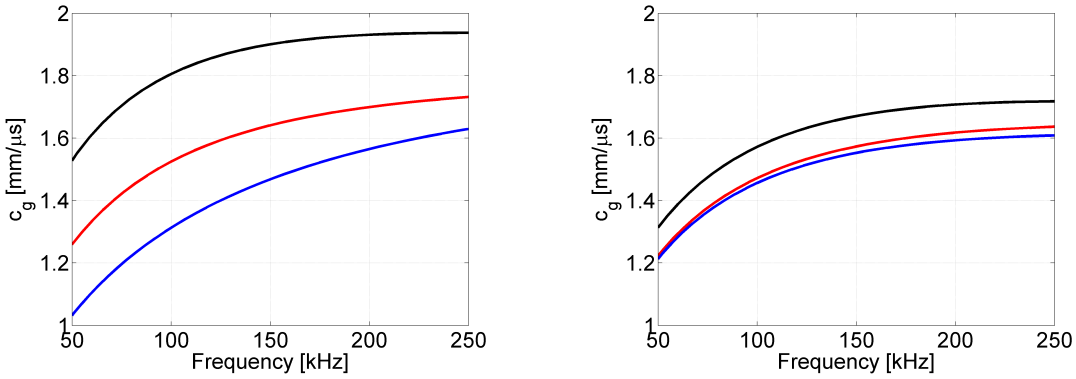

(a) GlassUD

(b) GlassQI

Figure 58: Group velocity vs. frequency for the plates under consideration. Black curve: 0°. Red curve: 45°. Blue curve: 90°.

directional properties of the spiral FSAT to re-map both axis of the spectrogram associated with the baseline subtracted signal $g(t)$. Within this scenarion, not only the frequency axis can be mapped to angles, but also the time domain axis can be mapped to distances without the requirement of having to use a dispersion compensation procedure. To illustrate this, let $g(t)$ be the signal carrying the informations about the response of the plate according to Equation (46). For this signal, the spectrogram carrying information about the short-term, time-localized frequency content of $g(t)$ can be easily computed through the STFT algorithm

$$\text{spectrogram}(t, \omega) = |\text{STFT}(t, \omega)|^2 . \tag{52}$$

On the spectrogram, a first operation can be immediately performed: by exploiting the directionality-frequency mapping associated with the spiral FSATs, the spectrogram can be transformed from spectrogram(t, ω) to spectrogram(t, ϑ). Then, the time domain needs to be remapped to space. This can be done simply by exploiting the directionality-frequency map associated with the spiral FSAT design, in a much simpler way than the one that involved the use of dispersion compensation outlined in Section 4.4.2. In detail, the time, t, can be transformed into space, x, simply by multiplying each azimuthal line of the spectrogram with the group velocity, c_{gr}, corresponding to that particular direction and frequency, which are univocally determined by the spiral FSAT design characteristics. This operation is performed for each i-th azimuthal line associated with the spectrogram,

such that

$$x(\vartheta_i) = c_{gr}(\vartheta_i)t. \tag{53}$$

As evident from Equation (53), the extension of spatial coordinate x varies for each azimuthal location, since it depends on the value of the group velocity associated with the i-th direction. The spectrogram is thus remapped by interpolation on a regularly spaced x-axis such that: the horizontal axis represents space (which is the same of every azimuthal line), and the vertical axis represents angles. As seen before, a third dimension indicating the amplitude of a particular wavenumber (angle) at a particular spatial coordinate (radial location) is represented by the intensity or color of each point in the image. This can finally be transformed into a polar map that carries the information about location of the acoustic events whose features are contained in $g(t)$.

The procedure described above provides the desired azimuthal and distance information that allows to localize the damage through the STFT algorithm in presence of anisotropic group velocities.

4.5.2 Experimental Results

The technique presented above is exploited to estimate the location of simulated damages by analyzing the signals recorded by the spiral FSAT prototypes employed on the GlassUD and GlassQI plates. As done for the aluminum plate case, damage sites are simulated through magnets, since they provide a fast and non-invasive way to setup different damage configurations. In detail, each damage is simulated through stacks of 4 magnets (1 on the back of the plate, and 3 on the front), which each magnet having a diameter of 19 mm, and a thickness of 5 mm. Two sample damage configurations are represented in Figure 59.

The experimental setup and procedures are identical to the one described in Section 4.4.4. Before presenting the results for different damage scenarios the analysis steps of Section 4.5.1 are now detailed for the the case of a single damage positioned at a radial distance of 127 mm (5 in) from the device center and forming an angle of $-45°$ with respect to the device reference orientation for the GlassUD plate.

As done before, the baseline response of the plate is recorded first. Figure 60(a) shows the

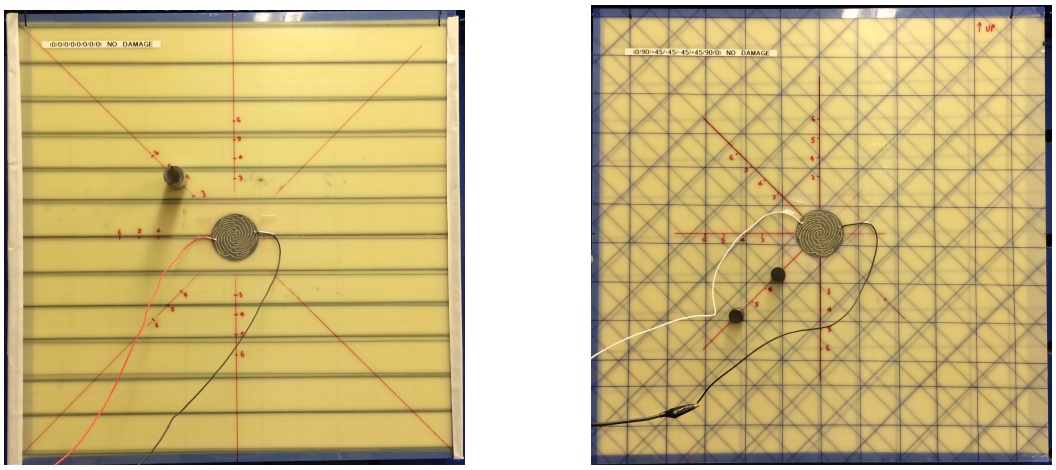

(a) GlassUD (b) GlassQI

Figure 59: Experimental setup for the FSAT tests on composites in pulse-echo mode.

time trace as recorded by the device for the pristine plate condition, i.e. with no simulated damages. Later, a simulated damage is added to the plate in the location described above. The response recorded by the device is reported in Figure 60(b). From a visual inspection of the two signal, it can be stated that no damage signature is clearly visible in this case. One thing that can be noticed in both signals are distinguished wave packets at approximately 100 μs, 220 μs, and 350 μs.

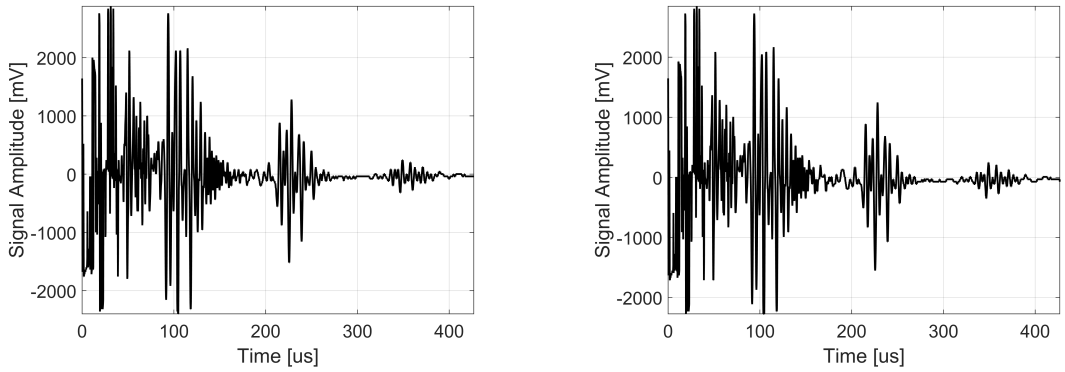

(a) (b)

Figure 60: (a) Baseline signal recorded by the spiral FSAT. (b) Signal recorded by the spiral FSAT with a damage located at 5 in from the device center, with an angular position of $-45°$.

In order to highlight the damage signature, baseline subtraction is performed, and the resulting signal is reported in Figure 61. As it can be seen, its amplitude is much smaller

if compared with the one of Figure 50. This is due to the much higher level of material attenuation that is characteristic of composites [12]. Despite of this, the damage signature is still clearly visible.

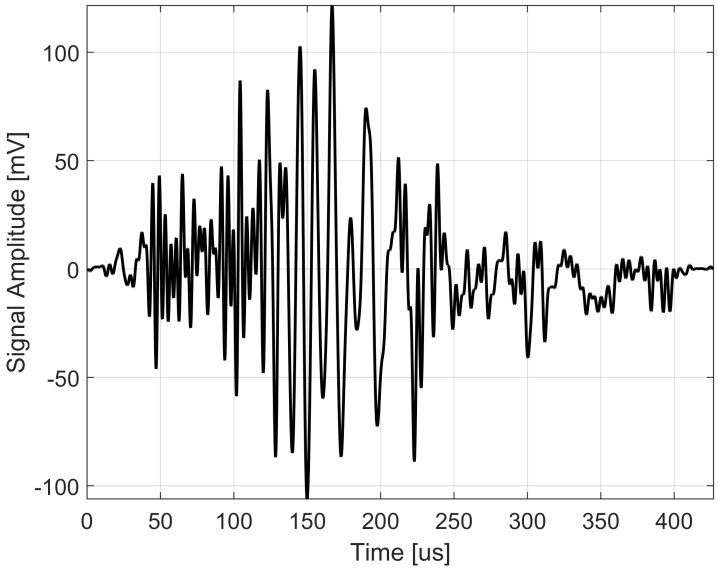

Figure 61: Signal $g(t)$ computed by subtracting the baseline signal to the one recorded with the simulated damage on the structure.

According to Equation (46), this signal corresponds to the time trace $g(t)$, upon which the technique discussed in Section 4.5.1 can be applied to highlight the damage location. To this aim, the spectrogram of the signal of Figure 61 is computed through the STFT algorithm. Figure 62 shows the result of this operation, where it can be seen that the spectrogram is characterized by a localized high energy spot for a frequency of approximately 100 kHz and an time of 150 μs.

In order to associate these values to physical coordinates, the frequency is mapped to the angle and the time is mapped to space according to the procedure above. The resulting spectrogram is reported in Figure 63 where it can be seen that the high energy spot of the spectrogram gives a very good estimate of the actual location of the damage (white circle), with an error that is below 15 mm.

The representation of the spectrogram of Figure 63 is finally re-mapped to physical coordinates by noting that angle and radial distance are, in fact, the polar coordinates

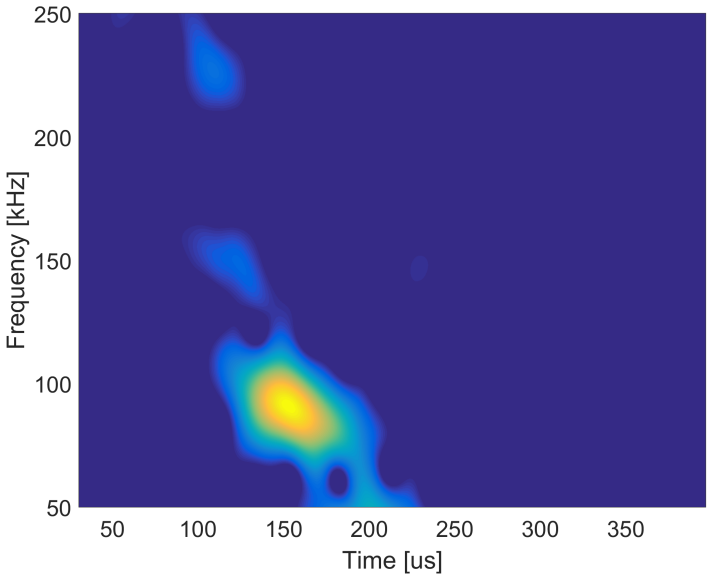

Figure 62: Spectrogram of the signal $g(t)$. The damage signature is evident.

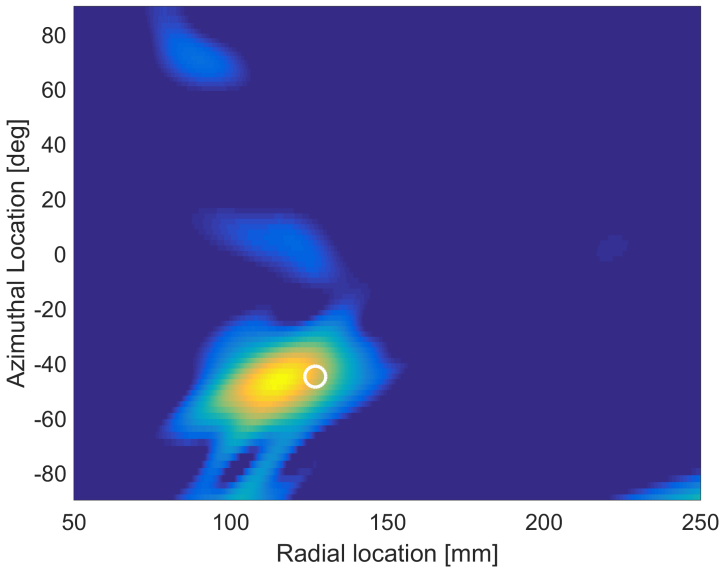

Figure 63: Spectrogram of the signal $g(t)$ with (i) the frequency axis replaced by the corresponding angle, and (ii) the time axis replaced by space. White circle: actual location of the damage.

associated with the map. Figure 64 shows the the spectrogram re-mapped in Cartesian coordinates, where indications on actual location *and size* of the damage are also provided (red circle).

In light of the results obtained above, a number of different damage scenarios have been

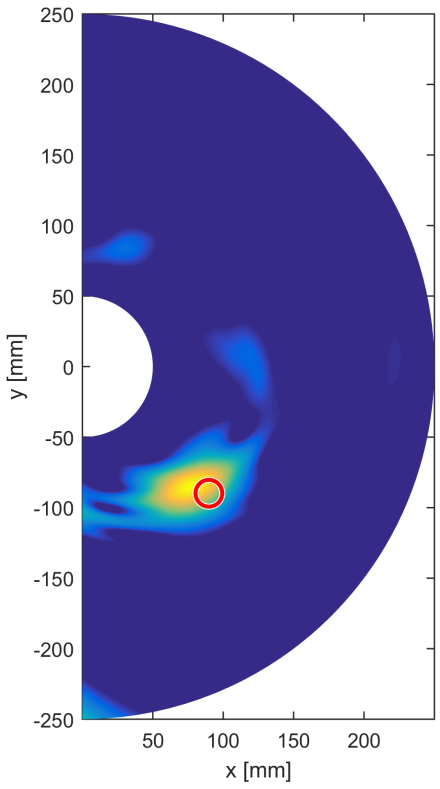

Figure 64: Re-mapped spectrogram of the signal $g(t)$ in Cartesian coordinates. Red circle: actual location and size of the damage.

tested for the GlassUD and the GlassQI plates, featuring both single and multiple simulated damage sites at different radial distances from the spiral FSAT as well as azimuthal locations. Results for the spiral FSAT on the GlassUD plate are presented in Figure 65 for single damage scenarios, and Figure 66 for multiple damage scenarios. Results for the spiral FSAT on the GlassQI plate are subsequently presented in Figure 67 for single damage scenarios, and Figure 68 for multiple damage scenarios. As it can be observed, in both laminates the spiral FSATs are able to reconstruct with remarkable accuracy the location of damage sites, with a maximum error below 15 mm.

As previously observed for the device mounted on an aluminum plate, localization accuracy deteriorates when approaching the higher portion of the device bandwidth, for which directionality distortion in actuation mode where recorded. In addition, it has to be noted that, due to the size of the magnets used to simulate the damage, the shadowed damage site

is not detected in any of the composite laminates tested, as reported in Figure 66(c) for the GlassUD plate, and Figure 68(c) for the GlassQI one. Nonetheless, the overall performance of the devices is considered very good.

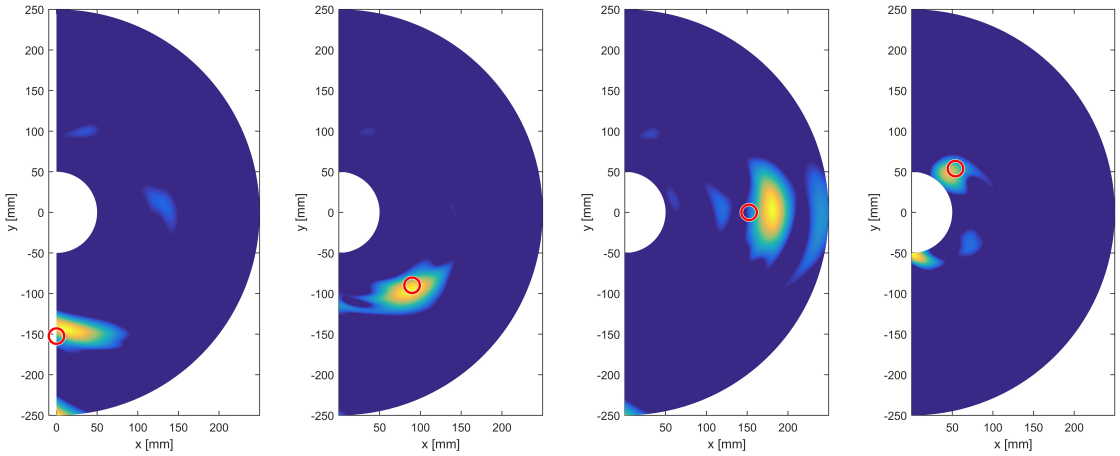

(a) $-90°$ and 6 in (b) $-45°$ and 5 in (c) $0°$ and 6 in (d) $45°$ and 3 in

Figure 65: GlassUD plate pulse-echo results: remapped spectrogram of single acoustic source scenarios at different radial and azimuthal locations from the FSAT center location. Red circle: actual location and size of the source.

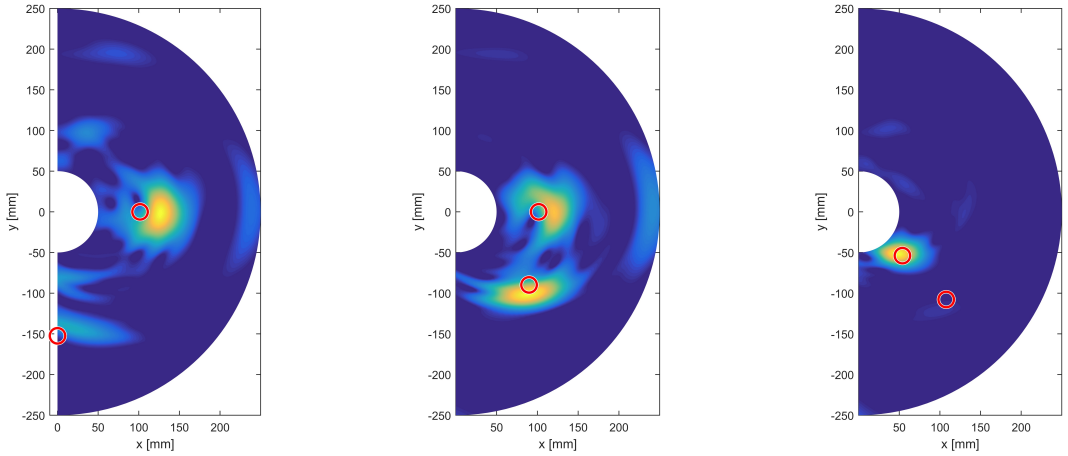

(a) $-90°$ and 6 in & $0°$ and 4 in (b) $-45°$ and 5 in & $0°$ and 4 in (c) $-45°$ and 3 in & $-45°$ and 6 in

Figure 66: GlassUD plate pulse-echo results: remapped spectrogram of multiple acoustic sources scenarios at different radial and azimuthal locations from the FSAT center location. Red circle: actual location and size of the source.

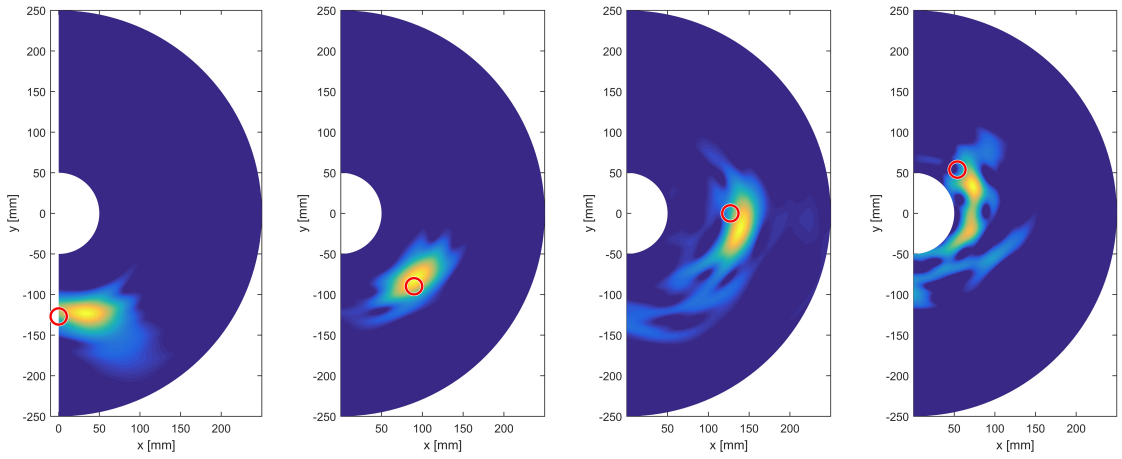

(a) $-90°$ and 5 in (b) $-45°$ and 5 in (c) $0°$ and 5 in (d) $45°$ and 3 in

Figure 67: GlassQI plate pulse-echo results: remapped spectrogram of single acoustic source scenarios at different radial and azimuthal locations from the FSAT center location. Red circle: actual location and size of the source.

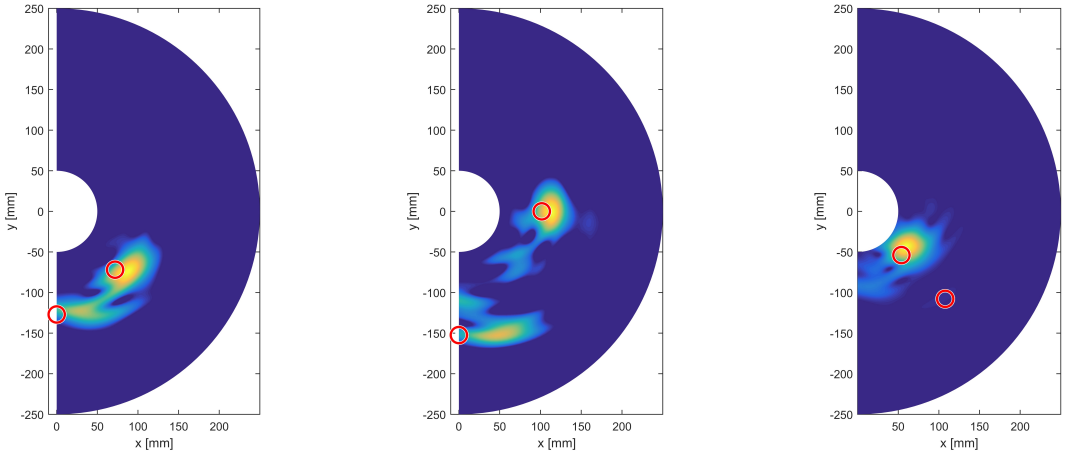

(a) $-90°$ and 5 in & $-45°$ and 4 in

(b) $-90°$ and 6 in & $0°$ and 4 in

(c) $-45°$ and 3 in & $-45°$ and 6 in

Figure 68: GlassQI plate pulse-echo results: remapped spectrogram of multiple acoustic sources scenarios at different radial and azimuthal locations from the FSAT center location. Red circle: actual location and size of the source.

4.6 Conclusions

In this chapter, experimental verification of damage detection performance of the spiral FSATs operated in pulse-echo mode have been presented both for isotropic and anisotropic plates. In the process, damage imagining techniques based on the evaluation and re-mapping

of the baseline subtracted spectrogram of the signal carrying information regarding the position of the damage sites have been outlined and discussed. Imagining results showed a consistent spiral FSAT performance with localization errors consistently below 30 mm.

In the next chapter the concept of sensor design by assigning its electrode shape in the wavenumber domain will be extended to strain sensing applications. Analytical developments towards the definition of a new device, termed the Acoustic Wave Rosette, will be discussed at length and its operations will be evaluated from a numerical and experimental standpoint.

CHAPTER V

ELECTRODE PATTERNING FOR STRAIN SENSING: THE ACOUSTIC WAVE ROSETTE

5.1 Overview

The concept of sensor design by assigning electrode shapes in the wavenumber domain is extended to a novel application that is of particular interest for SHM systems: strain sensing. The concepts and developments presented herein can be viewed as an extension of the existing electrode patterning procedures widely exploited for the design of interdigitated transducers (IDTs) as part of Surface Acoustic Wave (SAW) devices [36]. Firstly, the analytical framework for one-dimensional and two-dimensional periodic electrode layouts are generated and tailored to strain sensing applications. In their essence they rely on monitoring frequency shifts of radiation associated to local straining of the electrode patterning.

This leads to the concept of the Acoustic Wave Rosette (AWR), a transducer characterized by electrode patterns whose wavenumber representation features maxima corresponding to specific strain directions. The concept is verified numerically through analytical elasticity-based solutions for (i) mono-axial traction, and (ii) pure-shear scenarios. Experimental verification of the pattern filtering properties is then performed by synthesizing the transducer pattern through measurements from an SLDV. Even though upscaling of the global dimensions of the transducer is adopted to best exploit the experimental equipment available, results show how the patterning is indeed capable of acting as a multi-band spatial filter suitable for strain sensing.

The properties of the AWR concept suggest that frequency shifts of radiation can be consistently associated with local straining of the hosting medium. In addition, given the envisioned low-power consumption characteristics of SAW devices [98], this can enable wireless, multi-strain component interrogation of a structure with a single device.

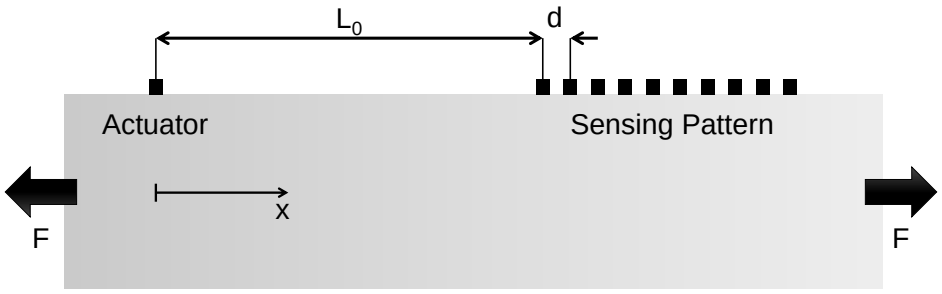

Figure 69: 1D strain sensing concept. F represents a generic load condition.

5.2 Electrode Patterning for Strain Sensing

5.2.1 IDT for SAW-based Strain Sensing

The use of IDT patterns for SAW-based strain sensing relies on the local generation of a surface wave that is then collected by an electrode deposited according to a 1D periodic pattern, Figure 69. The IDT acts as a spatial filter centered at the frequency corresponding to the SAW wavelength $\lambda = d$, with d denoting the electrode spacing. Application of a load F induces a strain ε which alters the spacing. Therefore $d = d(\varepsilon)$, which causes a corresponding frequency shift recorded by the IDT, as a result of $\lambda = \lambda(\varepsilon)$. The principle can be illustrated mathematically by expressing the layout of the sensing material (black rectangles in Figure 69) as

$$f(x) = \sum_{i=0}^{I} \delta(x - (x_i + u_i)) \tag{54}$$

where x_i is the position of the i-th electrode, which, in turn, can be explicitly written as

$$x_i = L_0 + id \tag{55}$$

being L_0 the distance between the actuator position and the first electrode, u_i the axial displacement at the i-th electrode location due to the applied load F, and $\delta(\cdot)$ the Dirac-delta function. The FT of Equation (55) leads to its wavenumber domain representation

$$D(k(\omega)) = \sum_{i=0}^{I} e^{-jk(\omega)(x_i+u_i)}. \tag{56}$$

where I is the number of the electrodes (black rectangles in Figure 69).

Interesting considerations can be made substituting Equation (55) into Equation (56). In particular, Equation (56) can be rearranged as

$$D(k(\omega)) = \sum_{i=0}^{I} e^{-jk(\omega)id(1+\bar{\varepsilon}_i)} \tag{57}$$

where $\bar{\varepsilon}_i$ is the *local* axial straining seen by the i-th electrode.

If the assumption that the strain level is constant underneath the sensing device holds

$$\bar{\varepsilon}_i = \hat{\varepsilon} = const \tag{58}$$

Equation (57) can be further rearranged as follows

$$D(k(\omega)) = \frac{\sin(\frac{I}{2}k(\omega)d(1+\hat{\varepsilon}))}{\sin(\frac{1}{2}k(\omega)d(1+\hat{\varepsilon}))}. \tag{59}$$

From Equation (59) it is evident that the function $D(k(\omega))$ reaches local maxima when its denominator goes to zero, which happens for the following condition

$$\frac{1}{2}k_M(\omega)d(1+\hat{\varepsilon}) = 2p\pi \tag{60}$$

where p is integer-valued. Equation (60) relates the maxima of $D(k(\omega))$ to the strain $\hat{\varepsilon}$.

The combination of (i) the wavenumber-strain relationship provided by the transducer design, Equation (60), and (ii) the wavenumber-frequency mapping defined by the considered dispersion branch of the underlying medium leads to a frequency-strain correlation that determines the axial straining of the elastic medium. In other words, the transducer acts as a spatial filter tuned at a frequency that is determined by the spacing of the sensing material (d in Figure 69). Figure 70 shows the filtering properties of a patterning with a 10 MHz periodicity. The spectrum of the interrogating wave is represented by the dashed

black curve, while the one associated to the voltage collected by the sensing pattern ($I = 64$) is represented by the solid black curve (both spectra are normalized to one). As it can be seen, the pattern filters the broadband input sharply around its design frequency.

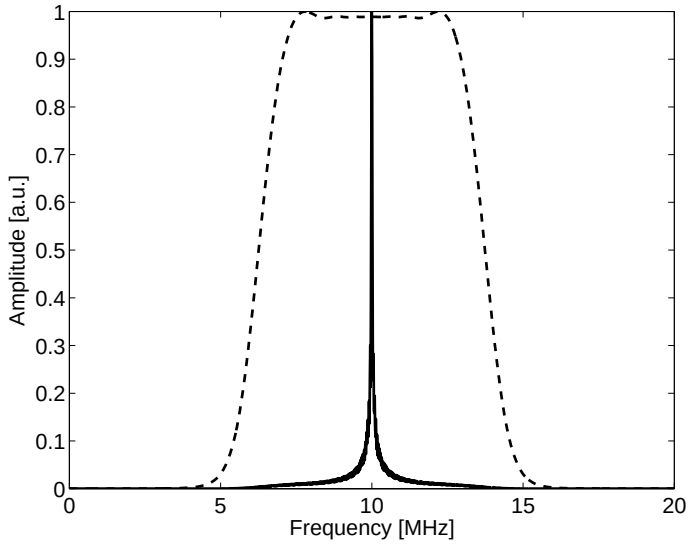

Figure 70: Example of filtering properties associated to transducer patterning.

When the hosting medium is stretched, the distance d changes, thus shifting the tuning frequency associated to the patterning. This shift defines a one-to-one relation between the frequency maximum of the spectrum associated to the voltage signal recorded by the device, and the undergoing structural strain.

For the case of $p = 1$, that is the one of interest since it represents the filtering associated with the fundamental periodicity d, this condition is readily obtained from Equation (60) as

$$f_M(\hat{\varepsilon}) = \frac{f_{M_0}}{(1 + \hat{\varepsilon})} \tag{61}$$

where f_{M_0} is the center frequency associated with the pattern in the unstretched condition, and a non dispersive wave is considered, for which $k_M(\omega) = 2\pi f_M / c_p$, with c_p denoting the phase velocity of surface waves (Rayleigh waves). The relation given by Equation (61) is reported in Figure 71 for an example case with $f_0 = 10$ MHz.

It is worth noting that, for practical applications, the assumption of constant strain requires a device of small dimensions, that thus operates at high frequencies [97].

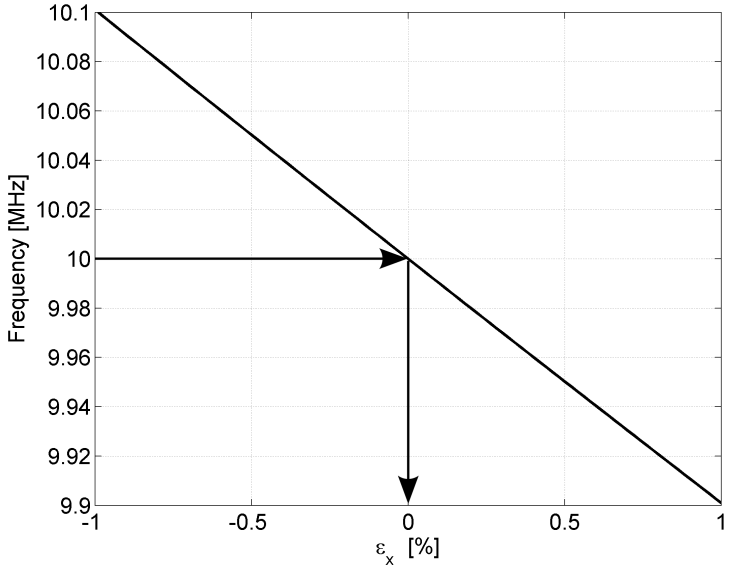

Figure 71: Strain VS. Frequency for an example scenario with a center frequency of 10 MHz.

To better understand this phenomenon, an example is shown. A clamped-free beam made of uniform isotropic material with the x-axis originating at the clamped end of the beam is considered. The beam operates under the action of an axially distributed load $p_0 = const$ applied at the centroid of the section. The axial displacement is given by

$$u(x) = \frac{p_0}{EA}\left(Lx - \frac{x^2}{2}\right) \tag{62}$$

where EA is the axial stiffness of the beam. The axial strain field varies linearly with respect to x

$$\varepsilon(x) = \frac{du(x)}{dx} = \frac{p_0}{EA}(L - x). \tag{63}$$

As stated above, in order to apply Equation (61) to determine the axial strain level, the assumption made in Equation (58) must hold. Unfortunately this is not the case here, since the axial strain field varies linearly with the x coordinate. The only possible counter-measure is to estimate a suitable operating frequency for which the difference between the function represented by Equation (57), which is exact in terms of strain levels, and the function represented by Equation (59), which is approximated, is negligible. The objective is then to estimate a frequency for which the differences between Equation (57) and Equation (59) are negligible.

To this aim, consider an actuator/sensor combo of the type of that of Figure 69 placed at $x = L/2$, and a load p_0 chosen such that the beam undergoes a local strain of 5%. For the sensor, two different patterning periodicity are chosen: the first one has an associated frequency $f_0 = 1$ MHz, while for the second one $f_0 = 50$ MHz. For both configurations the selected number of electrodes is $I = 64$.

The results are presented in Figure 72 in terms of patterning frequency output for the stretched case. As it can be seen, the choice of a suitable frequency range allows to minimize the difference between the actual spectrum (black curves), i.e. the one expressed by Equation (57), and the one approximated with constant strain assumption (red curves), i.e. the one expressed by Equation (59).

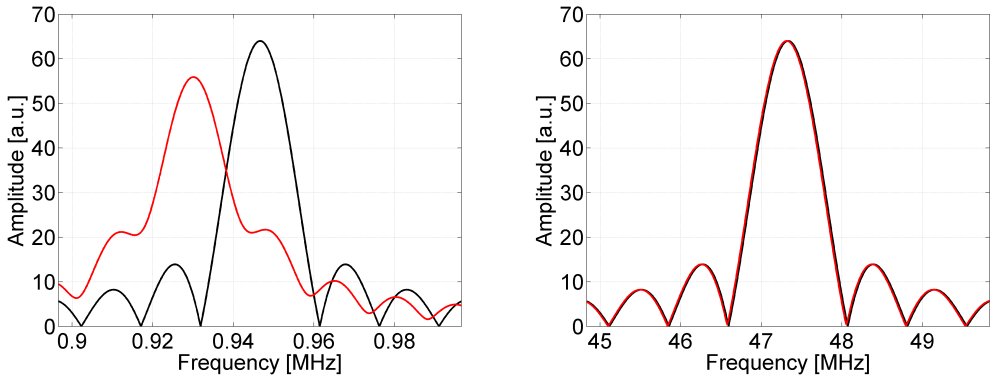

Figure 72: Comparison between actual and constant strain level approximation directivity functions for (a) $f_0 = 1$ MHz, and (b) $f_0 = 50$ MHz. Local axial strain level is 5% in both cases. Black curves: exact spectrum. Red curves: spectrum approximated with constant strain assumption.

In general, it is possible to identify a suitable frequency range that minimizes directionality distortion. This is associated to a maximum outer dimension of the sensing device, at which the undergoing straining of the structural component can be confidently estimated by means of Equation (61), which assumes a constant strain level underneath the device.

More in detail, the spatial scale derived by the analysis presented suggests frequency ranges for which surface (Rayleigh) waves are excited, confirming the non-dispersive nature of the interrogating waves involved. Moreover, it can be easily verified that a finite transverse dimension of the gratings does not affect the directionality of the grating itself.

5.2.2 Extension to 2D

The concept presented above can be readily extended to a bi-dimensional domain. The goal is to be able to measure the three surface-relevant strain components, namely ε_1, ε_2, and ε_{12}.

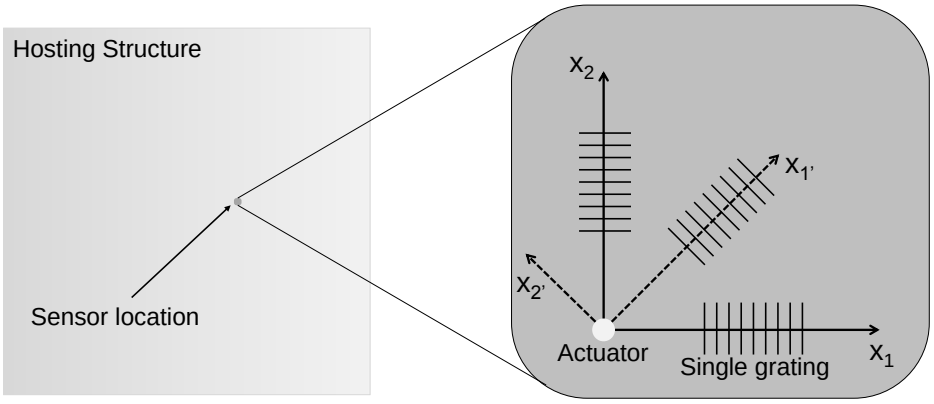

Figure 73: Bi-dimensional strain sensing concept. Single 1D gratings are arranged in a rosette configuration.

To determine the three independent components of strain, three linearly independent strain measures are needed, i.e. three patters positioned in a rosette-like layout are required, as sketched in Figure 73. In this scenario, each of the axial strains measured by the independent gratings needs to be rotated according to tensorial rotation rules

$$\varepsilon_{1'} = \frac{\varepsilon_1 + \varepsilon_2}{2} + \frac{\varepsilon_1 - \varepsilon_2}{2} \cos 2\vartheta + \varepsilon_{12} \sin 2\vartheta. \tag{64}$$

It is worth noting that such a device requires three separated IDTs and either (i) three separated sources of excitation consisting of plane waves in the pattern directions, or (ii) a circular wave source, which would imply an unnecessary spreading of energy in "dead" directions, i.e. in directions non aligned with the electrode patterns. For this reasons the solution of Figure 73 is not optimal. A new framework that exploits more advanced electrode patterning is thus derived for strain sensing applications.

5.3 The Acoustic Wave Rosette Principles of Operation

An extension of the rosette-like configuration presented above can be achieved exploiting the frequency-dependent directivity of Equation (15). As done for the case of the FSAT in Chapter 3, the transducer shape can be designed in the wavenumber domain by means of Equation (33). Later, the associated spatial shape of the electrode can be retrieved through IFT procedures from Equation (15), that is here re-written for sake of completeness

$$f(\boldsymbol{x}) = \frac{1}{N}\text{rect}\left(\frac{|\boldsymbol{x}|}{a}\right)\sum_{n=1}^{N}\cos(\boldsymbol{k_n}\cdot\boldsymbol{x}). \tag{65}$$

In Equation (65) the *sin*-like term of Equation (15) has been replaced by a *cos*-like one. This is done because the interrogating wave is envisioned to be generated at the center of the device, Figure 74, and for this configuration a *sine* generated pattern would lead to signal cancellation at transducer location azimuthally opposite to one another (light red areas), since *sine* patterns are anti-symmetric, while the interrogating wave is symmetric.

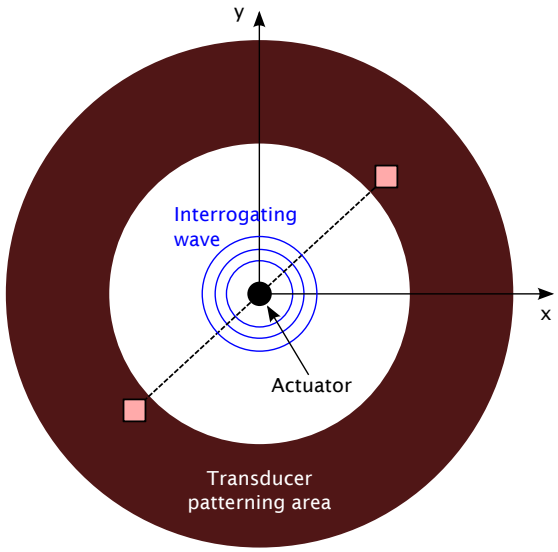

Figure 74: Schematic of the envisioned configuration of the AWR. Dimensions not to scale.

With this in mind, the rosette-like configuration of Figure 73, which features material distribution in three specific directions to enable strain retrieval through tensorial rotation, is ported to the wavenumber domain. More in detail, the material distribution corresponds to three maxima in the wavenumber domain corresponding to three wave vector directions.

Assuming an isotropic hosting medium, the design provided as an example in Figure 75 features a tri-directional wavenumber distribution associated with three different frequencies, which are represented by three different iso-frequency circles. With the wavenumber shape of the device in place, Equation (65) is then used to retrieve the spatial distribution of sensing material through IFT procedures.

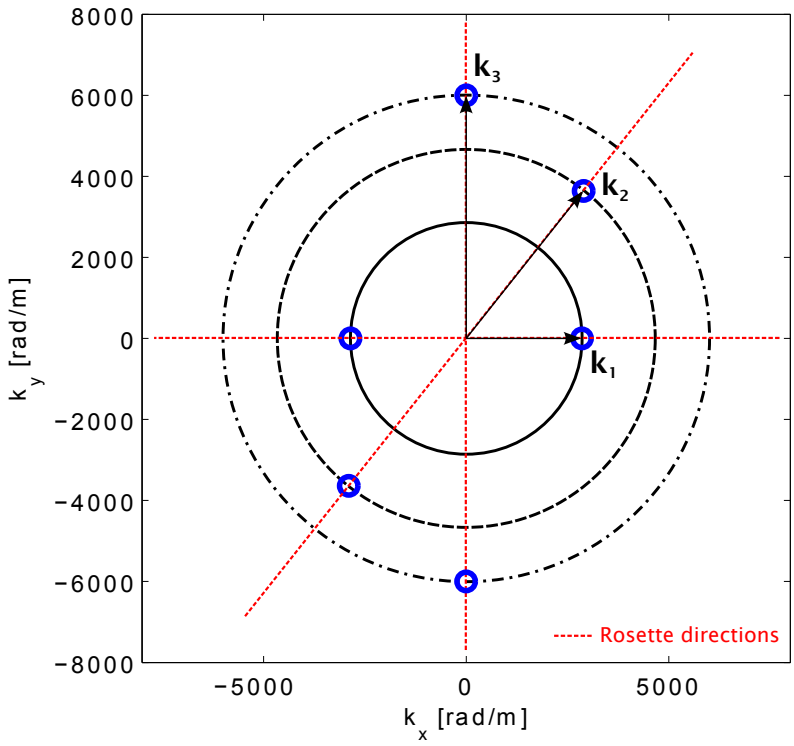

Figure 75: Schematic of the AWR directivity in the wavenumber domain.

Within this scenario, straining of the hosting medium deforms the electrode patterning. This generates a corresponding deformation of the wavenumber shape of the transducer (which is represented by three peaks in three different directions). In turn, peaks shift in the wavenumber domain trigger frequency shifts in the spectrum of the voltage sensed by the device, which can ultimately be associated to strain components.

5.3.1 Assumptions on Displacement Field and Sensor Spatial Shape

As seen in Section 5.2.1, a suitable frequency range must be selected in order to minimize directionality distortions. The sensor performance would be greatly affected by a non-uniform strain field underneath the transducer itself, and this poses an upper limit to the outer dimension of the transducer. The general case of a bi-dimensional, linear (or, without loss of generality, linearized) displacement field is considered

$$\begin{aligned} u &= u_{/x}x + u_{/y}y \\ v &= v_{/x}x + v_{/y}y \end{aligned} \tag{66}$$

where $(u,\, v)$ represent the displacement field in the Cartesian reference frame $(x,\, y)$, and $(\cdot)_{/\xi} = \frac{\partial(\cdot)}{\partial \xi}$ and are assumed to be constant terms. The corresponding strain field is readily obtained by differentiation

$$\begin{aligned} \varepsilon_x &= u_{/x} \\ \varepsilon_y &= v_{/y} \\ \varepsilon_{xy} &= \tfrac{1}{2}\left(u_{/y} + v_{/x}\right) \end{aligned} \tag{67}$$

where the naming of the variables involved is self-explaining.

For illustration purposes, the spatial shape of the sensor is simplified as follows (from Equation (65))

$$f(\boldsymbol{x}) = \cos(\boldsymbol{k}_0 \cdot \boldsymbol{x}) \tag{68}$$

where $\boldsymbol{x} = [x,\, y]^T$ is a generic position vection in the spatial domain, and $\boldsymbol{k}_0 = [k_{0_x},\, k_{0_y}]^T = k_0[\cos\vartheta_0,\, \sin\vartheta_0]$ denotes the location of a maximum of the electrode distribution in the wavenumber space. If compared with Equation (65) the limited spatial support term is dropped, and a single peak in the wavenumber domain is considered. The simplification is introduced to be able to illustrate the shift of a single peak to an underlying strain in the hosting medium.

5.3.2 Development of Strain-frequency Relation

Within these assumptions, the spatial shape of the sensor subject to a general displacement field of the type of that described by Equation (66) can be written as

$$f(\boldsymbol{x}) = cos(k_{0_x}(x+u) + k_{0_y}(y+v)) \tag{69}$$

Its wavenumber shape is retrieved by applying a bi-dimensional FT, which can be expressed analytically as

$$\begin{aligned}\mathcal{D}(k_x,k_y) = j\pi \quad & \left[\delta(k_{0_x}+u_{/x}k_{0_x}+u_{/y}k_{0_y}-k_x)\delta(k_{0_y}+v_{/x}k_{0_x}+v_{/y}k_{0_y}-k_y)+\dots\right. \\ & \left.\dots+\delta(k_{0_x}+u_{/x}k_{0_x}+u_{/y}k_{0_y}+k_x)\delta(k_{0_y}+v_{/x}k_{0_x}+v_{/y}k_{0_y}+k_y)\right].\end{aligned} \tag{70}$$

Equation (70) shows directivity maxima at

$$\begin{aligned}k_{x_M} &= k_{0_x}+u_{/x}k_{0_x}+u_{/y}k_{0_y} \\ k_{y_M} &= k_{0_y}+v_{/x}k_{0_x}+v_{/y}k_{0_y}.\end{aligned} \tag{71}$$

Adopting a coordinates change from Cartesian to polar, wavenumber components k_x and k_y are replaced by k_0 and ϑ_0. This is performed because radial shifts, rather than azimuthal, are of particular interests, given their direct relations, at least for isotropic materials, to frequency shifts through medium dispersion relations. Assuming (i) isotropic hosting medium, and (ii) Rayleigh waves propagation, the relation between the radial wavenumber $k_{0_M}=\sqrt{k_{x_M}^2+k_{y_M}^2}$ and the frequency ω is

$$\omega = c_R\, k_{0_M} \tag{72}$$

where c_R is the Rayleigh wave velocity, that, in turn, can be expressed as a function of shear waves velocity, $c_s=\sqrt{G/\rho}$ by [3]

$$\frac{c_R}{c_s} = \frac{0.87+1.12\nu}{1+\nu} \tag{73}$$

where ν is the Poisson's ratio of the considered medium.

Re-writing Equation (71) to highlight the radial wavenumber k_{0_M} yields

$$\begin{aligned}k_{0_M} &= \Big[(1+u_{/x})^2k_{0_x}^2+u_{/y}^2k_{0_y}^2+2(1+u_{/x})u_{/y}k_{0_x}k_{0_y}+\dots \\ &\quad \dots+v_{/x}^2k_{0_x}^2+(1+v_{/y})^2k_{0_y}^2+2(1+v_{/y})v_{/x}k_{0_x}k_{0_y}\Big]^{1/2}.\end{aligned} \tag{74}$$

Equation (74) can be linearized as follows

$$\begin{aligned}
(1+u_{/x})^2 &\approx 1+2u_{/x}\\
u_{/y}^2 &\approx 0\\
2(1+u_{/x})u_{/y} &\approx 2u_{/y}\\
v_{/x}^2 &\approx 0\\
(1+v_{/y})^2 &\approx 1+2v_{/y}\\
2(1+v_{/y})v_{/x} &\approx 2v_{/x}.
\end{aligned} \tag{75}$$

which yields

$$k_{0_M} = [(1+2u_{/x})k_{0_x}^2 + 2u_{/y}k_{0_x}k_{0_y} + (1+2v_{/x})k_{0_y}^2 + 2v_{/x}k_{0_x}k_{0_y}]^{1/2} \tag{76}$$

and

$$k_{0_M} = [(1+2u_{/x})k_{0_x}^2 + 2(u_{/y}+v_{/x})k_{0_x}k_{0_y} + (1+2v_{/y})k_{0_y}^2]^{1/2}. \tag{77}$$

Furthermore, substituting the relations of Equation (67) gives

$$k_{0_M} = [(1+2\varepsilon_x)k_{0_x}^2 + 4\varepsilon_{xy}k_{0_x}k_{0_y} + (1+2\varepsilon_y)k_{0_y}^2]^{1/2}. \tag{78}$$

Equation (78) can be further developed by noting that

$$\begin{aligned}
k_{0_x} &= k_0\cos\vartheta_0\\
k_{0_y} &= k_0\sin\vartheta_0.
\end{aligned} \tag{79}$$

to obtain

$$k_{0_M} = [(1+2\varepsilon_x)k_0^2\cos^2\vartheta_0 + 4\varepsilon_{xy}k_0^2\sin\vartheta_0\cos\vartheta_0 + (1+2\varepsilon_y)k_0^2\sin\vartheta_0]^{1/2} \tag{80}$$

which can be rearranged as

$$k_{0_M} = k_0[(1+2(\varepsilon_x\cos^2\vartheta_0 + \varepsilon_{xy}\sin 2\vartheta_0 + \varepsilon_y\sin^2\vartheta_0)]^{1/2}. \tag{81}$$

Furthermore

$$\left(\frac{k_{0_M}}{k_0}\right)^2 = 1+2(\varepsilon_x\cos^2\vartheta_0 + \varepsilon_{xy}\sin 2\vartheta_0 + \varepsilon_y\sin^2\vartheta_0). \tag{82}$$

Finally, introducing Equation (72) into Equation (82) yields

$$\varepsilon_x\cos^2\vartheta_0 + \varepsilon_{xy}\sin 2\vartheta_0 + \varepsilon_y\sin^2\vartheta_0 = \frac{1}{2}\left[\left(\frac{f_M}{f_0}\right)^2 - 1\right] \tag{83}$$

which represents the final relation between strain components and center frequencies recorded by the electrode pattern.

Looking at the terms present in Equation (83), the following considerations can be made:

- f_0 and ϑ_0 are assigned at the design stage;
- f_M is registered as the sensor response;
- ε_x, ε_y, and ε_{xy} are the unknowns of the problem.

It is easy to recognize that the left-hand-side of the frequency-strain relation of Equation (83) has the same form of the well-known relation used for strain rotation in strain rosettes [7].

5.3.3 Multi-component Strain Sensing

In order to find a unique relation between frequency peaks shifts and strain components, three different peaks with three different azimuthal locations in the wavenumber domain are necessary, thus $N = 3$ in the summation of Equation (65). The resulting AWR sensor is a device that is able to perform sensing of multiple strain components simultaneously by a proper arrangement of its electrode patterns.

Using the relation between frequency shifts and strain components found in Equation (83), a solving linear system can be set up in the form of

$$\boldsymbol{A}\boldsymbol{\epsilon} = \boldsymbol{b} \tag{84}$$

where

$$\begin{aligned} \boldsymbol{\epsilon} &= [\varepsilon_x,\, \varepsilon_y,\, \varepsilon_{xy}]^T \\ b_i &= 1/2 \left[(f_{M_i}/f_{0_i})^2 - 1 \right] \end{aligned} \tag{85}$$

where the i-th row of $\boldsymbol{A}$ is expressed as

$$\boldsymbol{A}(i,:) = \left[\cos^2 \vartheta_{0_i},\, \sin 2\vartheta_{0_i},\, \sin^2 \vartheta_{0_i} \right] \tag{86}$$

With the linear system of Equation (84) in place, the solution for $\boldsymbol{\epsilon}$ is easily obtained by inverting the matrix $\boldsymbol{A}$

$$\boldsymbol{\epsilon} = \boldsymbol{A}^{-1}\boldsymbol{b} \tag{87}$$

Considering for example the following directions:

- $\vartheta_0^{(1)} = 0$;
- $\vartheta_0^{(2)} = \pi/4$;
- $\vartheta_0^{(3)} = \pi/2$;

then the matrix $\boldsymbol{A}^{-1}$ is given by

$$\boldsymbol{A}^{-1} = \begin{bmatrix} 1 & 0 & 0 \\ 0 & 0 & 1 \\ -\frac{1}{2} & 1 & -\frac{1}{2} \end{bmatrix} \tag{88}$$

In this case ε_x is given by the shift of the first peak ($\vartheta = 0°$), ε_y by the shift of the third frequency peak ($\vartheta = 90°$), and ε_{xy} is given by a combination of the shifts of the three frequency peaks.

An alternative approach that is not investigated here would be that of employing a least squares solution. In this case, the number of frequency peaks (and thus directions in the wavenumber space) should be greater than the number of strain components to be determined ($N > 3$ in Equation (65)). Once the problem is setup, the solution can be found by means of the following system

$$\boldsymbol{\epsilon}^{LS} = (\boldsymbol{A}^T\boldsymbol{A})^{-1}\boldsymbol{A}^T\boldsymbol{b}. \tag{89}$$

5.3.4 AWR Multi-strain Detection Performance on an Axially and Transversally Loaded Square Plate

The analytical derivation presented above is adopted to test the performance of an AWR on an aluminum square plate. Two case studies are selected to test the transducer performance: (i) pure axial loading along the $x-$axis, and (ii) pure shear loading on the left-most edge of the plate. The schematic of the loading scenarios, and the position of the sensing device are reported in Figure 76. The elasticity solutions for load cases can be easily computed analytically. For the pure axial load case, the solution in terms of displacements is

$$\begin{aligned} u &= \tfrac{q}{E}x \\ v &= -\nu\tfrac{q}{E}y \end{aligned} \tag{90}$$

from which the strain field is readily derived

$$\begin{aligned} \varepsilon_x &= \frac{q}{E} \\ \varepsilon_y &= -\nu\frac{q}{E} \\ \varepsilon_{xy} &= 0. \end{aligned} \tag{91}$$

For the pure shear load case, the solution in terms of displacements is instead

$$\begin{aligned} u &= 0 \\ v &= \frac{q}{G}x \end{aligned} \tag{92}$$

from which the strain field is readily derived

$$\begin{aligned} \varepsilon_x &= 0 \\ \varepsilon_y &= 0 \\ \varepsilon_{xy} &= \frac{q}{2G}. \end{aligned} \tag{93}$$

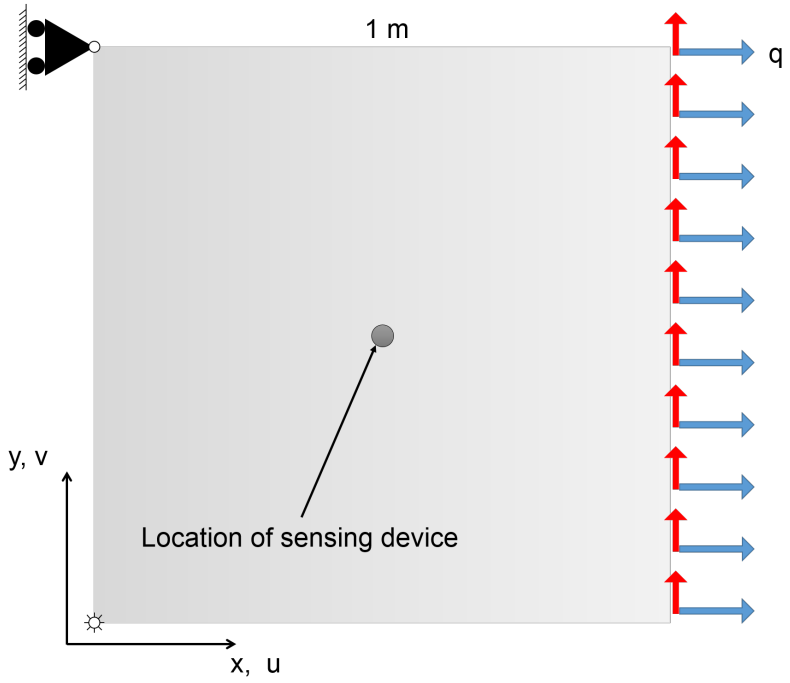

Figure 76: Schematic of the numerical problem under analysis. The sensing device is located at the center of the plate. The origin of the Cartesian axes is located at the bottom-left hinge. Blue arrows: pure axial load scenario. Red arrows: pure shear load scenario.

5.3.4.1 Design

The AWR electrode patterning is designed in the wavenumber domain according to the procedure illustrated in Section 5.3.2. In particular, frequency peaks at 35, 45, and 55 MHz are selected at $-30°$, $90°$, and $120°$ wavenumber directions, respectively. The dispersion curves considered are those associate to a 0.81 mm thick aluminum plate. The resulting sensor spatial shape is represented in Figure 77: the outer dimension of the device is set to 15 mm. As it can be seen the AWR electrode pattern has the shape of a ring, with an inner cut diameter of 2 mm, which corresponds approximately to 15 times the wavelength associated to the lowest wavenumber peak. As outlined during the design stage, this is done to take into account the presence of an actuation source in the center of the AWR pattern that is responsible of generating the scanning wave packet to be read by the electrode pattern to retrieve strain components.

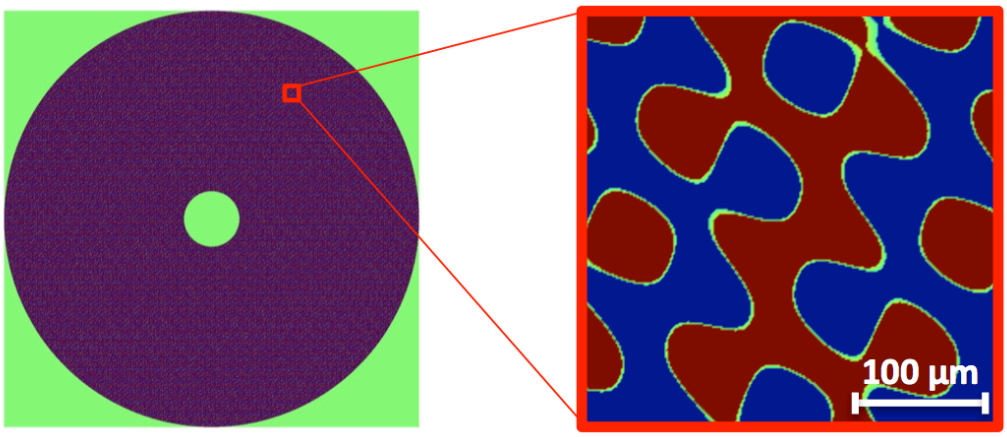

Figure 77: AWR shape in the spatial domain (threshold $\eta = 0.03$). Outer diameter dimension = 15 mm, inner diameter dimension = 2 mm.

5.3.4.2 Numerical Simulation

With the elasticity solution and the sensor patterning in place, the following procedure is simulated numerically: first an analytical pre-strain condition is imposed on the hosting structure and the displacement field is computed. A wave packet is then fired from the actuator location, positioned at the center of the pattern, in order to interrogate the electrodes. The actuation is performed through a special wave packet which is the sum

of three TB-like signals. This custom-designed signal, termed Orthogonally Shaped Triple Tone Burst (OS-TTB), is used as the interrogating signal featuring a center frequency of 45 MHz with 4-cycles assigned to the central burst, Figure 78. OS-TTB signals are very convenient because they provide a wide frequency band excitation while keeping the signal footprint limited in the time domain. For this reason they are the wave packet of choice in this numerical analysis.

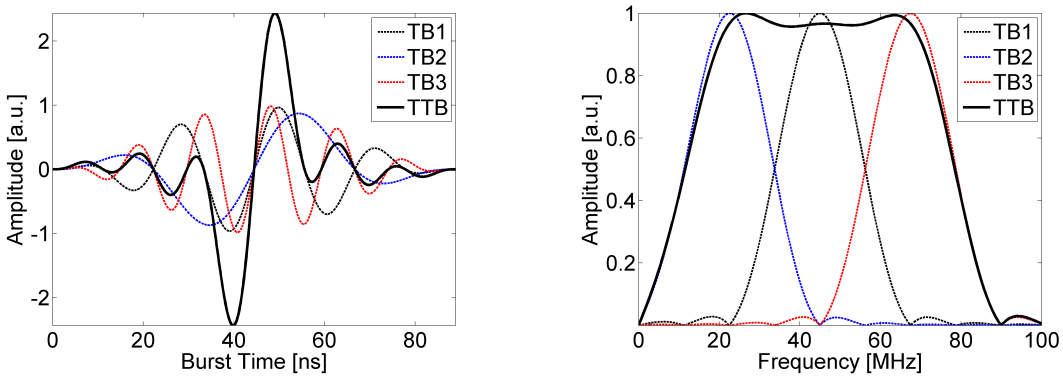

(a) Time Domain (b) Frequency Domain

Figure 78: Orthogonally shaped TTB used to achieve a broadband excitation.

After the interrogating signal is generated, the response at the transducer location is collected. To accomplish this task, the wave field at each location is weighted with the corresponding electrode polarization (± 1 for red and blue areas in Figure 77, respectively), and summed up over the entire area of the AWR. More in detail, the plate response is generated and measured over a grid of M x M points, with M = 2048. Sampling of the measurement points is simply performed by evaluating the sensor shape function $f(\boldsymbol{x}_j)$ at grid point $\boldsymbol{x}_j$. To this aim, let $w(\boldsymbol{x}_j, t)$ denote the out-of-plane displacement of the plate measured at location $\boldsymbol{x}_j$. The transducer response is then computed as

$$w(t) = \sum_{j=1}^{M^2} f(\boldsymbol{x}_j) w(\boldsymbol{x}_j, t) \tag{94}$$

where the weights $f(\boldsymbol{x}_j)$ are calculated based on the threshold sensor of Figure 77 re-mapped over the response grid.

The time-domain signal is then transformed into the frequency domain by means of

FT, frequency shifts about the reference condition are computed, and the system of Equation (87) is solved for strain components.

5.3.4.3 Considerations on Frequency Resolution and Peak Sharpness

It is worth noting that, when computing the FT of the sensor output, a fine frequency resolution is needed in order to achieve an acceptable precision level in the determination of strain components. For this reason, the Chirp Z-transform (CZT) algorithm is used instead of the conventional FFT algorithm. The benefit of using the CZT algorithm is that it allows the computation of the FT of a signal over a limited and selectable band, dramatically increasing the frequency resolution of the signal spectrum [62]. Figure 79 shows the error with respect to the analytical solution that is committed on the calculation of the axial strain level when adopting the CZT (red) and the FFT (black) to retrieve frequency peak shifts in a simple 1D case. As it can be seen, the CZT allows to achieve a higher precision, with an error on the strain value below 5% for strain levels as small as 7 $\mu\epsilon$. For the same strain level the FFT alghoritm presents an error with respect to the analytical strain value of about 80%. While FFT resolution can generally be improved by zero-padding, achieving the same precision as the one offered by the CZT would be impractical.

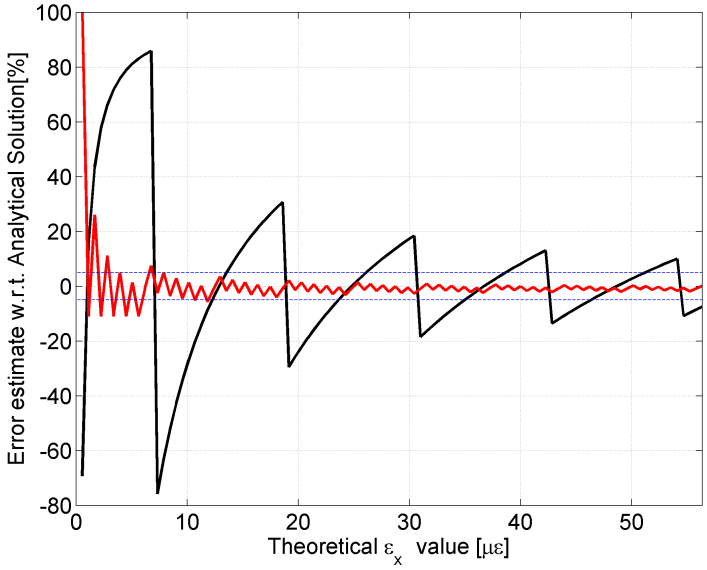

Figure 79: Error FFT VS. CZT. Black solid line: FFT error. Red solid line: CZT error. Blue dashed line: 5% error threshold.

In addition to frequency resolution, there is also another parameter that needs to be considered: device dimension. In SAW-based devices literature [10], the typical number of electrode pairs (a.k.a. "fingers number") used ranges from 64 to 128. These values are selected in order to achieve sharp filtering properties associated with the device. For the AWR the concept of electrode pairs cannot be defined; in his place, the concept of "equivalent fingers" is introduced. As indicated by literature, sharp filtering around the frequencies dictated by AWR patterns is supposed to be achieved with at least 64 radial repetitions of the pattern associated, in this case, with the lowest design frequency, i.e. for the one associated with the longest wavelength and the smallest wavenumber.

5.3.4.4 Results

For the axial load case, the results of the simulation in terms of signal spectrum are presented in Figure 80 for a distributed load of $q = 1$ GPa, while the corresponding strain components are reported in Table 5. For the shear load case, the results are instead presented in Figure 81, again for a distributed load of $q = 1$ GPa, and the corresponding strain components are reported in Table 6. As it can be seen, the matching between analytical values of strain and the one derived analyzing spectral shifts of the sensor inner patterning are in very good agreement, with a maximum error below 4% compared to analytical strain values.

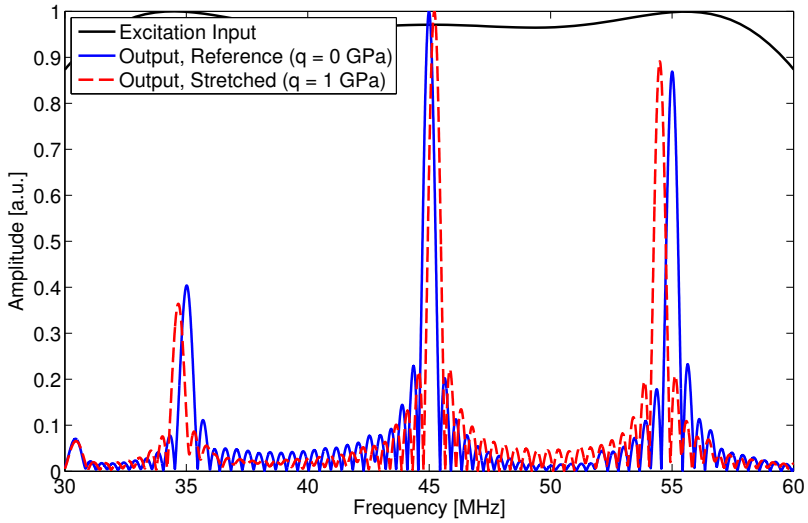

Figure 80: Frequency spectrum results for the simulated axial load configuration.

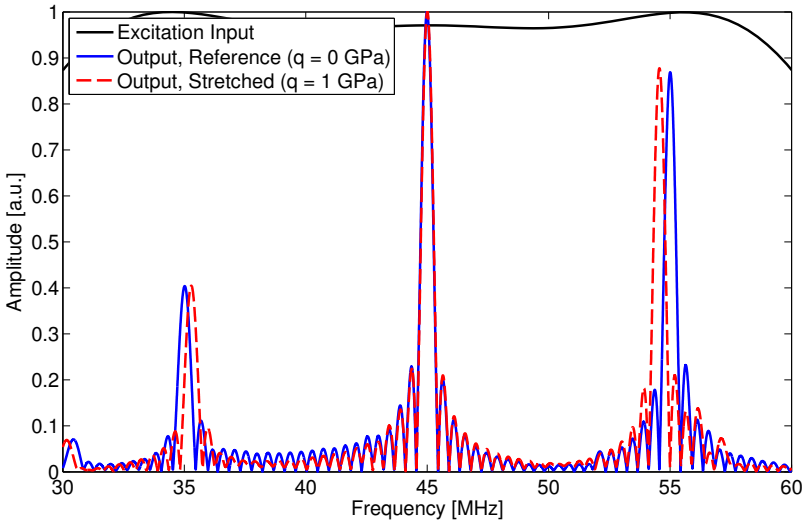

Figure 81: Frequency spectrum results for the simulated shear load configuration.

Table 5: Comparison between analytical values of strain components and measured ones for the axial load configuration.

	Analytical ($\mu\varepsilon$)	Measured ($\mu\varepsilon$)
ε_x	1414	1434
ε_y	-467	-485
ε_{xy}	0	-31

Table 6: Comparison between analytical values of strain components and measured ones for the shear load configuration.

	Analytical ($\mu\varepsilon$)	Measured ($\mu\varepsilon$)
ε_x	0	-49
ε_y	0	52
ε_{xy}	1881	1824

5.4 Experimental Proof of Concept of Multi-band Filtering Capabilities

The tri-band filtering performance of the AWR pattern is now evaluated experimentally. The evaluation relies on measurements performed by means of a SLDV on a refined grid of points, out of which the desired electrode pattern is sampled. This, results in a configuration

where the sensor output is computed as the weighted sum of the response recorded at selected measurements points, with weights defined by the AWR shape function, Equation 65. This approach allows a great flexibility in testing various electrode patterns, without the need to physically manufacture the transducer. The procedure is in all similar to the one presented for the evaluation of the numerical performance of the device.

5.4.1 Experimental Setup

In order to perform the above-mentioned test, some adjustments to the AWR presented in Section 5.3 are required. In particular, (i) SLDV spatial resolution between adjacent grid points, and (ii) sensor patterning resolution both lead to consider performing the test at a lower frequency range, compatible with SLDV operations. In addition, the maximum sampling frequency associated with the SLDV acquisition system is 2.56 MHz, which is well below the required one for a transducer with a frequency content of the order of 50 MHz.

In addition, due to SLDV limited maximum allowable grid size (practically about 40k points), it is not possible to perform a full field scan and evaluate the sensor response by weighting the wave propagation field with the patterning value. Instead, the scan is performed along a single line, which is transformed into a full wave propagation field by radial replication, and interpolation on a structured grid suitable for pattern weighting in a subsequent post-processing stage. A high level overview of the process is presented in Figure 82.

For the reasons above, the frequency of 100 kHz is chosen as a reference, and the hosting medium is set to be an aluminum plate of dimension 1.5 m x 0.7 m x 1 mm. The sensor interrogation signal is provided by a 4-cycle Hanning-windowed tone burst, by means of a 7 mm square PZT transducer bonded to the plate, Figure 83(b). The PZT is driven by a E&I 1040L power amplifier, while the signal is generated by a Agilent 33220A function generator.

Given this frequency range, Lamb waves are excited in the hosting medium. In particular, the A_0 Lamb mode is targeted. Even though Lamb waves are know to be dispersive, the filtering properties of the patterning are preserved.

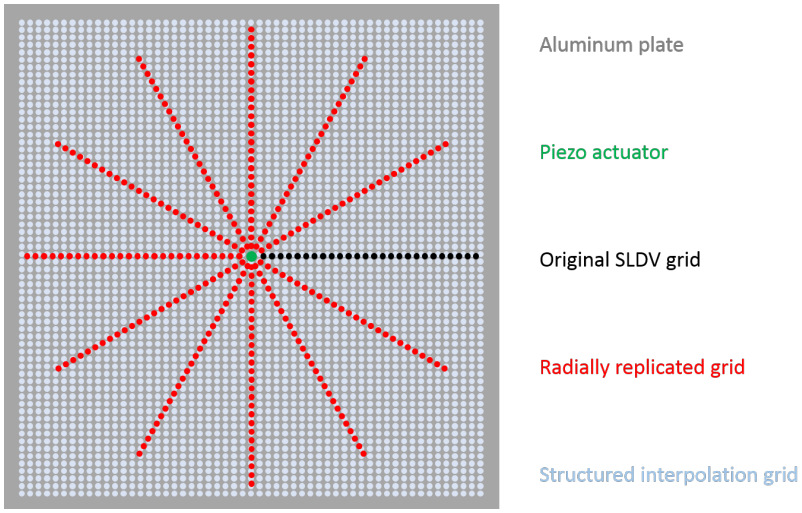

Figure 82: High level overview of the data acquisition and interpolation process for the verification of multi-band filtering properties associated with the AWR patterning. Grid-points are coarsened for visualization purposes.

The response is recorded over a single line extending horizontally from the excitation point for 450 mm, Figure 83(a). Wavefield measurements over the scan line are performed by repeating the excitation pulse with a repetition rate of 10 Hz, which is used as a trigger, so that phase information is maintained at each measurement point, and the recorded wavefield appears as simultaneously captured at all points. The response is then replicated radially and interpolated over a fine grid of M x M points, with $M = 1024$. Sampling of the measurement points is simply performed by evaluating the sensor shape function $f(\boldsymbol{x_j})$ at grid point $\boldsymbol{x}_j$.

The AWR response is computed through the following relation

$$TH_{AWR}(t) = \sum_{j=1}^{M^2} f(\boldsymbol{x}_j) u(\boldsymbol{x}_j, t) \tag{95}$$

where the weights $f(\boldsymbol{x}_j)$ are calculated based on the threshold AWR shape.

Given the excitation input bandwidth characteristics, frequency peaks at 85, 100, and 115 kHz are chosen at -30°, 90°, and 210° wavenumber domain directions. The resulting AWR electrode pattern is reported in Figure 84.

Figure 85 shows full field time snapshots of the interpolated wave propagation field that is used to interrogate the device. The filtering performance results presented in Figure 86 demonstrate the capability of the pattern to act as a tri-band spatial filter. Table 7 presents

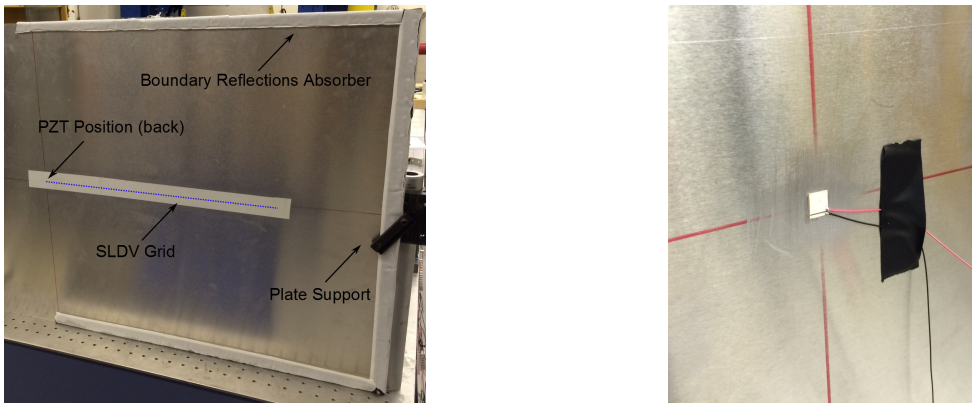

(a) Plate setup

(b) PZT close-up

Figure 83: Experimental setup.

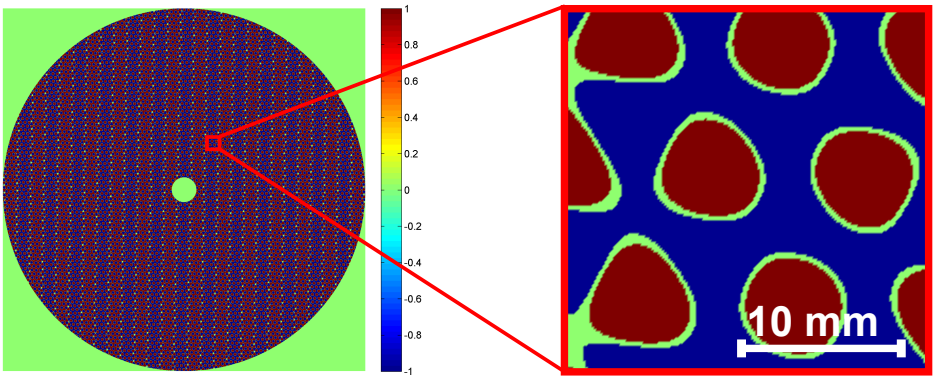

Figure 84: Sensor shape in the spatial domain. Outer radial dimension: 450 mm, inner radial dimension: 30 mm. Threshold $\eta = 0.07$.

quantitative results on the peak detection performance of the AWR. As it can be seen, the patterning is shown to able to filter the input signal quite sharply around the expected frequencies, with a maximum error of only 1.1%.

These results validate the AWR multi-band filtering properties and poses a fundamental milestone for future investigations upon the device. It is worth noting that this "low-frequency" AWR is not feasible to manufacture, nor it would have any practical application for strain sensing. It has been presented here solely for sake of experimental verification of multi-band filtering properties, for which it has proved to perform adequately.

Table 7: AWR multi-band filtering properties: peak frequencies comparison with design.

Design frequency [kHz]	AWR peak frequency [kHz]	Error [%]
85	84.06	1.10
100	99.38	0.62
115	114.40	0.60

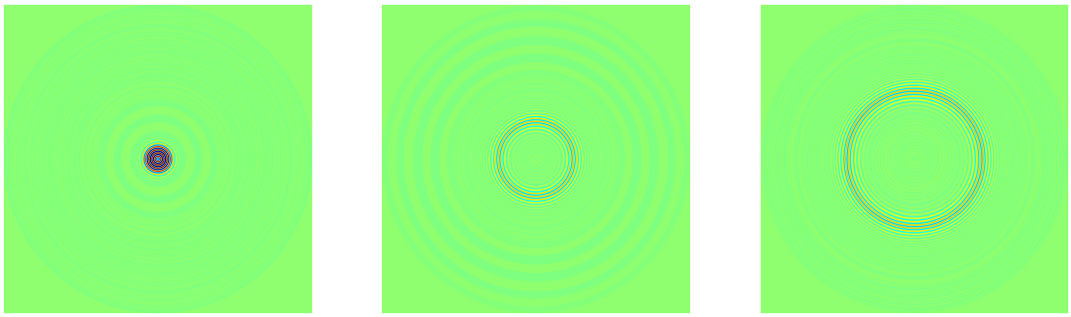

(a) $t = 50\,\mu s$ (b) $t = 100\,\mu s$ (c) $t = 150\,\mu s$

Figure 85: Full wave propagation field snapshots reconstructed from the experimental scan performed with an SLDV.

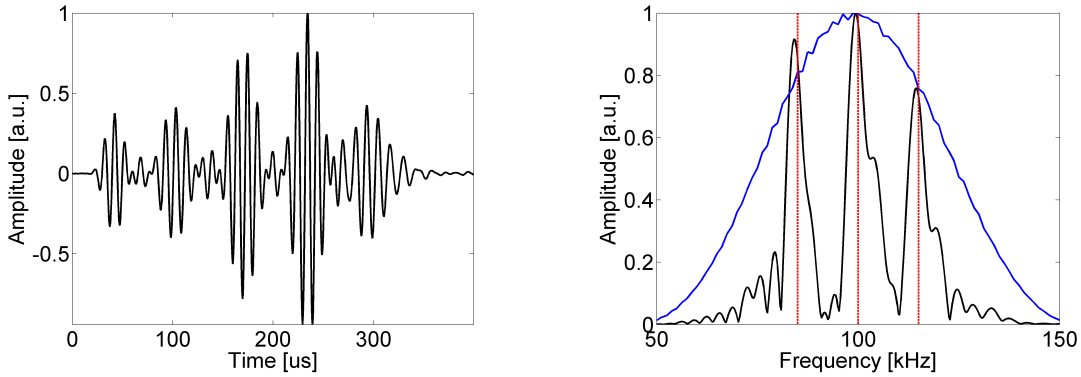

(a) AWR time domain response (b) AWR frequency domain response

Figure 86: Acoustic wave rosette output signal. (a) Time domain signal (TH_{AWR}). (b) Frequency domain. Solid blue line: excitation input. Solid black line: AWR response. Red dashed lines: design peak frequencies associated with the AWR pattern.

5.5 Paths to AWR Fabrication

For envisioned real-life applications, AWRs transducers must have a footprint that is reduced to few mm, in order to comply with the restrictions presented in Section 5.2.1. Thus,

as stated before, the AWR design suggest applications that exploit Surface Acoustic Waves (SAWs) at a device level, i.e. a suitable frequency range that would allow SAWs propagation based on the device thickness is foreseen.

The manufacturing procedure for SAW sensors is mainly device and application specific [37]. In general, issues such as substrate selection, transducer geometry and thin film deposition technique all need to be considered. In addition, it is advisable to take into account also the final operational environment of the device since it might have an important influence from a material selection standpoint.

5.5.1 Typical SAW Architectures

SAW devices typically utilize interdigitated transducers (IDTs) that are fabricated onto a substrate to generate Rayleigh waves. The wave velocity is determined by the substrate material and, in the case of anisotropic substrates, the cut of the crystal [37]. The energy of SAWs is confined to a zone close to the surface [3], and this makes them the most sensitive among acoustic devices.

SAW devices are presently fabricated using processes that have been primarily developed for Integrated Circuits (IC) technology in the microelectronics industry, and the two manufacturing architectures that are usually adopted are: (i) bulk piezoelectric (standard), and (ii) silicon integration (under development). For the standard bulk piezoelectric architecture, Figure 87(b), materials that offer a compromise between a high electromechanical coupling and low temperature coefficient are preferred, Quartz being the dominant material at the moment [55]. However, Quartz is expensive and, most importantly, difficult to deposit on substrates such as Silicon, thus limiting its applications, particularly in microelectronics. Other examples of piezoelectric substrates are Lithium Niobate ($LiNbO_3$), and Lithium Tantalate ($LiTaO_3$). For the Si integration architecture, Figure 87(a), a piezoelectric Zinc Oxide (ZnO) layer performs the coupling of the acoustic waves. Silicon di-Oxide (SiO_2) thin layers act as an adequate electric insulating layer as well as providing a suitable substrate for the growth of high-quality ZnO films [10].

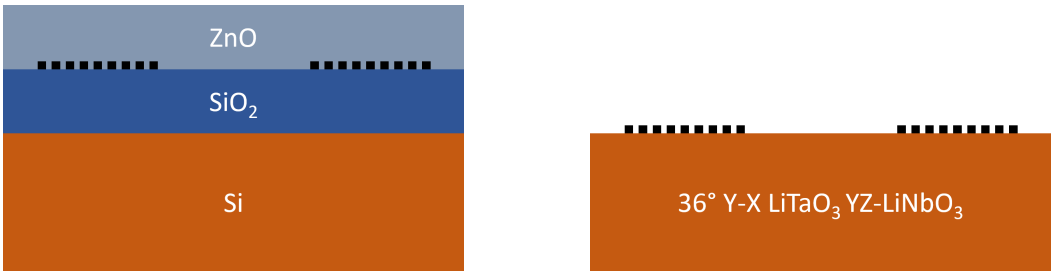

(a) Bulk piezoelectric architecture

(b) *Si* integration architecture

Figure 87: Schemes of typical manufacturing architectures for SAW devices. Thicknesses are not on scale.

In recent years there has been an increased interest in ZnO thin films in terms of potential applications in transducers and sensors. Above others, an important application using ZnO materials was the fabrication of ultra-high frequency SAW devices for communication applications, which makes use of the piezoelectric properties of this material to generate and detect SAW signals [31]. Other thin films, such as Aluminum Nitride (AlN), have been reported due to their low temperature coefficient and high electromechanical coupling [82].

To realize the interdigital structures on the surface of the acoustic device for either the *Si* integration or bulk piezoelectric substrates, commonly used planar fabrication processes such as etching and liftoff methods are used [37]. The etching procedure involves the selective etching away of unwanted metal patterns after a development step which removes either exposed or unexposed photoresist from the surface of the substrate. A positive mask is used in the photolithography step and the subsequent removal of unwanted metal is dependent upon the type of photoresist used, whether positive or negative.

5.5.2 AWRs Envisioned Architecture

Of the two architectures presented above, the bulk piezoelectric one is impractical for AWR manufacturing. Its criticality resides in the high anisotropy levels of the totality of the available piezoelectric substrates, that usually come under the form of crystals. Due to this fact, the retrieval of frequency shifts from radial wavenumber ones presents difficulties related to non-circular iso-frequency contours. The theory presented in Section 5.3 was formulated for substrates for which frequency can be easily mapped to radial wavenumbers

being iso-frequency contours circles in the bi-dimensional wavenumber domain, which is not the case here.

High substrate anisotropy can be mitigated by adopting the Si integration technique, but it still retains a weak level of anisotropy, Figure 88. More interestingly, there exist a number of commercially available substrates that are isotropic in nature. The most prominent example is fused silica which is a noncrystalline, glass form of silicon dioxide. As it is typical for glasses, it lacks long range order in its atomic structure. Its highly cross linked three dimensional structure gives rise to its high use temperature and low thermal expansion coefficient, characteristics that make its use ideal as a substrate of choice for the fabrication of envisioned AWR devices. In addition to its isotropic nature, fused silica represents an idea substrate for growing ZnO thin layers with good piezoelectric properties and a high electro-mechanical coupling coefficient. It can be grown in thin film form by RF magnetron sputtering (which is very attractive due to the simplicity of the process and relatively low equipment cost) on a variety of substrates, including silicon and fused silica. Other advantages of using ZnO films include (i) easy integration with micro-sensors and micro-actuators on the same substrate, (ii) excellent bonding with various substrate materials, (iii) high temperature stability [43], (iv) and low cost of deposition. For these combined reasons, ZnO represents the piezoelectric layer of choice for a possible future fabrication of AWR devices.

5.5.3 Electrode Patch Linking

One last problem that needs to be discussed is how to link together the various patches that constitute the AWR electrodes. For application like the FSAT presented in Chapter 3 the electrode patches were very limited in number due to the fact that the material layout (for a single spiral branch) in the wavenumber domain was continuous. In that case, manual linking through AutoCAD was implemented. Unfortunately, this is not the case for the AWR, where thousands of patches that constitute the electrode need to be linked together. This cannot be done by inspection and an automatic patch linking procedure must be adopted, as outlined below. The goal is to be able to automatically handle the electrical

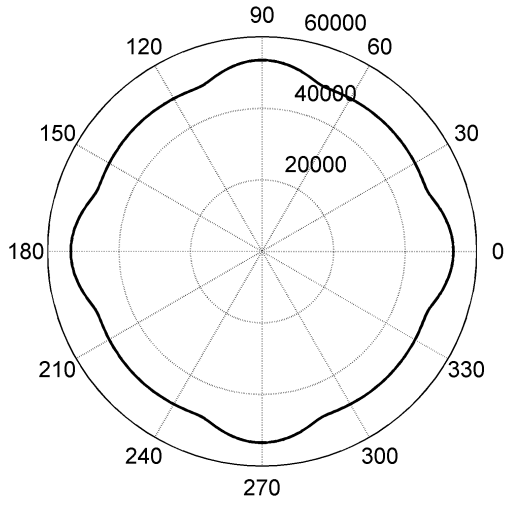

Figure 88: Example of dispersion curve in terms of group velocity [m/s] for $< 100 >$ Silicon at a frequency of 250 MHz.

connections between single patches. The approach followed is to treat all the patches belonging to a single electrode as a logical image, i.e. a bi-dimensional matrix made of 1s where the electrode is present and 0s where there is no electrode.

The connection procedure can be implemented easily by exploiting the MATLAB morphological image processing routines. The fundamental steps of the algorithm are the following:

- Patches belonging to a single electrode are converted to a logical image;
- Patch automatic recognition is implemented on the logical image;
- Geodesic Recursive Connection (GRC) is then implemented until only one patch remains, with a connection ligament thickness arbitrarily chosen in terms of pixels.

As a simple example, the procedure is firstly applied to a tri-patched image, Figure 89(a), so that visual inspection of the automatically generated connections (or ligaments) can be performed easily. Figure 89(b) shows the processed image with the patch connections in place.

(a) (b)

Figure 89: Application of the GRC algorithm to a tri-patched image. (a) Original image. (b) Processed image. Ligaments width is set to 3 px.

A second example is reported in Figure 90 where an AWR-like pattern with 26 patches is used as input for the GRC method.

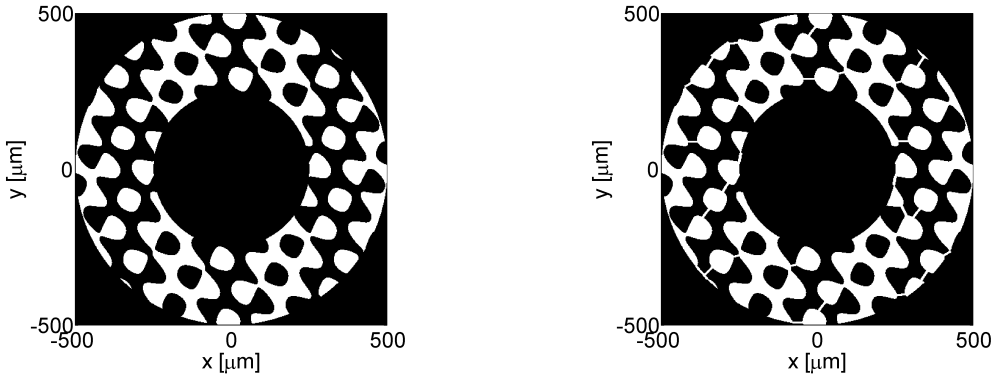

(a) (b)

Figure 90: Application of the geodesic recursive connection algorithm to an AWR-like pattern. (a) Original image. (b) Processed image. Ligaments width is set to 3 px.

One question that might arise is whether or not the initial filtering properties of the electrode are maintained, or, in other words, if the ligaments lead to a significant distortion of the overall electrode pattern. To this aim, a check on the wavenumber distortion caused by the ligaments is performed. The approach relies on the computation of the Structural Similarity Index (SSIM) on the original and processed images (or, better, on their 2D FT) to check whether or not the distortion due to the presence of the ligaments is acceptable. The SSIM is a point-wise index that can assume values from 0 to 1, where 1 means point-wise

perfect match between two images. The SSIM result for the wavenumber region of interest on the reduced AWR-like pattern is presented in Figure 91. The minimum SSIM value in the regions of interest, i.e. in correspondence of the wavenumer peaks, is 0.9463. This sets the distortion associated with the presence of the ligaments approximately to 5%. Further investigations are envisioned as part of future studies on the subject.

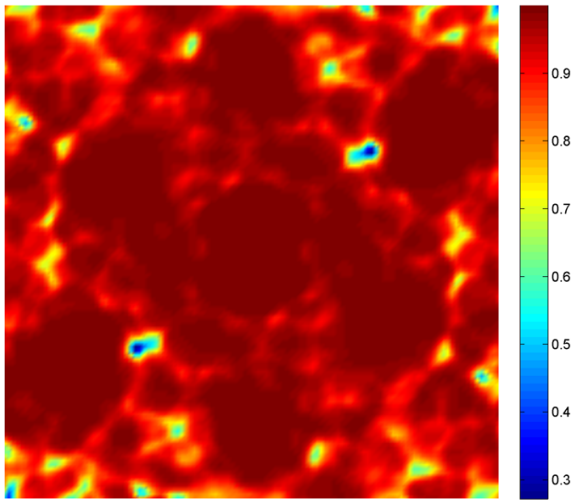

Figure 91: Wavenumber domain SSIM between the AWR-like patterns of Figure 90(a) and Figure 90(b).

In summary, the GRC method can be confidently applied to connect an arbitrary number of patches without problem. The main drawback of the technique is that automatic handling of connections is impossible in presence of a double electrode configuration, such as the one found in actual AWR schemes. For a lack of a better solution, this problem is deferred to the microfabrication procedure, where a split electrode configuration is envisioned.

5.5.4 Envisioned Microfabrication Procedure for AWRs

Given the considerations presented in Section 5.5.2 and Section 5.5.3, a possible process flow for the manufacturing of AWRs is presented in Figure 92, where a high level overview of the steps that need to be taken is presented. The critical steps of the process flow are represented by the deposition of the ZnO piezoelectric layer, which would require big zinc targets (6 in diameter) for the deposition through RF magnetron sputtering [10] or layers of

the order of few μm, which represent typical thicknesses that can be found in literature [22].

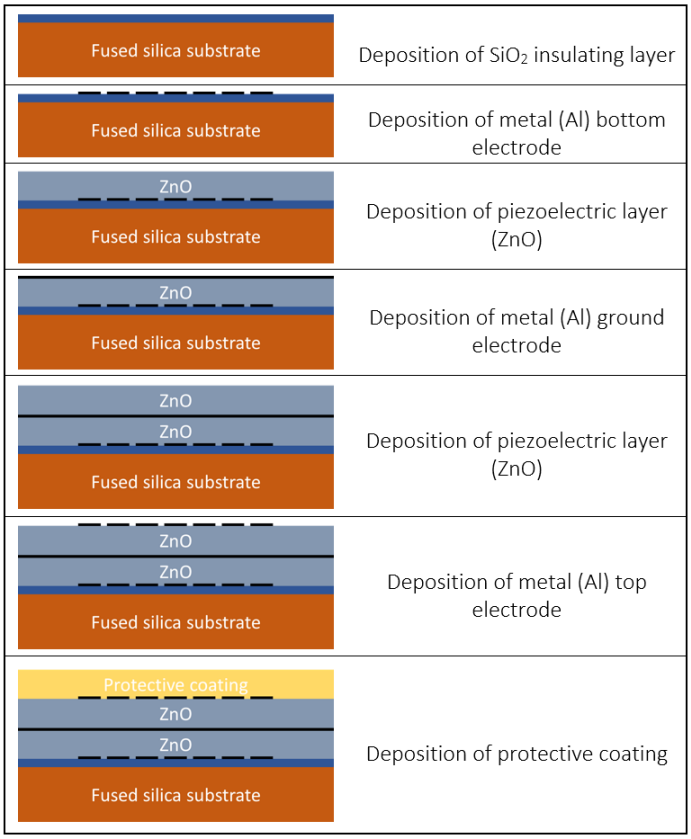

Figure 92: High level overview of a possible fabrication procedure for AWRs.

5.6 Conclusions

In this chapter, the concept of sensor design by assigning its electrode shape in the wavenumber domain has been extended to strain sensing. To this aim, the design of a co-located strain sensor, termed Acoustic Wave Rosette, has been developed analytically, numerically, and experimentally. The transducer is characterized by an internal patterning whose wavenumber representation features maxima at specific directions. The resulting sensing pattern leads to a multi-band spatial filter suitable for strain sensing applications.

In the next chapter, the wavenumber-based design procedure will be tailored to the study of a passive impact localization device. To this aim, analytical/numerical and experimental studies will be conducted to assess the device capabilities and limits. Envisioned applications for the proposed transducer are those that involve acoustic events (i.e. impacts) with limited

frequency bandwidth excitation, for which FSATs design principles cannot be applied due to constraints on the spatial dimensions of the device.

CHAPTER VI

ELECTRODE PATTERNING FOR IMPACT DETECTION: THE IMPACT DIRECTIONALITY REVEALER

6.1 Overview

In this chapter an approach based on the employment of the wavenumber design technique detailed in Chapter 2 is proposed for passive impact direction determination. The ability to locate damage or impacts in structural materials with waveguide geometries (plates, rods, pipes, etc) is one of the attractions of GWs-SHM. Damage location can be achieved by either an "active-passive" approach or by a "passive-only" approach. In the former, diffractions of piezoelectrically actuated waves can be used to locate pre-existing damages [84, 54, 28, 49], while in the latter, growing damage or sudden impacts can be located by monitoring acoustic emissions. Traditionally, damage or impact location is based on Time-Of-Flight (TOF) triangulation of wave measurements taken at multiple receiving points.

The concept presented herein contributes to extend the "passive-only" damage localization approach by taking advantage of electrode patterning to reduce hardware requirements to a minimum. Envisioned applications are those that involve sensing of acoustic events (i.e. impacts) with limited frequency bandwidth, for which conventional FSATs fall short in their frequency-directionality mapping. In those bands, the design of effective spiral FSATs is particularly limited because an effective frequency beam-steering would lead to excessive dimension given the wavelengths that are typical for the A_0 target mode.

To overcome this, an approach that exploits wave relative amplitudes at two pilot frequencies is proposed. The goal is to identify a shape of the device to enable the determination of the direction of a traveling wave generated by an impact-like acoustic event. The resulting device, termed Impact Directionality Revealer (IDR), is a device that is able to determine the direction of an impact relying on a two-point inspection of the spectrum of its sensed voltage. Numerical and experimental validation of the concept are then presented

to demonstrate the principles of operation associated with the device. The methodology discussed herein is generally applicable to anisotropic and geometrically complex structures, where conventional approaches, such as time-of-flight estimations, are challenging due to direction dependent wave velocity, and material attenuation.

6.2 "Low-frequency" FSAT Drawbacks

The main drawback of spiral FSATs is that they are characterized by relatively high operational frequencies, typically ranging from 50 kHz to 350 kHz, in order to keep the overall dimension of the device acceptable, which is dictated by the wavelength guided by the structure, being A_0 the typical design wave mode of choice. This makes the device difficult to employ in passive impact detection schemes, due to the limited frequency content of impact events.

For high speed ballistic events, the impact duration time is of the order of few microseconds [80], which translates in a frequency bandwidth of the order of few tens of kHz. Within this frequency band, the design of a spiral FSAT device able to determine the Direction of Arrival (DOA) of a wave packet presents a directionality-frequency mapping that is of limited practical use. As an example, Figure 93(a) reports a spiral FSAT design with a frequency bandwidth going from 10 kHz to 30 kHz and a radius $a = 25$ mm. The corresponding directionality-frequency mapping is reported in Figure 93(b).

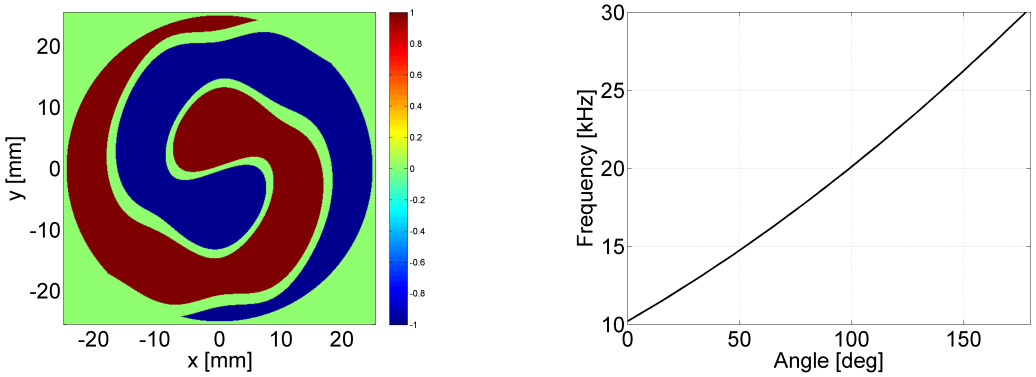

(a) (b)

Figure 93: (a) Low-frequency spiral FSAT example. Design bandwidth: $10 - 30$ kHz. Hosting medium is a 0.81 mm thick aluminum plate. (b) Corresponding directionality-frequency mapping.

As it can be seen, the material distribution in the spatial domain highlight the long wavelengths associated with the A_0 mode in the frequency band. Moreover, it can be observed from the directionality-frequency mapping how tight the mapping is, spanning only 20 kHz. Figure 94 shows device directionality plots for the frequencies of 15 kHz and 30 kHz. If for the 30 kHz case (Figure 94(b)) the directionality is somewhat preserved, this is not the case for 15 kHz (Figure 94(a)), for which the directionality maximum spans an azimuthal region that goes from 30° to 60°. The degradation of the directionality performance of the device is evident and this directly affects its DOA estimation performance of the device. For these reasons, FSAT performances at low frequencies would be poor, and the problem of impact detection with limited bandwidth acoustic events is now tackled.

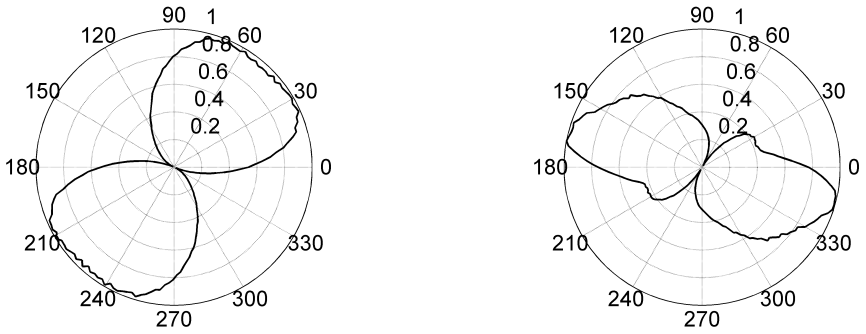

(a) 15 kHz

(b) 30 kHz

Figure 94: Example of device directionality. Radial scale is arbitrary.

6.3 Impact Directionality Revealer Principles of Operation

The idea behind this new transducer design stems from the same considerations at the base of the FSAT design [74], along with the use of wave amplitude directional properties. Recalling Equation (11), the sensor's response amplitude in the presence of a planar wave can be expressed in terms of a frequency-dependent sensitivity factor, $S(\omega)$, multiplied by the amplitude of the surface strain

$$V(\omega) = S(\omega, \vartheta)\varepsilon_{1'1'}(\omega) \tag{96}$$

The sensitivity factor was decomposed in Section 2.2.2 into two terms

$$S(\omega, \vartheta) = \mathcal{H}(\vartheta)\mathcal{D}(\boldsymbol{k}(\omega), \vartheta) \tag{97}$$

The quantity $\mathcal{H}(\vartheta)$ represents the material-related directionality, while $\mathcal{D}(\omega, \vartheta)$ represents the shape-related directionality. For this analysis, the material-related directionality is assumed constant. This stems from the thought of utilizing PVDF films as the choice material for the envisioned transducer, which does not exhibit anisotropy at the frequency ranges under consideration [78].

As seen in the previous section, continuous beam steering between two angles that define an angular sector (which was the idea at the foundation of the spiral design) would lead to a device with poor directionality performances. To cope with this, information deriving from the wave amplitude is factored into the design procedure. According to Equation (96), the voltage absolute amplitude is determined by $\varepsilon_{1'1'}$, which depends on the energy associated with the impact event, which, in turn, is unknown. Thus, in order to be able to exploit amplitude information, wave amplitude at two different frequencies have to be considered. It is shown now how the ratio of the amplitude between two "pilot" frequencies can be modulated based on the wave direction of arrival. This operation is performed by mapping the amplitude ratio to the directionality ratio, which can be determined by assigning the shape of the transducer in the wavenumber domain through the function $\mathcal{D}(\boldsymbol{k}(\omega), \vartheta)$.

A proof by construction is now presented. To this aim, a three-channels device is considered. The first two channels (Channel A and Channel B), which can be seen as the equivalent of positive and negative electrode of the spiral FSAT design, feature a known azimuthal variation of the function $\mathcal{D}(k(\omega), \vartheta)$ such that, for two non-coincident frequencies, namely ω_1 and ω_2, the following relationships are satisfied

$$\begin{aligned} \mathcal{D}_{AB}(k(\omega_1), \vartheta) &\neq 0 \quad \forall\, \vartheta \\ \mathcal{D}_{AB}(k(\omega_2), \vartheta) &\neq 0 \quad \forall\, \vartheta, \end{aligned} \tag{98}$$

where the subscript $_{AB}$ is used to highlight that the geometric directionality function is associated with the Channels A and B.

An effective wavenumber configuration that fulfills the relations of Equation (98) is that

of a distribution of material featuring two azimuthal-wise peaks with a double ring arrangement. Figure 95 shows a schematic of the configuration, where the amplitude variation of the peaks is represented by a changing thickness along the line.

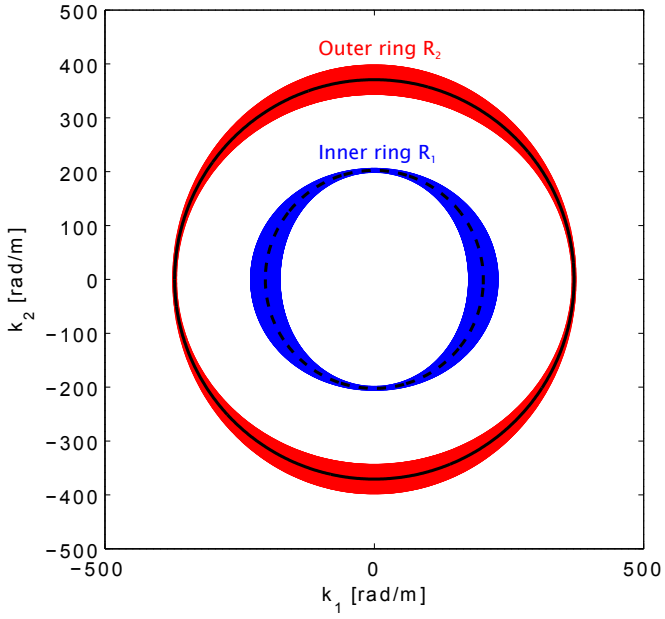

Figure 95: Schematic of double ring material arrangement in the wavenumber domain. Black solid line: iso-frequency circle corresponding to the outer ring material distribution. Black dashed line: iso-frequency circle corresponding to the inner ring material distribution.

The inner ring (R_1, blue line) features the following azimuthal amplitude distribution

$$A^{R_1}(k(\omega_1)) = 1 + \left| \frac{1}{2}\left(1 - \cos(2\vartheta + \pi)\right) \right| \tag{99}$$

where k_0 and ϑ represent radial and azimuthal wavenumber components, respectively. $A^{R_1}(k_0(\omega_1))$ presents the maximum amplitude at $\vartheta = 0$ and $\vartheta = \pi$.

The outer ring (R_2, red line) features the following azimuthal amplitude distribution

$$A^{R_2}(k(\omega_2)) = 1 + \left| \frac{1}{2}\left(1 - \cos(2\vartheta)\right) \right| \tag{100}$$

and presents the maximum amplitude at $\vartheta = \frac{\pi}{2}$ and $\vartheta = \frac{3}{2}\pi$.

In addition to Channels A and B, a third (reference) channel featuring $\mathcal{D}_{REF}(k(\omega), \vartheta) = 1$ (i.e. its shape is a point or, more practically, a circle in the spatial domain) is considered. Provided that the incoming wave packet has a non-zero frequency content at the frequencies

ω_1 and ω_2, the device will always display a non-zero voltage reading for those two frequencies when interrogated by a traveling wave. In particular, the voltage sensed by Channel A and B, respectively at frequencies ω_1 and ω_2 can be written as

$$\begin{aligned} V(\omega_1) &= \mathcal{D}_{AB}(\omega_1, \vartheta)\varepsilon_{1'1'}(\omega_1) \\ V(\omega_2) &= \mathcal{D}_{AB}(\omega_2, \vartheta)\varepsilon_{1'1'}(\omega_2) \end{aligned} \tag{101}$$

where $\varepsilon_{1'1'}(\omega)$ is the amplitude of the strain.

In addition to those of Equation (101), the following relations can be written for the reference channel response at the same selected frequencies

$$\begin{aligned} V_{REF}(\omega_1) &= \varepsilon_{1'1'}(\omega_1) \\ V_{REF}(\omega_2) &= \varepsilon_{1'1'}(\omega_2). \end{aligned} \tag{102}$$

Since the amplitude of the sensed voltages in Equation (101) and Equation (102) inherently depends on the amplitude of the strain, voltage amplitude ratios instead of absolute values are considered

$$\begin{aligned} \frac{V(\omega_2)}{V(\omega_1)} &= \frac{\mathcal{D}_{AB}(\omega_2, \vartheta)}{\mathcal{D}_{AB}(\omega_1, \vartheta)} \frac{\varepsilon_{1'1'}(\omega_2)}{\varepsilon_{1'1'}(\omega_1)} \\ \frac{V_{REF}(\omega_2)}{V_{REF}(\omega_1)} &= \frac{\varepsilon_{1'1'}(\omega_2)}{\varepsilon_{1'1'}(\omega_1)}. \end{aligned} \tag{103}$$

Combining the two equalities of Equation (103) and solving for the directionality ratio yields

$$\frac{\mathcal{D}_{AB}(\omega_2, \vartheta)}{\mathcal{D}_{AB}(\omega_1, \vartheta)} = \frac{V(\omega_2)}{V(\omega_1)} \frac{V_{REF}(\omega_1)}{V_{REF}(\omega_2)}. \tag{104}$$

The operation reported in Equation (104) is always allowed, since the function $\mathcal{D}_{AB}(k(\omega), \vartheta)$ has a non-zero value at both ω_1 and ω_2, and for all the ϑ values. Equation (104) represents the relation that is at the foundation of the design of a device, termed as Impact Directionality Revealer (IDR), capable of determining the Direction of Arrival (DOA) of acoustic events simply relying on the geometrical shape of its electrodes.

For the double ring arrangement, it can be easily verified that the directionality ratio $\mathcal{D}_{AB}(\omega_2, \vartheta)/\mathcal{D}_{AB}(\omega_1, \vartheta)$ of Euqation (104) corresponds to the material distribution ratio A^{R2}/A^{R1}. The ratio is reported in Figure 96(a). It is worth noting that such a device intrinsically presents a four-folded directionality indetermination. In particular, 180° and

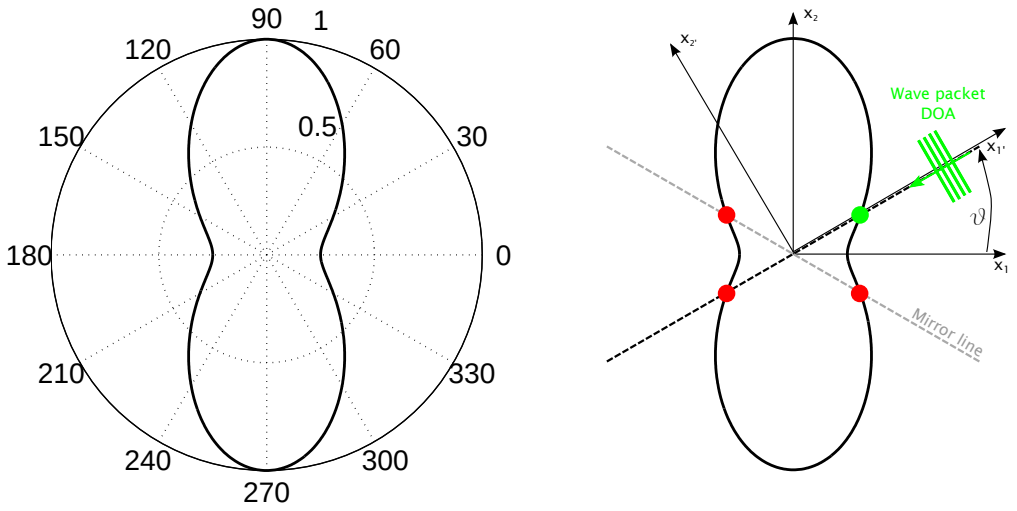

(a) (b)

Figure 96: (a) Directionality ratio $\mathcal{D}_{AB}(\omega_2, \vartheta)/\mathcal{D}_{AB}(\omega_1, \vartheta)$ (b) Illustration of IDR directionality indetermination.

mirror indetermination are outlined in Figure 96(b); while the former is always present, the latter vanishes for arrival directions of $0 + m\frac{\pi}{2}$, where m is integer-valued.

Figure 96 also highlights another important feature: the directionality ratio at two selected frequencies (or, more rigorously, wavenumbers) is monotonically increasing from 0° to 90°, such that no superior levels of directionality indetermination arise. Also, as a reminder, frequencies must be selected such that the impact signal has a non-null frequency content, as presented in Figure 97, otherwise the directionality properties of the device are compromised.

6.4 Analysis of an IDR Concept for Isotropic Plates

Dispersion relations of Lamb waves in isotropic plates are considered in the following section due to their extensive use in damage detection. In particular, the IDR target wave mode is supposed to be A_0.

6.4.1 Design

The pilot frequencies selected for the double ring configuration are 10 kHz and 33 kHz for operations on a 1 mm thick aluminum plate. Figure 98(a) reports the wavenumber domain

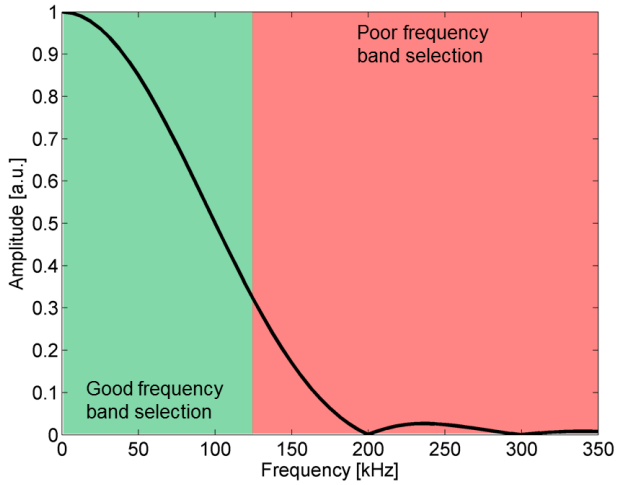

Figure 97: IDR frequency selection choices. Reported spectrum corresponds to a 10 μs long, (1 − cos) finite duration impulse function.

representation of the device. As it can be seen, both rings are modulated around their pilot frequency by a Gaussian in order to avoid the inclusion of radial discontinuities in the spectrum.

The corresponding spatial arrangement of the two electrodes is retrieved by applying a bi-dimensional IFT according to Equation 16, with a successive three-level quantization that allows the device to be manufacturable. The result of the process is reported in Figure 98(b). The outer dimension is cut at a radius of 45 mm.

As for the case of the FSAT, this thresholding procedure, introduces a wavenumber distortion of the sensor shape. While for the FSAT this had a relative low impact on the overall transducer performance, this is not the case for the IDR. Threshold represents here a serious distortion of the wavenumber shape of the IDR, as depicted in Figure 99(a), where side lobes are visible. This must be taken into account when computing directionality ratios. As it can be seen from Figure 99(b), the threshold IDR still features an amplitude ratio that satisfies the relations of Equation (103), so the threshold double ring arrangement indeed is a good candidate for an IDR concept.

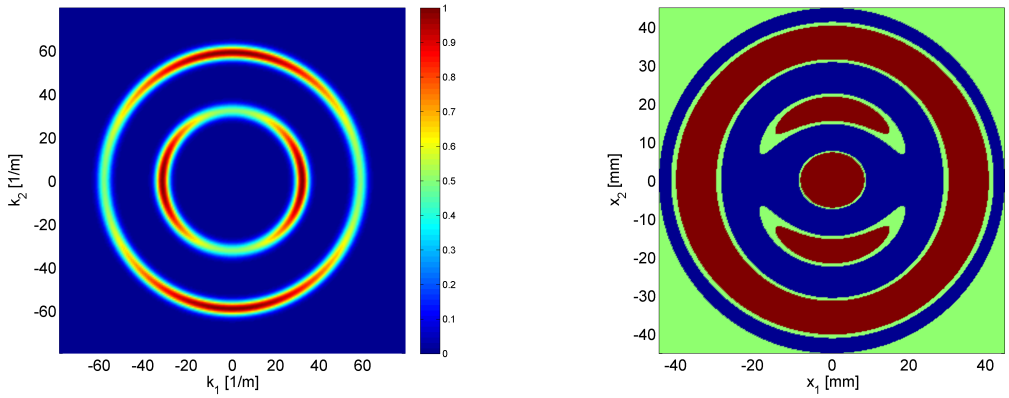

(a) (b)

Figure 98: IDR double ring arrangement of sensing material. (a) Wavenumber domain representation. (b) Spatial domain representation retrieved through bi-dimensional IFT and successive threshold of the electrodes (threshold level $\eta = 3\%$). Target hosting medium is a 1 mm thick aluminum plate.

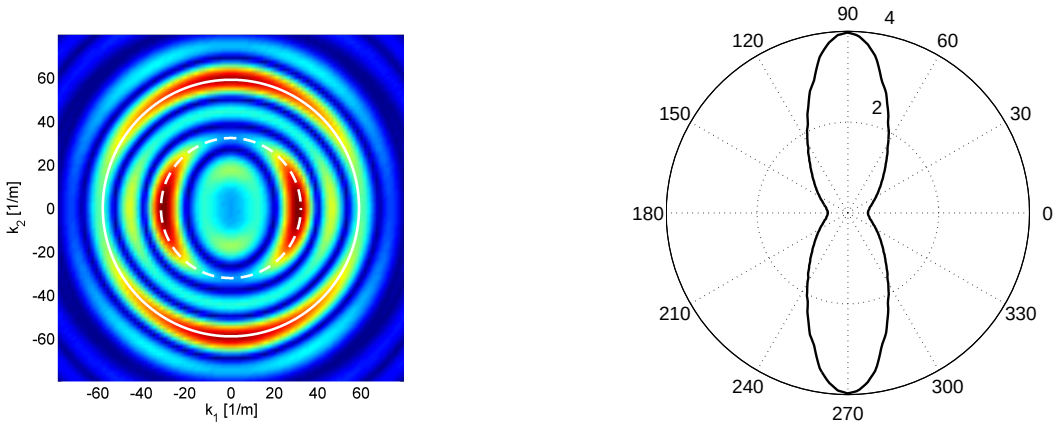

(a) (b)

Figure 99: (a) Wavenumber domain transformation of threshold IDR. Domain distortions are visible. Dashed white line: R_1 frequency. Solid white line: R_2 frequency. (b) Directionality ratio R_2/R_1.

6.4.2 Numerical Analysis

The performance of the IDR outlined in Section 6.4.1 is evaluated through numerical simulations that predict the wave propagation field generated by a point source. The objective is to test the performance of the device for different directions of incoming waves corresponding to an impulsive event applied to the test structure.

6.4.2.1 Simulation Approach

In the considered formulation, the plate response at location $\boldsymbol{x}$ due to a point source located at $\boldsymbol{x_s}$ is evaluated through a Green's function formalism [4]

$$u_3(\boldsymbol{x}, \omega) = g_0(\omega)\mathcal{G}(\boldsymbol{x}, \boldsymbol{x_s}, \omega) \tag{105}$$

where $u_3(\boldsymbol{x}, \omega)$ denotes the plate's out-of-plane displacement, while $g_0(\omega)$ is the amplitude of the excitation at frequency ω. The Green's function $\mathcal{G}$ is here approximated as [30]

$$\mathcal{G}(\boldsymbol{x}, \boldsymbol{x_s}, \omega) = j\pi^2 H_0^{(1)}(kr_s) \tag{106}$$

where $H_0^{(1)}$ is the Hankel function of the first kind and order 0, and $r_s = |\boldsymbol{x} - \boldsymbol{x_s}|$ is the distance of the considered point from the source. Also, k is the wavenumber of the considered wave mode (A_0 in this case), and it is related to frequency through the corresponding dispersion branch $k = k(\omega)$.

The simulation consider the configuration of Figure 100(a), where an aluminum plate of 1 mm thickness is excited by a 10 μs long, $(1 - \cos)$ like, finite duration impulse, whose time and frequency domains are represented in Figure 100(b).

The plate response is measured over a grid of M x M points, with M = 256. Sampling of the measurement points is simply performed by evaluating the sensor shape function $f(\boldsymbol{x}_j)$ at grid point $\boldsymbol{x}_j$, with a procedure analogous to the one presented in Section 5.4 for the AWR. The measurement grid and its IDR-sampled version are shown in Figure 101.

The response of the device is computed through a discretized version of Equation (16). In particular, let $u_3(\boldsymbol{x}_j, t)$ denote the response measured at location $\boldsymbol{x}_j$. Then the transducer response can be expressed as

$$U_3(t) = \sum_{j=1}^{M^2} f(\boldsymbol{x}_j) u_3(\boldsymbol{x}_j, t) \tag{107}$$

where the weights $f(\boldsymbol{x}_j)$ are calculated based on the threshold sensor. Responses at different DOA are evaluated by rotating the transducer orientation with respect to the source location, as represented in Figure 101(b) for the case of a 45° rotation, so that one single

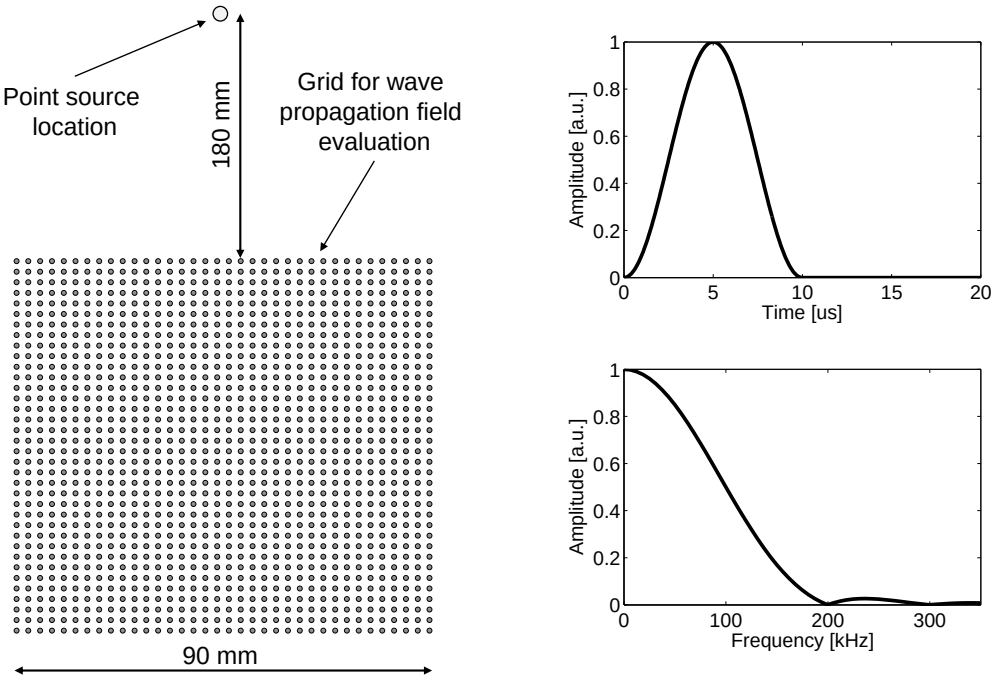

(a) (b)

Figure 100: (a) Reference simulation configuration (dimensions not on scale). (b) Finite duration impulse used as excitation signal.

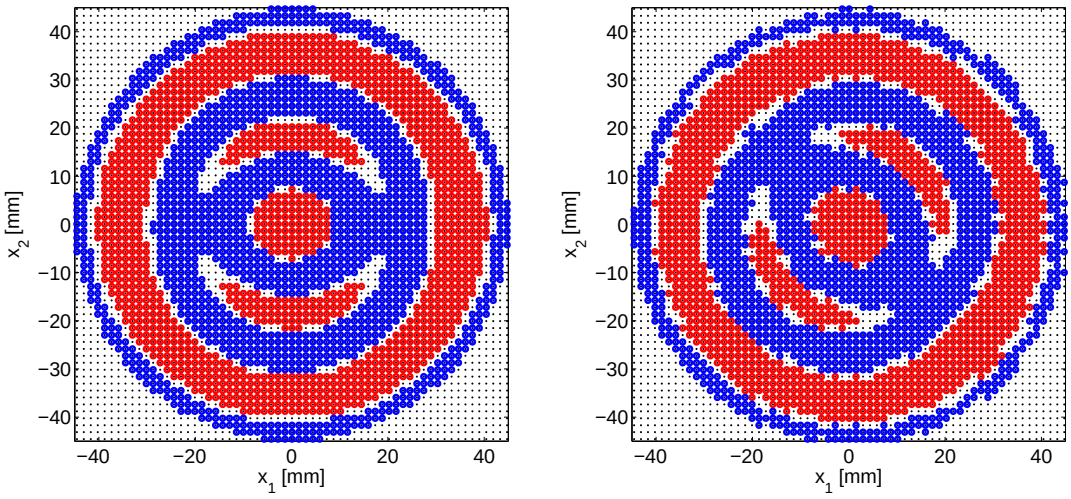

(a) (b)

Figure 101: Electrode weighting representation (grid has been coarsen for sake of presentation). Black dots: numerical grid. Blue circles: positive IDR electrode. Red circles: negative IDR electrode. (a) IDR oriented at 90° with respect to the impact source. (b) IDR oriented at 45° with respect to the impact source. The rotation is defined as positive if clock-wise.

simulation is required. Rotation is defined to be positive if clock-wise. The reference voltage V_{REF} and its spectrum are evaluated considering the signal average of the four central points of the grid (which correspond to the center of the device).

6.4.2.2 Results

The IDR response for a device rotation of 45° is presented in Figure 102. As it can be seen, the device acts as a spatial filter at the design frequencies, with the small discrepancies to be attributable to to the device mapping procedure that interpolates the electrode shape on the numerical grid. In order to retrieve the DOA of the simulated impact event, ratios of the reference and IDR-weighted signal are retrieved and processed according to the procedure outlined in Section 6.3. First, the time traces of the IDR and the reference channel, Figure 102(a), are used to retrieve the corresponding frequency spectra, Figure 102(b). From these, the voltage ratios $V(\omega_2)/V(\omega_1)$ and $V_{REF}(\omega_1)/V_{REF}(\omega_2)$ are retrieved. Then, Equation 104 is used to compute the directionality ratio associated with the wave packet under consideration. Its value is interpolated over the device azimuthal directionality function to retrieve the DOA of the wave packet.

Results are summarized in Figure 103 and Table 8. As it can be seen, the DOAs detected by the sensor are very close to those expected, with a maximum discrepancy of only 2°, excluding the 0° and 90° directions. These two directions are considered exceptions, since the IDR output is either non-existent, or undetermined, as seen Figure 103(a) and (d). As it can be seen in Figure 99(b), low sensitivity is indeed expected in those two cases, given the shape of the amplitude ratio function. This can be easily verified by looking at the derivative of the amplitude ratio, which approaches either zero or infinity for the two above-mentioned directions.

6.4.3 Testing

An experimental validation of the concept is now performed. In the experiments, the out-of-plane displacement is recorded by a Polytec PSV-400 SLDV over a grid of 160 x 160 measurement points covering a 90 x 90 mm area over a 0.81 mm thick aluminum plate. The response recorded at each point is weighted according to Equation (107), and combined with

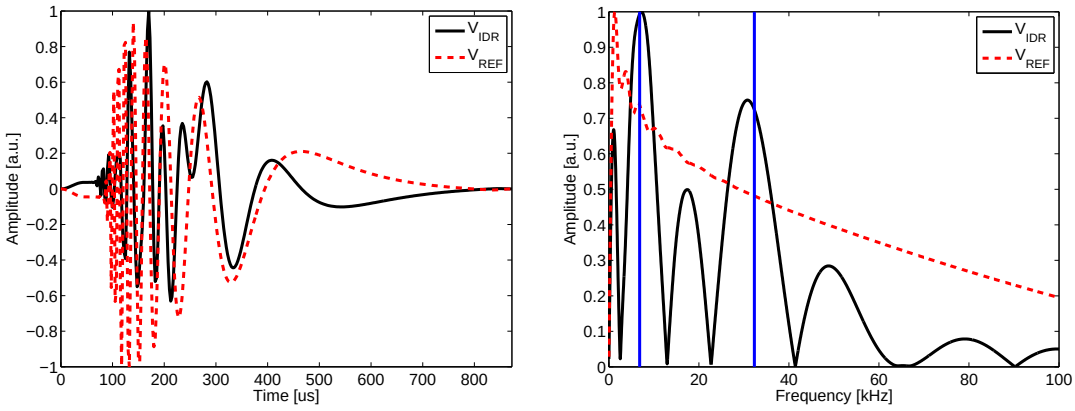

(a) (b)

Figure 102: IDR output signals for a 45° impact DOA. (a) Time domain signals. (b) Corresponding frequency spectra. Blue lines: pilot frequencies.

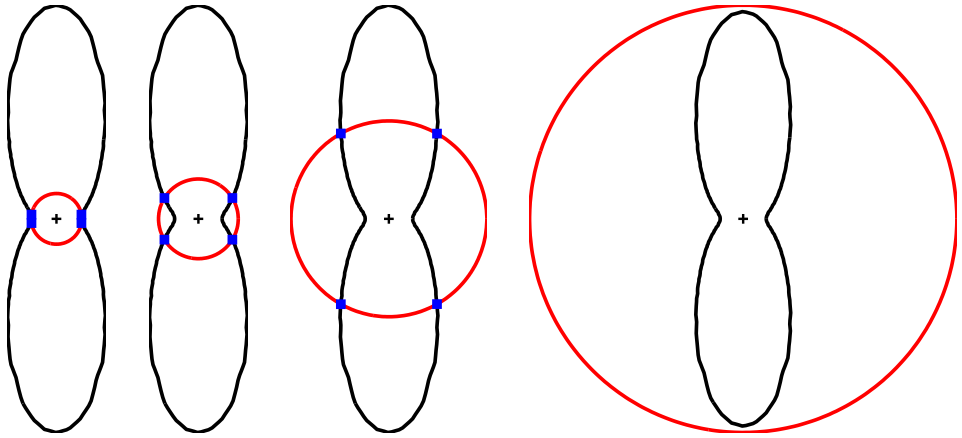

(a) 0° (b) 30° (c) 60° (d) 90°

Figure 103: Peaks ratio visualization for different impact DOA. Black curve: IDR peak ratio (A^{R_2}/A^{R_1}). Red circle: computed amplitude ratio. Blue squares: intersection points.

that of all other points to obtain the global response of the IDR. The weighting procedure is analogous to the one considered for the experimental analysis of the AWR described in Section 5.4.

A new IDR geometry is generated, specifically tailored to the 0.81 mm thick aluminum plate, with double ring frequencies set to 10 kHz and 30 kHz, respectively. The resulting electrode configuration is reported in Figure 104(a). The radial extension of the device is set to 45 mm, and the threshold is $\eta = 0.05$. The wavenumber configuration is tuned to the A_0 mode in the selected kHz range. The corresponding ratio of the double rings amplitude

Table 8: IDR numerical performace summary for different impact DOA. Estimates reported include spurious directions derived from its directionality indetermination.

IDR Rotation Angle	Actual Impact DOA	IDR Estimate DOA
0°	90°	NaN
15°	75°	±76.44° ± 103.58°
30°	60°	±60.58° ± 119.39°
45°	45°	±45.77° ± 134.38°
60°	30°	±31.49° ± 148.48°
75°	15°	±17.54° ± 162.56°
90°	0°	±9.57° ± 170.41°

is reported in Figure 104(b).

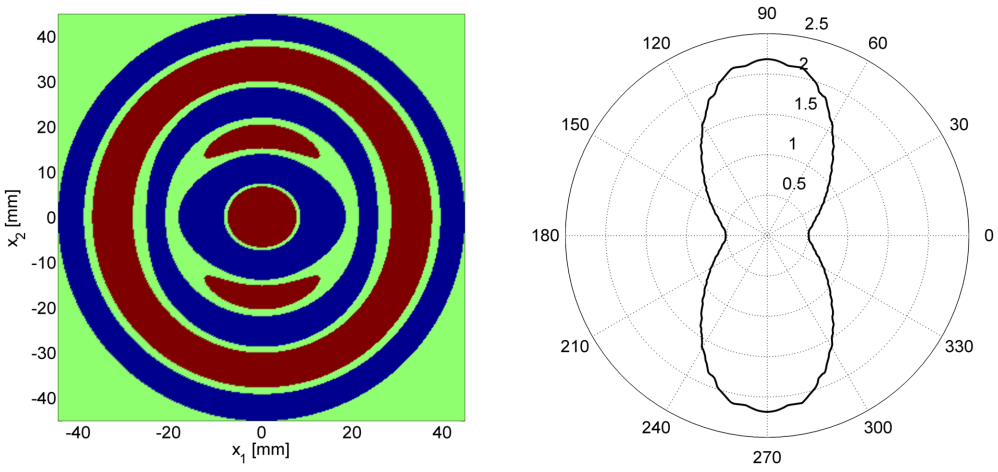

(a) (b)

Figure 104: IDR configuration for the 0.81 mm thick aluminum plate used in the experiments. (a) Electrode shape with double-ring frequencies set to 10 kHz and 30 kHz respectively. Threshold level $\eta = 0.05$. (b) Corresponding double ring amplitude ratio.

The tests are performed using a 15 mm x 0.9 mm round PZT disk to simulate the presence of an impact-like event. The disk is bonded to the plate at a distance of 250 mm from the center of the reconstructed IDR, and at an angle of 45° with respect to the x_1 (horizontal) direction. The PZT is driven by a high voltage rectangular pulse of 10 μs width, whose bandwidth is wide enough to excite the frequency range of interest ($<$ 50 kHz).

The excitation provided by the source was inspected beforehand by performing a preliminary SLDV acquisition at the center of the transducer. As it can be seen from Figure 105, the frequency range of interest shows good excitation levels, although, as expected, (i) the

spectral amplitude is not perfectly uniform, and (ii) the excitation authority below 8 kHz is greatly compromised.

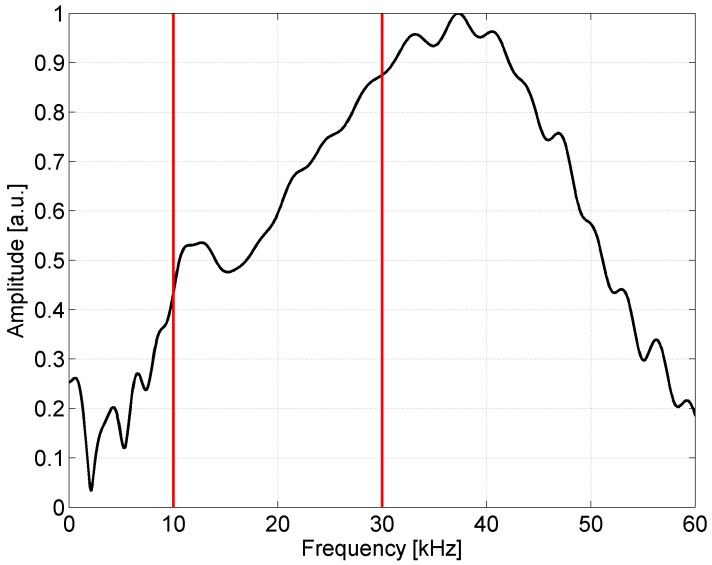

Figure 105: Frequency spectrum of the excitation provided by the PZT source used to simulate an impact damage. Red vertical lines: pilot frequencies for the IDR experimental configuration.

An example of the frequency outputs obtained from the synthesis of the IDR for the case of the simulated impact-like event forming a 45° with respect to the x_1 axis is presented in Figure 106(a). The same procedure that was adopted for the numerical analysis is implemented, and the computed DOA results in 44.13°, with an error of only 0.87°, Figure 106(b).

Results for different DOAs are collected by rotating the IDR shape, thus maintaining the same experimental setup, which allows to perform a single SLDV scan. The obtained results are summarized in Table 9. As for the numerical case, the DOAs detected by the sensor are very close to those expected, with a maximum discrepancy of 3°, excluding the 0° and 90° directions. As remarked above, these two directions are considered exceptions, since the IDR output is either non-existent, or misleading.

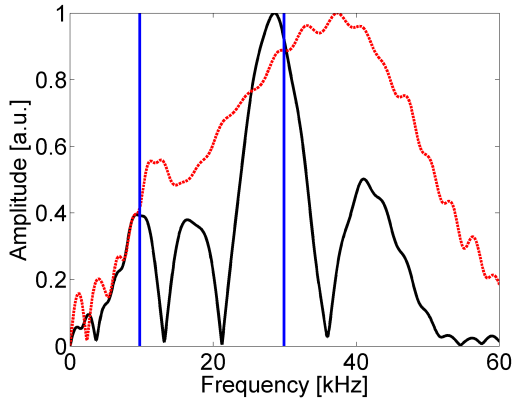

(a)

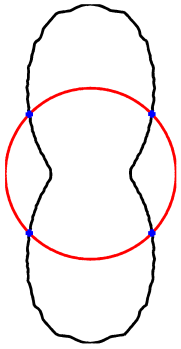

(b)

Figure 106: IDR experimental synthesis results. (a) Frequency spectrums. Black solid line: signal collected by the IDR electrodes. Red dashed line: reference signal. Blue solid lines: pilot frequencies. (b) Directionality interpolation. Black line: directionality ratio. Red line: Directionality ratio deriving from the signal collected from the synthesized IDR. Blue dots: intersections.

Table 9: DOA predictions for the experimentally synthesized IDR. Estimates reported include spurious directions derived from its intrinsic directionality indetermination.

IDR Rotation Angle	Actual Impact DOA	IDR Estimate DOA
-45°	90°	$\pm 84.83° \pm 95.14°$
-30°	75°	$\pm 72.02° \pm 107.61°$
-15°	60°	$\pm 57.95° \pm 121.93°$
0°	45°	$\pm 44.13° \pm 135.90°$
15°	30°	$\pm 30.57° \pm 149.62°$
30°	15°	$\pm 16.81° \pm 163.16°$
45°	0°	$\pm 7.97° \pm 172.03°$

6.5 Manufacturing Considerations

Although in this work an IDR prototype was not fabricated, a brief overview on envisioned manufacturing procedures is now presented. In particular, two simple and cost-effective solutions consider PVDF as the material of choice for the substrate, given its suitability for sensing operations due to its flexibility, light weight, and ease of processing.

6.5.1 Inkjet printing of Electrode Patterns

The first method that can be used for IDR prototyping features inkjet printing of its electrodes on a PVDF substrate. As PVDF comes in thin sheets, it is fully compatible with

inkjet printing, which provides a great choice for patterning electrodes with complicated shapes, such as those of IDR devices. As reported by Baravelli [5] this technique has been successfully adopted for FSAT sensing applications.

This fabrication approach consists in printing the electrodes' geometry as a thin polymer film on a metalized PVDF substrate. The printed features are then used as an etch resist mask for a subsequent metal etching step. This procedure is applied on a single side of the substrate, while the back side metalization provides the common ground electrical connection. After the etching step, the polymer mask is stripped away, leaving the desired electrodes' geometry in place.

6.5.2 Laser Cutting of Electrode Patterns

A second, faster, technique can be adopted to manufacture the IDR complex electrodes' geometrical shape. This technique, that features laser cutting of custom patterns, has been successfully used by Carrara [11] for the manufacturing of complex geometrical shapes associated with a distributed harvester geometry.

This fabrication approach starts with dxf representation of the desired electrodes' shape. This is feed to a CO_2 laser (e.g. the Trotec Speedy 300 Laser Engraver) which directly cuts into a PVDF substrate that has been previously bonded on the test structure. It is worth noting that, although the laser parameters must be fine tuned to prevent burning of the PVDF material, the technique is remarkably fast, and would allow to cut the IDR electrodes in few minutes, without the need to handle any chemicals.

6.5.3 IDR Reference Channel

One last thing that needs to be addressed in order to be able to prototype an IDR device, is the inclusion in its geometry of a reference channel. As stated in Section 6.3 this channel should have a shape that would provide an "isotropic reading", i.e. not biased by its geometry ($\mathcal{H}(\vartheta) = 1$). A closer look to the IDR shape depicted in Figure 104(a) shows that the idea location for the reference would probably be at the center of the IDR. The envisioned final IDR configuration is thus that of Figure 107.

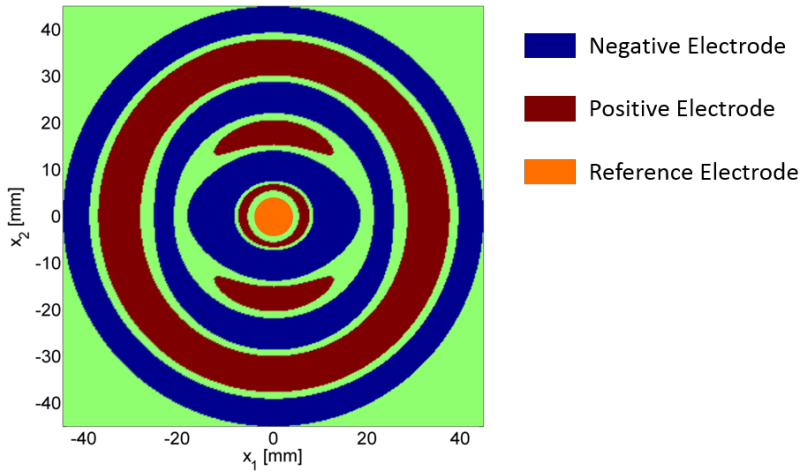

Figure 107: Envisioned electrodes configuration for a possible electrodes' arrangement of an IDR prototype.

6.6 Envisioned Application: Impact Source Localization

The combination of two IDRs would allow the determination of the actual location of the impact source when factoring in the geometry of the structural component, as well as the transducers location on it. Thus, as a final remark, a possible implementation of such a system is here reported for sake of completion.

Considering two IDRs attached on a structural component, the computed DOAs, namely ϕ_A and ϕ_B, define the equations of the straight lines connecting the impact source to each of the IDRs centroids

$$\begin{aligned} y_S &= (x_S - x_A)\tan(\phi_A) + y_A \\ y_S &= (x_S - x_B)\tan(\phi_B) + y_B \end{aligned} \tag{108}$$

where (x_S, y_S) represents the coordinates of the impact source in the $(x\,, y)$ Cartesian system, and $(x_A\,, y_A)$, $(x_B\,, y_B)$ represent the coordinates of the centroids of the two IDRs, respectively. The linear system of equation can be easily solved for the coordinates of the impact source as

$$\begin{aligned} x_S &= \frac{y_B - y_A + x_A\tan\phi_A - x_B\tan\phi_B}{\tan\phi_A - \tan\phi_B} \\ y_S &= (x_S - x_A)\tan(\phi_A) + y_A \end{aligned} \tag{109}$$

It is worth noting that realistic impact localization networks would require the use of a third IDR, in order to eliminate the so called "shadowing" problem along the direction

connecting the two IDRs. This would also be beneficial in addressing the four-folded indetermination, specifically by combining informations on source localizations and specimen geometry. Finally, a denser array of IDRs would also be beneficial for large area coverage in highly damped specimens, such as composites.

6.7 Conclusions

In this chapter an approach based on the employment of the wavenumber design technique has been proposed to design a transducer, named Impact Directionality Revealer (IDR), that is able to determine the direction of arrival of impact events. More in detail, the IDR is a device that is able to determine the direction of an impact relying on a two-point inspection of the spectrum of its sensed voltage generated by the impact, which provides the interrogating wave packet. Numerical and experimental validation of the concept have been presented to demonstrate the principles of operation associated with the device.

In the next chapter, a summary of the work conducted in this thesis will be presented, alongside with the discussion of the contributions made towards the implementation of innovative SHM devices. Finally, challenges associated with the presented formulations as well as future work envisioned to advance the state of the art on the subjects discussed herein will be presented.

CHAPTER VII

CONCLUSIONS AND FUTURE WORK

7.1 Summary

This research studies the application of Fourier-based methodologies to the design of acoustic transducers that find application in the broad area of Structural Health Monitoring (SHM). The analytical framework of the equations governing sensing and generation of guided waves through surface-mounted piezoelectric devices provides the design tools for electrode patterning. The underlying design principle relies on the wavenumber domain representation to confer ad hoc sensing and actuation capabilities to the transducers. The configurations investigated are (i) the spiral Frequency Steered Acoustic Transducer (FSAT), (ii) the Acoustic Wave Rosette (AWR), and (iii) the Impact Direction Revealer (IDR).

The work expands on FSATs as devices that are capable of continuous frequency-based beam steering on isotropic and anisotropic plate-like structures. Analytical/numerical simulations are performed to verify the transducer performance in actuation mode. Successively, device prototyping on monolithic piezo wafers proves their effectiveness in directional actuation of guided waves. The main drawback of this device resides in the absence of conformability, which would represent a strong limitation to its applicability to real-life scenarios. To overcome this problem, the FSAT design is ported to piezo-fibers active layers. The design procedure is therefore adjusted to compensate for active layer anisotropy, and the modifications are proved to be effective through piezo-elastic coupled FE simulations. The new device, that features a new "apodized" shape, is thus fabricated in collaboration with Dr. Cesnik group at the University of Michigan at Ann Arbor, and directional actuation properties are verified experimentally. Later, the damage detection capabilities of monolithic spiral FSATs are assessed in pulse-echo operation. To this aim, tailored imagining techniques are employed for damage localization. The tests demonstrate the ability to locate damage sites on both isotropic and anisotropic plates.

The sensor design approach is successively extended to strain sensing applications, whereby the Acoustic Wave Rosette, AWR, concept is introduced. The device is capable of multiple strain component detection through the monitoring of frequency shifts associated with shape change of the electrode pattern. The spatial filtering that is at the foundation of FSAT devices is here re-imagined for strain sensing. Analytical/numerical as well as experimental proofs-of-concept of AWR effectiveness are presented.

The work finally presents the Impact Directionality Revealer, IDR, for impact localization. Relative low frequency contents of the vast majority of impact event would imply unacceptable spatial dimensions for FSAT arrangements. To address this, the IDR exploits information from the wave amplitude collected by the device at specific, pilot, frequencies. This leads to a formulation whereby the direction of arrival of a wave packet generated by a potential impact event can be detected simply by relying on the geometrical shape of the device electrodes. In support of the theoretical derivations, numerical simulation using Green's functions formalism, as well as experimental evidence of the device effectiveness are presented.

7.2 Contributions

The research presented in this work tackles three different areas that are relevant to SHM applications: (i) active monitoring of damage detection in waveguides, (ii) strain sensing for loads monitoring, and (iii) passive localization of impact events. Specifically, the work documented in this thesis provides the following contributions to the state of the art:

- Spiral frequency steered acoustic transducers:
  - Development of monolithic spiral FSATs for directional sensing and actuation of guided waves in both isotropic and anisotropic plate-like structures;
  - Development of the toner transfer method as a rapid and cost-effective technique for the prototyping of complex electrode shapes on monolithic piezoelectric wafers;
  - Adaption of FSAT framework to comprise piezo-fibrous active layers with the development of an anisotropy compensated device;

  - Experimental and numerical validation of directional actuation for both (i) the spiral FSAT prototypes realized on monolithic piezoelectric wafers, and (ii) the apodized spiral FSAT prototype on a piezo-fibrous active layer;
  - Experimental implementation of damage imaging techniques that exploit pulse-echo operations of the spiral FSAT prototypes manufactured on monolithic piezo wafers;
  - Adaption of FSAT framework to extend its applicability field to anisotropic composite plates.

- Acoustic wave rosettes:
  - Outline of a novel theoretical framework for the novel class of AWR transducers;
  - Numerical proof-of-concept of the AWR filtering properties and strain sensing performance through application to two different load scenarios where analytical solutions are available;
  - Experimental proof-of-concept of the AWR filtering properties for a device that targets Lamb waves, in order to be able to exploit the available experimental setup;
  - Envisioned prototype manufacturing process through the use of micro-fabrication techniques;

- Impact directionality revealers:
  - Formulation of sensing principles for the novel class of IDR transducers;
  - Numerical and experimental proof-of-concept of the effectiveness of IDR arrangements;
  - Envisioned prototype manufacturing guidelines.

7.3 Future Work

The devices presented in this research work are still in their formative years. While the spiral FSAT presented herein count on a strong foundation deriving from previous work

done in the research group, both AWRs and IDRs designs are completely new contributions of this thesis. All three classes of devices still present limitations and challenges that need to be addressed as part of future work.

7.3.1 Towards FSAT Devices

On one hand, the spiral FSAT prototypes on monolithic piezo wafer demonstrated their effectiveness on both isotropic and anisotropic composite plates. This was limited to laboratory scenarios: however the results achieved with the device in pulse-echo mode are promising, although some challenges have arisen. In particular, the effect and role of the bonding layer on the transducer directionality needs to be addressed in detail. Also, specifically for composites, the role of material attenuation needs to be studied in depth, so that more efficient interrogation strategies can be developed.

On the other hand, the apodized spiral FSAT prototype with a piezo-fibrous active layer proved its effectiveness in actuation mode, although the recorded directionality distortion was greater than the one registered for the FSAT prototype manufactured on a monolithic piezo wafer. The manufacturing of a new prototype with (i) reduced bandwidth, and (ii) an effective poling procedure should be pursued, along with testing of the device damage localization performance through pulse-echo schemes.

The ultimate challenge is the manufacturing of an apodized spiral FSAT for pulse-echo operations on composites. To this aim, a refined design able to mitigate the presence of directional attenuation must be studied.

7.3.2 Towards AWR Devices

The AWR presents multiple challenges, mainly related to its prototyping and testing. As explained in Section 5.5, standard microfabrication techniques should be suitable to bring the device to a prototype level. One challenge associated with fabrication would is represented by the handling of the split-electrode configuration, where masks alignment would be critical to ensure satisfactory performances of the device.

A second challenge is represented by the inclusion in the device of an actuator able to

generate the required interrogating wave. This is envisioned to be done through a ring-shaped comb-like arrangement of the electrode with inter-finger spacing corresponding to the center frequency of the AWR.

Once fabrication procedures are assessed, the major challenge would be to implement a temperature compensation procedure, which will be of paramount importance for the future use of the device as a strain gage.

7.3.3 Towards IDR Devices

The challenges associated to IDRs are related to manufacturing, and, more prominently, to the implementation of impact localization schemes featuring multiple devices to perform real-time detection of impact-like events.

Although the manufacturing procedure should be quite straightforward, the implementation of impact detection schemes according to the guidelines reported in Section 6.6 would require some additional thoughts. The main challenge associated with this is related to issues that might arise from the 4-folded indetermination, which is an intrinsic characteristic of the device.

As a final remark, it is worth noting that there is no need for individual control of single transducer elements for any of the proposed devices and concepts. This drastically reduces hardware and power requirements, so that cost and hardware limitations of traditional solutions can be partially mitigated.

REFERENCES

[1] Achenbach, J., *Wave propagation in elastic solids*. Elsevier, 1984.

[2] Alers, G. and Burns, L., "Emat designs for special applications," *Materials Evaluation*, vol. 45, no. 10, p. 1184, 1987.

[3] Auld, B. A., *Acoustic fields and waves in solids*. 1973.

[4] Baravelli, E., Senesi, M., Ruzzene, M., De Marchi, L., and Speciale, N., "Double-channel, frequency-steered acoustic transducer with 2-D imaging capabilities," *Ultrasonics, Ferroelectrics and Frequency Control, IEEE Transactions on*, vol. 58, no. 7, pp. 1430–1441, 2011.

[5] Baravelli, E., Senesi, M., Gottfried, D., De Marchi, L., and Ruzzene, M., "Inkjet fabrication of spiral frequency-steerable acoustic transducers (fsats)," in *SPIE Smart Structures and Materials+ Nondestructive Evaluation and Health Monitoring*, pp. 834817–834817, International Society for Optics and Photonics, 2012.

[6] Bartoli, I., Marzani, A., di Scalea, F. L., and Viola, E., "Modeling wave propagation in damped waveguides of arbitrary cross-section," *Journal of Sound and Vibration*, vol. 295, no. 3, pp. 685–707, 2006.

[7] Bauchau, O. A. and Craig, J. I., *Structural analysis: with applications to aerospace structures*, vol. 163. Springer Science & Business Media, 2009.

[8] Bennett, S., Peterson, D., Corl, D., and Kino, G. S., "A real-time synthetic aperture digital acoustic imaging system," in *Acoustical Imaging*, pp. 669–692, Springer, 1982.

[9] Bulst, W.-E., Fischerauer, G., and Reindl, L., "State of the art in wireless sensing with surface acoustic waves," *Industrial Electronics, IEEE Transactions on*, vol. 48, no. 2, pp. 265–271, 2001.

[10] Caliendo, C., D'amico, A., Varadi, P., and Verona, E., "Surface acoustic wave h 2 sensor on silicon substrate," in *Ultrasonics Symposium, 1988. Proceedings., IEEE 1988*, pp. 569–574, IEEE, 1988.

[11] Carrara, M., Kulpe, J., Leadenham, S., Leamy, M., and Erturk, A., "Fourier transform-based design of a patterned piezoelectric energy harvester integrated with an elastoacoustic mirror," *Applied Physics Letters*, vol. 106, no. 1, p. 013907, 2015.

[12] Carrara, M. and Ruzzene, M., "Numerical and experimental analysis of guided waves propagation in composite plates," in *SPIE Smart Structures and Materials+ Nondestructive Evaluation and Health Monitoring*, pp. 86950W–86950W, International Society for Optics and Photonics, 2013.

[13] Chiu, W. K., Galea, S., Koss, L., and Rajic, N., "Damage detection in bonded repairs using piezoceramics," *Smart materials and Structures*, vol. 9, no. 4, p. 466, 2000.

[14] Chung, S.-J., Li, M.-Y., Kanamaluru, S., and Chang, K., "Meander-image-line-feed microstrip antenna array for frequency-swept beam steering," in *Antennas and Propagation Society International Symposium, 1996. AP-S. Digest*, vol. 2, pp. 1254–1257, IEEE, 1996.

[15] Cullen, D. E. and Montress, G. K., "Progress in the development of saw resonator pressure transducers," in *1980 Ultrasonics Symposium*, pp. 696–701, IEEE, 1980.

[16] De Marchi, L., Marzani, A., Speciale, N., and Viola, E., "Dispersion compensation of lamb waves with the warped frequency transform in passive monitoring techniques," in *Ultrasonics Symposium (IUS), 2010 IEEE*, pp. 133–136, IEEE, 2010.

[17] Degertekin, F. L. and Khuri-Yakub, B. T., "Single mode lamb wave excitation in thin plates by hertzian contacts," *Applied physics letters*, vol. 69, no. 2, pp. 146–148, 1996.

[18] Deraemaeker, A. and Nasser, H., "Numerical evaluation of the equivalent properties of macro fiber composite (mfc) transducers using periodic homogenization," *International journal of solids and structures*, vol. 47, no. 24, pp. 3272–3285, 2010.

[19] Deraemaeker, A., Nasser, H., Benjeddou, A., and Preumont, A., "Mixing rules for the piezoelectric properties of macro fiber composites," *Journal of intelligent material systems and structures*, vol. 20, no. 12, pp. 1475–1482, 2009.

[20] Diaz Valdes, S. and Soutis, C., "Health monitoring of composites using lamb waves generated by piezoelectric devices," *Plastics, Rubber and Composites*, vol. 29, no. 9, pp. 475–481, 2000.

[21] Drafts, B., "Acoustic wave technology sensors," *Microwave Theory and Techniques, IEEE Transactions on*, vol. 49, no. 4, pp. 795–802, 2001.

[22] Du, X., Fu, Y., Tan, S., Luo, J., Flewitt, A., Maeng, S., Kim, S., Choi, Y., Lee, D., Park, N., and others, "Zno film for application in surface acoustic wave device," in *Journal of Physics: Conference Series*, vol. 76, p. 012035, IOP Publishing, 2007.

[23] Ellerbrock, P. J., "Dc-xa structural health-monitoring fiber optic-based strain measurement system," in *Smart Structures and Materials' 97*, pp. 207–218, International Society for Optics and Photonics, 1997.

[24] Fromme, P., Wilcox, P., Lowe, M., and Cawley, P., "A guided ultrasonic waves array for structural integrity monitoring," in *REVIEW OF PROGRESS IN QUANTITATIVE NONDESTRUCTIVE EVALUATION*, vol. 760, pp. 1780–1787, AIP Publishing, 2005.

[25] Fu, S., Shi, L., Zhou, Y., and Cai, J., "Dispersion compensation in lamb wave defect detection with step-pulse excitation and warped frequency transform," *Ultrasonics, Ferroelectrics, and Frequency Control, IEEE Transactions on*, vol. 61, no. 12, pp. 2075–2088, 2014.

[26] Giurgiutiu, V., "Tuned lamb wave excitation and detection with piezoelectric wafer active sensors for structural health monitoring," *Journal of intelligent material systems and structures*, vol. 16, no. 4, pp. 291–305, 2005.

[27] Giurgiutiu, V., *Structural health monitoring: with piezoelectric wafer active sensors*. Academic Press, 2007.

[28] Giurgiutiu, V. and Bao, J., "Embedded-ultrasonics structural radar for in situ structural health monitoring of thin-wall structures," *Structural Health Monitoring*, vol. 3, no. 2, pp. 121–140, 2004.

[29] Giurgiutiu, V., Bao, J., and Zagrai, A. N., "Structural health monitoring system utilizing guided lamb waves embedded ultrasonic structural radar," Feb. 7 2006. US Patent 6,996,480.

[30] Graff, K. F., *Wave motion in elastic solids*. Courier Dover Publications, 1975.

[31] Grate, J. W., Martin, S. J., and White, R. M., "Acoustic wave microsensors," *Analytical Chemistry*, vol. 65, no. 21, pp. 940A–948A, 1993.

[32] Hagood, N. and Bent, A., "Development of piezoelectric fiber composites for structural actuation," *AIAA Paper*, no. 93-1717, pp. 3265–3638, 1993.

[33] Hall, J. S. and Michaels, J. E., "Minimum variance ultrasonic imaging applied to an in situ sparse guided wave array," *Ultrasonics, Ferroelectrics, and Frequency Control, IEEE Transactions on*, vol. 57, no. 10, pp. 2311–2323, 2010.

[34] Hautamaki, C., Zurn, S., Mantell, S. C., and Polla, D. L., "Experimental evaluation of mems strain sensors embedded in composites," *Microelectromechanical Systems, Journal of*, vol. 8, no. 3, pp. 272–279, 1999.

[35] Heinonen, E., Juuti, J., and Leppävuori, S., "Characterization and modelling of 3d piezoelectric ceramic structures with atila software," *Journal of the European Ceramic Society*, vol. 25, no. 12, pp. 2467–2470, 2005.

[36] Holland, M. G. and Claiborne, L. T., "Practical surface acoustic wave devices," *Proceedings of the IEEE*, vol. 62, no. 5, pp. 582–611, 1974.

[37] Hoummady, M., Campitelli, A., and Wlodarski, W., "Acoustic wave sensors: design, sensing mechanisms and applications," *Smart materials and structures*, vol. 6, no. 6, p. 647, 1997.

[38] http://www.instructables.com/id/Easy-Consistent-Cheap-Toner-Transfer-Method-for Si/, "Easy, consistent and cheap toner transfer method for single and double sided pcbs."

[39] James, W. and Wilkie, W. K., "Method of fabricating nasa-standard macro-fiber composite piezoelectric actuators," *NASA/TM*, vol. 212427, 2003.

[40] Kehlenbach, M. and Das, S., "Identifying damage in plates by analyzing lamb wave propagation characteristics," in *Proc. SPIE*, vol. 4702, pp. 364–75, 2002.

[41] Keilers, C. H., Chang, F.-K., and others, "Identifying delamination in composite beams using built-in piezoelectrics: part iexperiments and analysis," *Journal of Intelligent Material Systems and Structures*, vol. 6, no. 5, pp. 649–663, 1995.

[42] Kessler, S. S. and Spearing, S. M., "Design of a piezoelectric-based structural health monitoring system for damage detection in composite materials," in *SPIE's 9th Annual International Symposium on Smart Structures and Materials*, pp. 86–96, International Society for Optics and Photonics, 2002.

[43] Khlebarov, Z. P., Stoyanova, A. I., and Topalova, D. I., "Surface acoustic wave gas sensors," *Sensors and Actuators B: Chemical*, vol. 8, no. 1, pp. 33–40, 1992.

[44] Kim, D. and Philen, M., "On the beamsteering characteristics of MFC phased arrays for structural health monitoring," *Proc. of 49th AIAA/ASME Structures*, pp. 1–6, 2008.

[45] Koh, Y., Chiu, W. K., and Rajic, N., "Effects of local stiffness changes and delamination on lamb wave transmission using surface-mounted piezoelectric transducers," *Composite Structures*, vol. 57, no. 1, pp. 437–443, 2002.

[46] Kollar, L. P. and Van Steenkiste, R. J., "Calculation of the stresses and strains in embedded fiber optic sensors," *Journal of Composite Materials*, vol. 32, no. 18, pp. 1647–1679, 1998.

[47] Konstantinidis, G., Drinkwater, B., and Wilcox, P., "The temperature stability of guided wave structural health monitoring systems," *Smart Materials and Structures*, vol. 15, no. 4, p. 967, 2006.

[48] Koosha, A. and Sunthankar, Y., "A novel directional ultrasonic radiator," in *Ultrasonics Symposium, 1989. Proceedings., IEEE 1989*, pp. 785–788, IEEE, 1989.

[49] Lastari, W. and Qiao, P., "Experimental investigation of damage detection on composite plates using wave analysis," in *Proc. SPIE*, vol. 5767, pp. 81–9, 2005.

[50] Laude, V., Gérard, D., Khelfaoui, N., Jerez-Hanckes, C. F., Benchabane, S., and Khelif, A., "Subwavelength focusing of surface acoustic waves generated by an annular interdigital transducer," *Applied Physics Letters*, vol. 92, no. 9, p. 094104, 2008.

[51] Li, J. and Rose, J. L., "Implementing guided wave mode control by use of a phased transducer array," *Ultrasonics, Ferroelectrics and Frequency Control, IEEE Transactions on*, vol. 48, no. 3, pp. 761–768, 2001.

[52] Lonsdale, A. and Lonsdale, B., "Method and apparatus for measuring strain," Dec. 17 1996. US Patent 5,585,571.

[53] Marantidis, C., Van Way, C. B., and Kudva, J. N., "Acoustic-emission sensing in an on-board smart structural health monitoring system for military aircraft," in *1994 North American Conference on Smart Structures and Materials*, pp. 258–264, International Society for Optics and Photonics, 1994.

[54] Matt, H. and Lanza di Scalea, F., "Macro-fiber composite piezoelectric rosettes for acoustic source location in complex structures," in *The 14th International Symposium on: Smart Structures and Materials & Nondestructive Evaluation and Health Monitoring*, pp. 65290Q–65290Q, International Society for Optics and Photonics, 2007.

[55] McCallum, J. J., "Piezoelectric devices for mass and chemical measurements: an update. a review," *Analyst*, vol. 114, no. 10, pp. 1173–1189, 1989.

[56] McNab, A. and Campbell, M. J., "Ultrasonic phased arrays for nondestructive testing," *NDT international*, vol. 20, no. 6, pp. 333–337, 1987.

[57] Michaels, J. E., Croxford, A. J., and Wilcox, P. D., "Imaging algorithms for locating damage via in situ ultrasonic sensors," in *Sensors Applications Symposium, 2008. SAS 2008. IEEE*, pp. 63–67, IET, 2008.

[58] Osmont, D. L., Devillers, D., and Taillade, F., "Health monitoring of sandwich plates based on the analysis of the interaction of lamb waves with damages," in *SPIE's 8th Annual International Symposium on Smart Structures and Materials*, pp. 290–301, International Society for Optics and Photonics, 2001.

[59] Pelts, S., Jiao, D., and Rose, J., "A comb transducer for guided wave generation and mode selection," in *Ultrasonics Symposium, 1996. Proceedings., 1996 IEEE*, vol. 2, pp. 857–860, IEEE, 1996.

[60] Pierce, S. and Culshaw, B., "Laser generation of ultrasonic lamb waves using low power optical sources," *IEE Proceedings-Science, Measurement and Technology*, vol. 145, no. 5, pp. 244–249, 1998.

[61] Pohl, A., Ostermayer, G., Reindl, L., and Seifert, F., "Monitoring the tire pressure at cars using passive SAW sensors," in *Ultrasonics Symposium, 1997. Proceedings., 1997 IEEE*, vol. 1, pp. 471–474, IEEE, 1997.

[62] Rabiner, L. R. and Gold, B., "Theory and application of digital signal processing," *Englewood Cliffs, NJ, Prentice-Hall, Inc., 1975. 777 p.*, vol. 1, 1975.

[63] Raghavan, A. and Cesnik, C. E., "Finite-dimensional piezoelectric transducer modeling for guided wave based structural health monitoring," *Smart materials and structures*, vol. 14, no. 6, p. 1448, 2005.

[64] Raghavan, A. and Cesnik, C. E., "Review of guided-wave structural health monitoring," *Shock and Vibration Digest*, vol. 39, no. 2, pp. 91–116, 2007.

[65] Rees, D., Chiu, W., and Jones, R., "A numerical study of crack monitoring in patched structures using a piezoelectric sensor," *Smart materials and Structures*, vol. 1, no. 3, p. 202, 1992.

[66] Ribay, G., Catheline, S., Clorennec, D., Kiri Ing, R., Quieffin, N., and Fink, M., "Acoustic impact localization in plates: properties and stability to temperature variation," *Ultrasonics, Ferroelectrics, and Frequency Control, IEEE Transactions on*, vol. 54, no. 2, pp. 378–385, 2007.

[67] Rose, J. L. and others, "A baseline and vision of ultrasonic guided wave inspection potential," *Transactions-American Society of Mechanical Engineers Journal of Pressure Vessel Technology*, vol. 124, no. 3, pp. 273–282, 2002.

[68] Rose, J., Ditri, J. J., Pilarski, A., Rajana, K., and Carr, F., "A guided wave inspection technique for nuclear steam generator tubing," *NDT & E International*, vol. 27, no. 6, pp. 307–310, 1994.

[69] Salas, K. I. and Cesnik, C. E. S., "Guided wave structural health monitoring using CLoVER transducers in composite materials," *Smart Materials and Structures*, vol. 19, no. 1, p. 015014, 2010.

[70] Salas, K. I. and Cesnik, C. E., "Design and characterization of the clover transducer for structural health monitoring," in *The 15th International Symposium on: Smart Structures and Materials & Nondestructive Evaluation and Health Monitoring*, pp. 69350B–69350B, International Society for Optics and Photonics, 2008.

[71] Salas, K. and Cesnik, C. E., "Guided wave excitation by a clover transducer for structural health monitoring: theory and experiments," *Smart Materials and Structures*, vol. 18, no. 7, p. 075005, 2009.

[72] Salas, K. and Cesnik, C., "Clover: an alterntive concept for damage interrogation in structural health monitoring systems," *Aeronautical Journal*, vol. 113, no. 1144, pp. 339–356, 2009.

[73] Schoess, J. N. and Zook, J. D., "Test results of a resonant integrated microbeam sensor (rims) for acoustic emission monitoring," in *5th Annual International Symposium on Smart Structures and Materials*, pp. 326–332, International Society for Optics and Photonics, 1998.

[74] Senesi, M. and Ruzzene, M., "A spiral frequency steerable acoustic transducer for SHM," in *SPIE Smart Structures and Materials+ Nondestructive Evaluation and Health Monitoring*, pp. 798136–798136, International Society for Optics and Photonics, 2011.

[75] Senesi, M., Xu, B., and Ruzzene, M., "Experimental characterization of periodic frequency-steerable arrays for structural health monitoring," *Smart Materials and Structures*, vol. 19, no. 5, p. 055026, 2010.

[76] Seydel, R. and Chang, F., "Implementation of a real-time impact identification technique for stiffened composite panels," in *Proceedings of the 2nd International Workshop on Structural Health Monitoring*, pp. 225–233, 1999.

[77] Shoykhetbrod, A., Nussler, D., and Hommes, A., "Design of a siw meander antenna for 60 ghz applications," in *Microwave Conference (GeMiC), 2012 The 7th German*, pp. 1–3, IEEE, 2012.

[78] Sirohi, J. and Chopra, I., "Fundamental understanding of piezoelectric strain sensors," *Journal of Intelligent Material Systems and Structures*, vol. 11, no. 4, pp. 246–257, 2000.

[79] Stoney, R., "Characterisation of a wireless passive surface acoustic wave strain sensor," *Trinity College Dublin*, 2009.

[80] Strassburger, E., Patel, P., McCauley, J. W., Kovalchick, C., Ramesh, K., and Templeton, D. W., "High-speed transmission shadowgraphic and dynamic photoelasticity study of stress wave and impact damage propagation in transparent materials and laminates using the edge-on impact (eoi) method," tech. rep., DTIC Document, 2008.

[81] Sun, K. J., Kishoni, D., and Johnston, P. H., "Feasibility of using lamb waves for corrosion detection in layered aluminium aircraft structures," in *Ultrasonics Symposium, 1993. Proceedings., IEEE 1993*, pp. 733–736, IEEE, 1993.

[82] Tirole, N., Choujaa, A., Hauden, D., and Martin, G., "Lamb waves pressure sensor using an aln/si structure," in *Ultrasonics Symposium*, vol. 1, pp. 371–371, INSTITUTE OF ELECTRICAL & ELECTRONICS ENGINEERS INC, 1993.

[83] Tua, P., Quek, S., and Wang, Q., "Detection of cracks in plates using piezo-actuated lamb waves," *Smart Materials and Structures*, vol. 13, no. 4, p. 643, 2004.

[84] Valdés, S. H. D. and Soutis, C., "Real-time nondestructive evaluation of fiber composite laminates using low-frequency lamb waves," *The Journal of the Acoustical Society of America*, vol. 111, no. 5, pp. 2026–2033, 2002.

[85] Van Trees, H. L., *Detection, Estimation, and Modulation Theory, Optimum Array Processing*. Wiley-Interscience, 2004.

[86] Weisstein, E. W., "Archimedes spiral," *From MathWorld-A Wolfram Web Resource. http://mathworld. wolfram. com/ArchimedesSpiral. html*, 2011.

[87] Weld, C. E., Sternhagen, J. D., Mileham, R. D., Mitzner, K. D., and Galipeau, D. W., "Temperature measurement using surface skimming bulk waves," in *Ultrasonics Symposium, 1999. Proceedings. 1999 IEEE*, vol. 1, pp. 441–444, IEEE, 1999.

[88] Weyman, A. E., *Principles and Practice of Echocardiography*. LWW; Second edition, 1994.

[89] Wilcox, P., Lowe, M., and Cawley, P., "The effect of dispersion on long-range inspection using ultrasonic guided waves," *NDT & E International*, vol. 34, no. 1, pp. 1–9, 2001.

[90] Wilcox, P. D., "A rapid signal processing technique to remove the effect of dispersion from guided wave signals," *Ultrasonics, Ferroelectrics, and Frequency Control, IEEE Transactions on*, vol. 50, no. 4, pp. 419–427, 2003.

[91] Wilcox, P., Lowe, M., and Cawley, P., "Mode and transducer selection for long range lamb wave inspection," *Journal of intelligent material systems and structures*, vol. 12, no. 8, pp. 553–565, 2001.

[92] Wilkie, W. K., Bryant, R. G., Fox, R. L., Hellbaum, R. F., High, J. W., Jalink Jr, A., Little, B. D., and Mirick, P. H., "Method of fabricating a piezoelectric composite apparatus," Oct. 7 2003. US Patent 6,629,341.

[93] Wilkie, W. K., Inman, D. J., Lloyd, J. M., and High, J. W., "Anisotropic laminar piezocomposite actuator incorporating machined pmn–pt single-crystal fibers," *Journal of Intelligent material systems and structures*, vol. 17, no. 1, pp. 15–28, 2006.

[94] Wilkie, W. K., Bryant, R. G., High, J. W., Fox, R. L., Hellbaum, R. F., Jalink Jr, A., Little, B. D., and Mirick, P. H., "Low-cost piezocomposite actuator for structural control applications," in *SPIE's 7th Annual International Symposium on Smart Structures and Materials*, pp. 323–334, International Society for Optics and Photonics, 2000.

[95] Williams, R. B., Grimsley, B. W., Inman, D. J., and Wilkie, W. K., "Manufacturing and cure kinetics modeling for macro fiber composite actuators," *Journal of reinforced plastics and composites*, vol. 23, no. 16, pp. 1741–1754, 2004.

[96] Williams, R. B., Park, G., Inman, D. J., and Wilkie, W. K., "An overview of composite actuators with piezoceramic fibers," *Proceeding of IMAC XX*, pp. 4–7, 2002.

[97] Wilson, W., Malocha, D., Kozlovski, N., Gallagher, D., Fisher, B., Pavlina, J., Saldanha, N., Puccio, D., and Atkinson, G., "Orthogonal frequency coded saw sensors for aerospace shm applications," *Sensors Journal, IEEE*, vol. 9, no. 11, pp. 1546–1556, 2009.

[98] Wilson, W. C. and Atkinson, G. M., "Wireless sensor applications in extreme aeronautical environments," in *Wireless for Space and Extreme Environments (WiSEE), 2013 IEEE International Conference on*, pp. 1–6, IEEE, 2013.

[99] www.efunda.com, "Efunda."

[100] Yang, M. and Qiao, P., "Modeling and experimental detection of damage in various materials using the pulse-echo method and piezoelectric sensors/actuators," *Smart materials and structures*, vol. 14, no. 6, p. 1083, 2005.

[101] Yatsuda, H., "Design techniques for saw filters using slanted finger interdigital transducers," *Ultrasonics, Ferroelectrics and Frequency Control, IEEE Transactions on*, vol. 44, no. 2, pp. 453–459, 1997.

[102] Yu, L. and Giurgiutiu, V., "In situ 2-d piezoelectric wafer active sensors arrays for guided wave damage detection," *Ultrasonics*, vol. 48, no. 2, pp. 117–134, 2008.

[103] Zhu, W., Rose, J., Barshinger, J., and Agarwala, V., "Ultrasonic guided wave ndt for hidden corrosion detection," *Journal of Research in Nondestructive Evaluation*, vol. 10, no. 4, pp. 205–225, 1998.